University of Alberta

Sub-micron Resolution Three Dimensional Structure Writing Using Two-Photon Absorption Process

by

A K M Zahidur Rahim Chowdhury 

A thesis submitted to the Faculty of Graduate Studies and Research in partial fulfillment of the requirements for the degree of Master of Science

Department of Electrical and Computer Engineering

Edmonton, Alberta

Fall 2006

Your file Votre référence
ISBN: 978-0-494-22244-7
Our file Notre référence
ISBN: 978-0-494-22244-7

Abstract

Nanometer resolution three dimensional(3D) structure-writing using two-photon absorption(TPA) has potential applications in the fabrication of various photonic and micro-mechanical devices. In a TPA process it is possible to modify the physical properties within a small subwavelength volume making 3D writing possible on a submicron scale with a simple process. SU-8 and Ormocore are two popular photoresists used for 800 nm Ti:Sapphire laser writing. Different simple 3D structures are reported in this thesis. A comparison of the performances of these two polymers for a particular laser system is presented for 80 fs 800 nm pulses. Structures with a minimum resolution of ~320 nm and 1.3 μm were achieved for 40X objective using Ormocore and SU8, respectively. Moreover, very high aspect ratio (~40) lines were produced in Ormocore using the TPA writing technique. Parameters such as TPA absorption and behavior of the resist during developing process are very important factors to simulate structure writing using TPA process. TPA coefficients were experimentally determined and the developing process was characterized for the resists.

ACKNOWLEDGEMENTS

There are many people with their direct help or support contributed to this work. I like to thank all of them.

I would like to express my heartiest gratitude, deepest sense of indebtedness, and gratefulness to my supervisor Dr. Robert Fedosejevs, Professor, Department of Electrical and Computer Engineering, University of Alberta, for his friendly supervision, assistance, encouragement, constructive criticism and valuable suggestions in accomplishing my thesis work. His passion for research and broad perspective inspired me all the time. I strongly appreciate the freedom he gave me to explore different possibilities and his confidence in my abilities. Additionally I cannot but say that he was very dynamic and always found time for any consultation even after being involved with so many things. Thanks a lot for all your support.

Dr. Ying Tsui, Associate Professor, Department of ECE, U of A, also supported me in many ways, especially whenever I needed some help and could not get hold of my supervisor. His friend attitude always encouraged me to discuss different topics without hesitation.

I also want to thank all the people in my lab who extended their helping hand in different times. Special thanks to Sean Kirkwood who guided me in so many times and so many ways that I have stopped counting. I also appreciate the help from Craig Unick, Micheal Argument, Mike Taschuk. Moreover, Blair Harwood and Rick Conrad were always beside me when I could not figure out why something wass not working.

I may not be in this position without the contribution from my parents. For sure they will be the most delighted people at my success, may be more delighted than me. Finally, thanks God for directing everything in the best way.

Contents

List of Tables

List of Figures

Chapter 1

Introduction

Laser-material processing started soon after demonstration of the first laser system in 1960. Due to poor beam quality and reproducibility initial investigations were mostly qualitative and mainly devoted to research topics like material evaporation and ablation. Further improvements of laser performance expanded the field to synthesis, plasma formation, laser cutting, hole-drilling, welding, jointing and so forth [7]. Laser-material interaction was primarily based on the thermal effect of laser on material and as a result the development of structure was limited to a one-dimensional (1D) or two-dimensional (2D) shape [8] with resolution characterized by the heat diffusion length in the material. As a result, other than photolithographic process, mostly, the feature size varied from tens of micrometers to millimeters.

The use of short-wavelength excimer laser in ultraviolate (UV) lithography has pushed the linewidth of integrated circuits to less than 100 nm. The process, based on single photon absorption process, is limited to 1D or 2D and relies on chemical bond-breaking changes due to the laser. Still, complex iterative lithographic steps can build up three-dimensional structures.

For 3D structure writing one can take advantage of the nonlinear response (quadratic in intensity) in order to confine the interaction to the focal volume of a high power microscope objective. By using a 3D computer controlled positioning stage to move the sample any arbitrary shape can be written in suitable nonlinear photosensitive material. In this way, nonlinear intensity dependent processes can be utilized to

achieve a 3D structure by scanning the focal spot within the material.

The recent development of fs lasers has added further advantages to laser-material processing. Laser-matter interactions for fs pulses are fundamentally different than longer pulses or CW lasers [7]. When material is irradiated by a fs laser, the photon energy is deposited much faster than electrons can transfer it to the lattice or molecule/atom oscillations through phonon emission or lattice vibration. As a result the thermal effect can be reduced for these short pulse lasers. This provides an ideal optical excitation for many photochemical or photo physical reactions where thermal effects are not desired. Moreover, a fs laser has an extremely large peak power compared to CW and nanosecond lasers. This high transient photon fluence density results in different non-linear process, providing new possibilities for material processing and many fascinating applications. The non-linear effects like two- and multiphoton absorption enable the fabrication of 3D micro-nano structures.

Two photon absorption (TPA) is an optical nonlinear phenomenon that occurs in all materials at sufficiently high level of irradiance when the combined energy of two photons matches the transition energy between the ground state and an excited state. The rate of TPA is proportional to the square of the incident light intensity. The quadratic dependence of the TPA rate on light intensity confines absorption to the highly localized area at the focal point. As a result the photochemical reaction occurs in a region ensuring smaller feature size, compared to the SPA process, produced by the nonlinear interaction changing the physical properties of the material.

In this thesis, different 3D structures are produced in two commercially available photoresists, Ormocore and SU-8. Lines of hundreds of nanometer width and very high aspect ratio were produced in the resists using a Ti:Sapphire fs laser source. Moreover, necessary primary parameters to simulate final structures produced in a TPA process are determined for future modeling of the overall process.

1.1 Background

1.1.1 Single photon absorption

In a single photon absorption (SPA) process the absorption is linearly dependent on intensity. The SPA coefficient, α (m^{-1}), is a material dependent parameter that relates the intensity to the absorption per unit length. Total absorbed energy in the material is also determined by the thickness of the material.

For an incident laser beam with an intensity, I (W m^{-2}), the absorption per unit length for SPA process can be defined as,

$$\frac{dI}{dz} = -\alpha I \tag{1.1}$$

where, z is the direction of beam propagation. The solution of the above equation can be used to determine the transmitted intensity, I_t after traveling though a material of certain thickness Δd (m) as,

$$I_t = I_i e^{-\alpha \Delta d} \tag{1.2}$$

where, I_i is the incident intensity of the beam. Absorption, α_A, in dB m^{-1}, is a widely used term to represent SPA in a material and is given as,

$$\alpha_A = \frac{10 \log_{10}(I_t/I_i)}{\Delta d} \tag{1.3}$$

The resulting change in etch rate depends on the absorbed energy per unit volume and the response of photoresist to the single photon absorption process.

1.1.2 Conventional photo-lithographic process

Photolithography is a widely used process in semiconductor industry to produce two-dimensional (2D) patterns using SPA phenomenon. Photoresists, mostly having absorption in the UV region, are used primarily to transfer the pattern or inverse of the pattern based on the type of the resist and other processing. Then selective etching or deposition of other materials is performed. Finally the resists are removed. Figure 1.1 demonstrates fabrication of a metal layer using a lithographic process. As

illustrated in the figure the exposed area of a positive photoresist washes away after development while the rest remains on the substrate. On the other hand, the exposed area remains on the substrate for a negative resist while the rest washes away.

In a case where there is a small gap between the mask and the resist, the fabrication procedure is called proximity printing as in Figure 1.1. Proximity printing is utilized, for example, when the resist is in a liquid form. In a contact printing process, where the resist is a solid, the mask is pressed hard enough to the substrate so that there is no gap (theoretically) between two surfaces. Diffraction due to spacing between resist and the mask causes a blurred or diffused image on the resist and reduces the resolution. The theoretical resolution for a shadowgraphic printing with a mask consists of equal lines and spaces of width w is given by

$$2w_{min} = 3\sqrt{\lambda\left(g + \frac{1}{2}d\right)} \tag{1.4}$$

where $2w$ is the grating period (m), g is the gap width(= 0 m for contact printing), λ is the wavelength (m) and d is the resist thickness (m). So, higher resolution can be achieved by reducing the gap and/or using shorter wavelength light sources for a particular resist-thickness.

1.1.3 Developing process

Photoresist, more specifically positive photoresist, can be a polymer that breaks into a low molecular weight monomer after the bond-breaking reaction due to absorption of photon-energy. Conversely, there are negative resists which are made up of a combination of monomers and photoinitiators like photo acid generators (PAG). The photoinitiator opens a bond of the monomer to form a unit cell of a large chained polymer. The bond breaking or polymer formation is dependent on the absorbed photon energy. The developer selectively etches away exposed or unexposed portion of the resist based on the type of the resist. A typical resist's behavior in a developing process is given in Figure 1.2. Both Ormocore and SU-8 are negative resists. Contrasts, as shown in the Figure 1.2, for these two resists will be determined in Chapter 2 using SPA exposures.

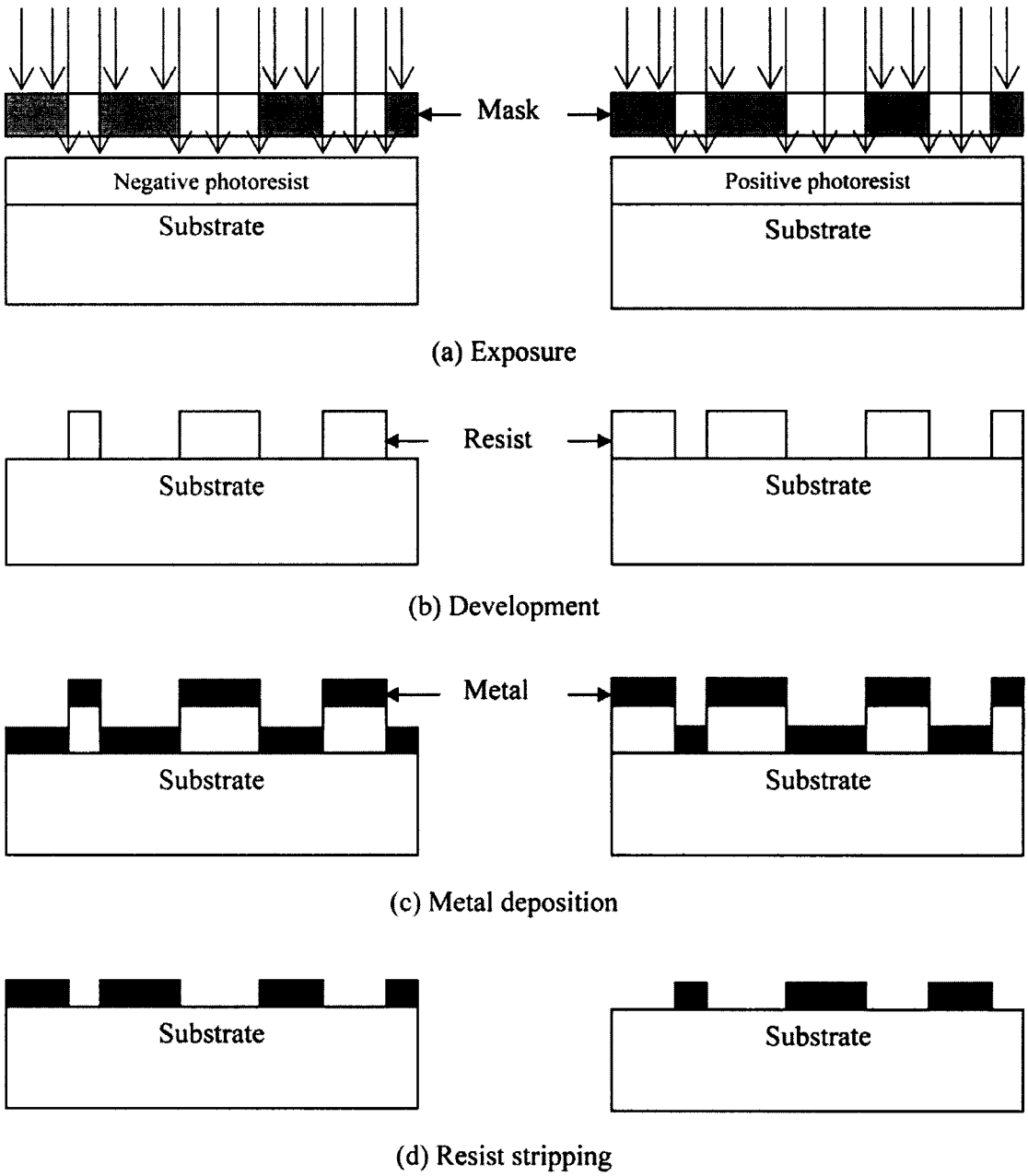

Figure 1.1: Photolithographic process for selective deposition of metal on a substrate. For a positive resist, the exposed portion of the resist washes away during the developing process while the unexposed remains on the substrate. The opposite happens for a negative resist.

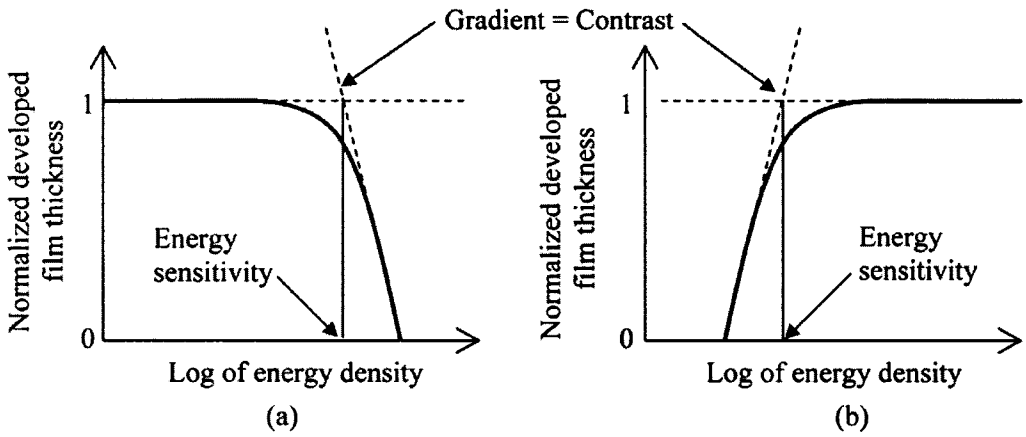

Figure 1.2: Typical photoresist's response to developer at different exposure dose (a) for positive resist and (b) for negative resist.

1.1.4 Two photon absorption process

In a Two photon absorption (TPA) process, the absorption is proportional to the square of the intensity. TPA is also a material dependent process and the TPA coefficient, β, relates the absorption to the intensity of the laser beam in the material. Absorption per unit length due to TPA is

$$\frac{\mathrm{d}I}{\mathrm{d}z} = -\beta I^2 \tag{1.5}$$

when the intensity change while propagating through a short distance is small it can be approximated by,

$$I_i - I_t \approx \beta \Delta d \, I_i^2 \tag{1.6}$$

where, I_i and I_t are the incident and transmitted intensity. Typical values of β are very small (in the order of 10^{-13} m/W) and it requires a very high intensity laser to have significant absorption in the material. Absorption in a material is also expressed in term of absorption cross-section. The absorption rate i.e. number of photons absorbed per unit time, N_2, due to TPA by a pulsed laser can be expressed as [9],

$$N_2 = \delta C \, \frac{P_a P_p}{(h\nu)^2} \, \frac{\Delta d}{A} \tag{1.7}$$

where, δ is the TPA cross-section (m^4 s photon^{-1} molecule^{-1}), P_a is the average beam power, P_p is the peak beam power (W), C is the concentration (molecules m^{-3}) of the material, Δd is the interaction length (m), A is the cross-sectional area of the beam (m), h is the Planck's constant and ν is the laser frequency. The peak power P_p can be determined as $P_p = P_a/R\tau$, where R is the repetition rate (pulses s^{-1}) and τ is the pulse width (s) the laser. SPA cross-section, σ can be also used to determine absorption in the material due to SPA process as,

$$N_1 = \sigma\, C \frac{P_a}{h\nu} \frac{V}{A} \tag{1.8}$$

where, V is the laser probe volume (m^3) assuming a cylindrical geometry.

The absorption rate, $N_{1\alpha}$, in a material with thickness Δd for the SPA process can be determined from Equation 1.1 as

$$N_{1_\alpha} = \alpha \frac{I}{h\nu} \Delta d\, A \tag{1.9}$$

The equation can be rearranged using $V = \Delta d\, A$ and $I = P_a/A$ as

$$N_{1_\alpha} = \alpha \frac{P_a}{h\nu} \frac{V}{A} \tag{1.10}$$

Comparing Equation 1.8 and 1.10 it is evident that

$$\alpha = \sigma\, C \tag{1.11}$$

Similarly the absorption rate, $N_{2\beta}$, for a TPA process can be calculated using Equation 1.5 as

$$N_{2_\beta} = \beta \frac{I^2}{h\nu} \Delta d\, A \tag{1.12}$$

The equation can be rearranged to establish the link between β and δ as

$$N_{2_\beta} = \beta \frac{P_p^2}{h\nu} \frac{\Delta d}{A} \tag{1.13}$$

Now, comparing Equation 1.7 and 1.13 β can be expressed in terms of δ as

$$\beta = \delta \frac{C}{h\nu} \frac{P_a}{P_p} \tag{1.14}$$

As mentioned earlier that $P_p = P_a/R\tau$.

1.1.5 TPA writing, a better tool for 3D fabrication

As mentioned earlier, the TPA process depends on the intensity of the beam. If a laser beam is focused to a point with a microscopic objective lens, as shown in Figure 1.3(a), a focused spot with high photon density is formed locally, with the total number of photons at every cross section being constant. The integrated intensity of a plane at a given position along the direction of the beam is a constant, as shown in Figure 1.3(b). This means that the linear response of the material to the light intensity based on single photon absorption does not have optical sectioning capability since the total integrated flux delivered to one plane will be the same as any other plane and thus all planes are exposed simultaneously to the same degree. On the other hand, if the material response is proportional to the square of the photon density, the time-integrated material response is enhanced at the focused position [Figure 1.3(c)]. One more advantage of TPA process is that generally absorption for a single photon is insignificant and thus light can penetrate more deeply inside the substance using a TPA process. Additionally, the fact that there is only small absorption of energy, at the region where photochemical reaction is not desired, protects material from permanent damage that may occur due to successive absorption of energy even though the intensity is lower than the threshold.

1.1.6 Photonic band-gap crystal

3D structures like micro-mechanical devices and photonic crystals can be produced using the TPA process. A photonic crystal is a periodically repeating structure made of two materials of different dielectric constants that reflects a narrow frequency band of the incident signal. Opals are the example of natural photonic crystals that produce brilliant colors by reflecting a narrow spectrum of light incident on them.

Generally, the length of periodicity of a photonic crystal is about one-half of the wavelength of the light. In such a case, photons tend to interact very strongly with the periodically repeating structure through constructive or destructive interference. The characteristics of this interaction can be artificially controlled by varying the lattice

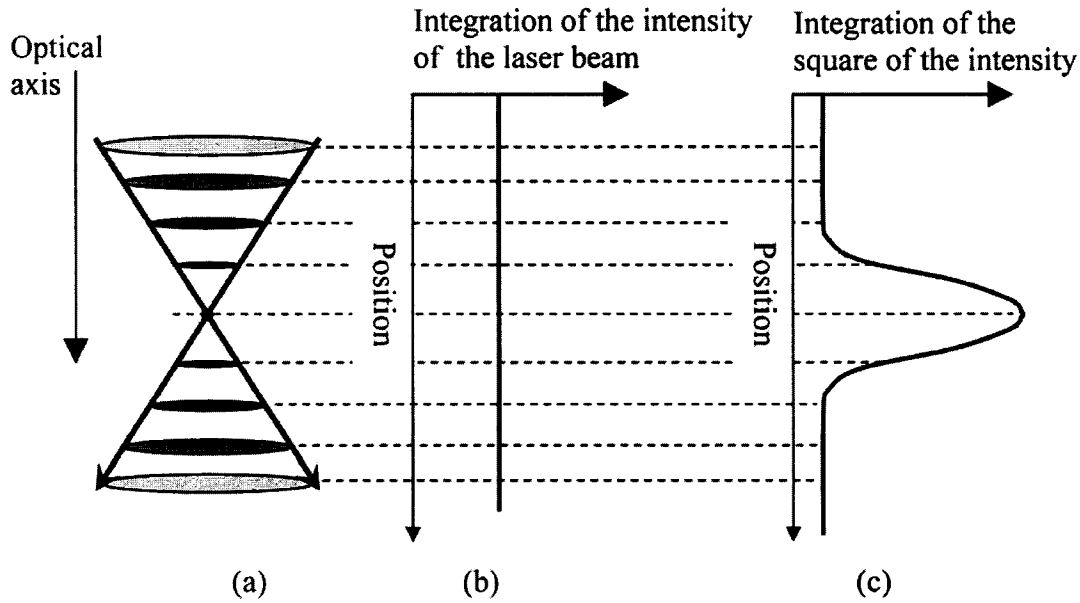

Figure 1.3: Demonstration of 3D writing possibility using TPA process. (a) Intensity variation for a focused beam (b) total SPA probability in each plane along the propagation direction for the focused beam (c)Total TPA probability in each plane along the propagation direction for the beam. [1]

constant, the dielectric constant, and the structure of the lattice. Photonic crystal structures can be used to produce tight bending waveguides, Y-junctions, filters and laser cavities [10, 11, 12].

1.2 Development of TPA writing to date

Currently, a lot of research work is being devoted to fs laser material processing, either in transparent solids or in liquids. One main challenge is to make novel photonic devices by fs laser machining in glass, a most widely used optical material. Unfortunately for most glasses, the linear absorption of near infrared (NIR) light (the working wavelength of a Ti:Sapphire laser) is negligible as their absorption edges are located in the UV spectral region. The laser-matter interaction is therefore based on multiphoton absorption of NIR light. But the very high photon fluences required to achieve

multiphoton absorption may also induce voids or cause irregular volume damage as the refractive index increases proportional to the local intensity of the beam due to the third order non-linear effect causing self focusing in the material. Utilizing the nonlinear effect on material Watanabe et al. [13] and Glezer et al. [14] proposed 3-D memory bits using laser-induced spots; Miura et al. [15] demonstrated light guiding in a direct laser written waveguide Furthermore, Sikorski et al. [16] observed a 3 db/cm gain at 1062 nm from an active waveguide inside neodymium-doped glass substrate. Sun et al. [17] utilized the single pulse produced voids as photonic atoms to organize photonic crystals.

Beside glasses, resists used for lithographic processing have also been studied for microfabrication using two or multiphoton absorption. S Katayama et al [18]-[19] studied the structures for diffraction gratings produced due to irradiation of NIR (800 nm, 150 fs) laser pulses in various polymeric materials. Examples of such polymeric materials includes polymethyl methacrylate (PMMA), thermoplastic epoxy resin (Epoxy) and a block copolymer of methyl methacrylate and ethyl acrylate-butyl acrylate [p-(MMA/EA-BA) block copolymer] doped with dyes, which either had or did not have absorption at 400 nm wavelength [18]. No structure was produced in undoped polymers. Diffraction line gratings were produced in PMMA and p-(MMA/EA-BA) block copolymer doped with dye having absorption at 400 nm by scanning the beam. Polysilane and polysilane coated epoxy and PMMA films were also studied by the same group [19] to produce diffraction gratings using similar optical system.

Liquid-phase photochemical reactions induced by fs laser pulses in a small volume can also produce polymer-based micromechanical or MEMS systems and optoelectronic/photonic devices. Polymers as optoelectronic/photonic materials are available for various wavelengths covering the entire visible to NIR range. These polymers are simple to process and allow for doping and molecular design to realize various optical functions.

Maruo et al [1] first reported 3D microstructure produced by TPA polymerization using a highly viscous liquid resist. A laser beam from a 790 nm wavelength, 200

fs pulse width, 76 MHz repetition rate Ti:Sapphire laser oscillator was focused into SCR-500 resin. The resin was a mixture of urethane acrylate oligomers/monomers and photoinitiators. A 0.85 numerical aperture (NA) oil immersion microscope objective produced spirals with a diameter of 7 μm and an axial pitch of 10.3 μm. The width and height of the spiral, were approximately 1.3 μm and 2.2 μm, respectively. Kawata et al [20] from the same research group demonstrated complex micro-structures using the same resin. They used 780 nm , 150 fs pulse width, 76 MHz Ti:Sapphire laser oscillator pulses and 100x objective lens with a NA 1.4 to focus the beam. The laser was scanned horizontally by a galvano mirror set and vertically by a piezo electric stage. Several microstructures such as a micro-gearwheel, micro-chain, micro-spring, micro-tube and micro-bull were presented in the article. Spatial resolution for the fabrication process was defined as the dimensions of the smallest achievable volume in which photochemical reaction can occur while the surrounding region was not affected. The best longitudinal and lateral resolutions reported in that article were 120 and 500 nm, respectively.

Some other groups proposed different photoresists or polymers with photo-acid generator for 3D fabrication. Kuebler et al [21] proposed a new photo-acid generator (PAG) with higher TPA cross-section that could reduce the required exposure time for faster processing or lower threshold intensity in order to avoid damage during TPA writing. The two-photon-activable PAG BSB-B_2 consists of a *bis*[(diarylamino)styryl]-benzen core with covalently attached sulfonium moieties. The *bis*[(diarylamino)styryl]-benzen possesses a high TPA cross-section of 805 $\times$ 10^{-50} cm^4 s $photon^{-1}$ [21] with a peak in the near infrared (745 nm) wavelength. The TPA cross-sections for conventional initiators are typically 10 $\times$ 10^{-50} cm^4 s $photon^{-1}$. The PAG BSB-B_2 was used in conjunction with the solid negative epoxide resist, Epon SU-8 for 3D microfabrication. It was also mixed with a chemically amplified positive resist, tetrahydropyranyl methachrylate (THPMA)-methyl methacrylate (MMA)-methacrylic acid (MA). 3D structures reported in the article had a limiting resolution of more than a micron resolution when using a 60x, 1.4 NA objective. A 745 nm Ti:Sapphire laser oscillator with 80 fs pulse width and 82 MHz repetition rate at an average power of 3.5 mW

was used in that experiment.

Kou et al [22] reported 3D structures in a hyper branched polyester acrylate (HPEA) with a maximum resolution of 0.85 μm. The HPEA was mixed with 1, 6-hexanediol diacrylate (HDDA), Ti-tanocene derivative (Irgacure 784) and *p*-Hydroxyanole at three different ratios to produce three different formulation A, B and C. The Irgacure 784 and *p*-Hydroxyanole worked as a photoinitiator and photoinhibitor, respectively. As mentioned in the article the presence of the photoinhibitor along with the initiator greatly increased the threshold value of the TPA polymerization. A mode-locked Ti:Sapphire laser (Coherent Mira 900F) was used in the experiments. The laser pulses with 80 fs pulse width, 800 nm wavelength at 1 KHz repetition rate was focused using a 100x, 1.22 NA microscope objective. They reported significant reduction of TPA threshold for the oligomer compared to SCR-500 resin used to write structures with highest resolution ever. The threshold for three different formulations were 2.9, 4.3 and 1.6 $\times 10^{7}$ mJ cm^{-2} [22], respectively, where the parameter for SCR-500, resist used for highest resolution ever, was 1.8 $\times 10^{12}$ mJ cm^{-2} [1]. The resists also had wide windows of laser power to operate as the ratio of thresholds between breakdown to TPA writing were 3.7, 4.3 and 3.4, respectively. Single rods were fabricated with a laser spot scanning at a speed of 20 μm s^{-1} and the structures were studied to find the TPA parameters. Simple lines and microgears were fabricated by the group to demonstrate 3D writing capability.

Ormocore, a commercially available photoresist, was also used to produce 3D structures by Serbin et al [23]. The fabrication process for the resist is simple and the resist is bio-compatible. A Ti:Sapphire laser oscillator was also used in their experiments with 80 fs pulse width and 80 MHz repetition rate. The operating wavelength of the laser was 780 nm and the laser beam was focused using a 100x microscope objective with 1.4 NA. The structures were written with an average beam power of 30 to 60 mW. The effective TPA cross-section of the resist, defined as the product of the ordinary two-photon absorption cross section, δ, and the efficiency of the initiation process, η (<1), was report as 3 $\times 10^{-55}$ cm^{4} s photon^{-1} [23]. Variation of voxel (volume element) height and width with exposure time and power were utilized

to determine the parameter. Minimum dimension of voxel height and width reported by the group were 550 nm and 150 nm, respectively. The focal point of the laser beam was scanned in the material in longitudinal direction using a galvo scanner and in lateral direction using a piezo stage to write complex 3D structures. Structures like a miniature statue of Venus, wood-pile photonic crystal structure, and micro-capsules were fabricated by the group.

SU-8 is a common negative ultra violet (UV) photoresist widely utilized for fabrication of high aspect ratio micro-structures. The resist is a solid coating after prebaking and there are several advantages of working with a solid coating. Neglible density difference between exposed and unexposed zone makes the pattern steady in its position. Relative position of the exposed volume in the photoresist remains unchanged for vibration of the substrate. For these reasons SU-8 is becoming popular for 3D fabrication even though the resist is very temperature sensitive and the processing of the material is more complex and time consuming.

Three dimensional structures were produced on a single shot basis by G. Witzgall et al [24] using commercial SU-8 based on the TPA process. A regeneratively amplified Ti:Sapphire laser system (Spectra Physics) was used for the fabrication. A slightly elliptical beam with beam diameter 4 mm $\times$ 5 mm was focused using a 25 mm lens. The primary objective of the paper was to explore the possibility of single shot 3D structure writing. The pulses with 120 fs pulse width, maximum 1 mJ pulse energy at 800 nm and 500 Hz repetition rate laser produced a 3D circular spiral with 4 μm width wall and the maximum height of the spiral was 80 μm. During the scanning one rotation stage rotated the substrate while moving away or closer to the beam focus. For 800 nm laser the TPA exposure and damage threshold for single-shot writing were 3.2 and 8.1 TW/cm^2, respectively. The adhesion problem of SU-8 on glass was solved by overlaying the resist on top of a thermally cured SU-8 layer.

Lee et at [25] fabricated sub diffraction limited structures with high-aspect ratio using commercially available SU-8 resists. A Grating like structure with widths smaller than 300 nm and an aspect ratio of nine were was fabricated by the research group. Two dimensional periodic structures with posts of 1.2 μm height and 460

nm diameter were also constructed in SU-8. These were also transferred to silicon using reactive ion etching and the height and width were reduced to 800 nm and 150 nm. A modelocked Ti:Sapphire laser oscillator with 100 fs pulse width at 808 nm wavelength and 100 MHz repetition rate was used for TPA writing. The laser pulses were focused using a 60x microscope objective having a NA of 0.85. A thin 2 μm thin layer of SU-8 was coated on silicon wafer by spin coating. The substrate was moved by a three-dimensional piezo stage with 10 nm resolution and 50 nm repeatability.

Another investigation on the production of ultra-high aspect ratio patterns was reported by Teh et al [26]. The resolution of voxels and lines produced on SU-8 were studied as a function of laser-pulse energy, exposure time and scanning speed. A Ti:Sapphire laser was also used for TPA fabrication with 795 nm wavelength, 70 fs pulse-width and 80 MHz repetition rate. Low NA (0.3), 10 times objective focused the beam with an average power of 40-100 mW to a silicon substrate coated with SU-8 resists. A thin 975 nm layer of resist was produced by spin coating at 6000 rpm for 30 seconds and used for 3D writing characterization. A piezo stage on top of an x-y translation stage was used to hold and scan the sample in the laser beam. The minimum voxel diameter and line width reported in the literature are around 1 μm. High-aspect ratio structures were also produced in thick layer of SU-8 having thickness up to 500 μm . The group reported vertical planes with maximum aspect ratio of 23:1 and pillars with aspect ratio of 50:1. The width for these structures were around 10 microns. 3D structures like suspended bridges of various lengths, microflaps, cantiliver rods, and cages were fabricated by the research group.

A 3D photonic crystal structure using square-spiral architecture was reported by Seet et al [27]. A 50 μm thick SU-8 layer was used to fabricate the structure using 100x, 1.4 NA objective and 800 nm, 130 fs, 100 Hz repetition rate Ti:Sapphire laser system operating. The minimum diameter of the voxel produced in SU-8 was 475 nm and the laser beam was scanned by moving the substrate placed on a 3D piezo-stage.

The following few paragraphs covers other fabrication techniques besides TPA writing for 3D structure writing. The performance reported such as aspect ratios or minimum feature size using a few resists are also mentioned for these processes

and other 2D fabrication processes. LIGA (German: Lithografie, Galvanoformung, Abformung) process is also used for 3D microstructure writing. In LIGA, synchrotron X-ray radiation is passed through a mask and the transmitted X-rays are used to expose a pattern in a resist [28, 29]. One of the initial goals of the process was to manufacture extremely small nozzles, a high aspect ratio structure, to separate uranium isotopes. Polymethyl methacrylate (PMMA) is a widely used resist for X-ray lithography. An aspect ratio as high as 87.5:1 (350 μm: 4 μm) is reported by Becker et al [28]. The minimum dimension produced by the lithography process was around 0.5 μm. In order to make 3D structures using the technique several fabrication steps are required [29, 30]. Griffiths [31] calculated the minimum feature size based on the properties of the PMMA and other physical limitations of the source. The minimum possible size for positive linear structures as mention in that paper were 0.5 μm and 2 μm for a 100 μm and 1 mm thick resists, respectively. The corresponding maximum possible aspect ration for these thicknesses are about 200 and 500. Although the technique has been used for some years now, LIGA remains expensive because of the high cost of the synchrotron accelerator. SU-8 resists was primarily developed for lithography with low flux synchrotron radiation. Bogdanov et al [32] reported structures with aspect ratio as high as 100 (400 μm: 4 μm) using x-ray lithography. A UV-LIGA process was also used to fabricate 3D structures in PMMA [33].

Another technique to produce 3D micro-structure is called stereo lithography. The technique allows the manufacturing of 3D parts by a light-induced spatially resolved polymerization [34]. In the stereo lithographic process several layers of photoresist were coated and focused UV light is used to expose one layer after another. Normally the stage is moved so that the focus moves to the next layer after exposing a 2D pattern in a layer. Ikuta et al [34] demonstrated structures with an aspect ratio greater than 10 and the minimum dimension of a cell is 5 μm $\times$ 5 μm $\times$ 3 μm.

Deep ion beam lithography (DIBL) using MeV protons, is a technique that can be also used produce 3D structures in both positive and negative resists. DIBL is a direct writing technique and no mask is required for this process. Sanchez et al [35] reported structures with aspect ration of 100 in PMMA using the technique. Kan

et al [36] produced a grid of lines above the substrate supported by vertical planes. The planes were written by 2 MeV protons that penetrates up to the substrate while the grid was produced utilizing undercut of the structure with 0.6 MeV protons. The minimum width of a line/wall produced in SU-8 is around 100 nm produced using 100 KeV protons as reported in [37]. The resist thickness or the line height was 0.25 μm for the structure. Ion beam LIGA has been applied for PMMA for 3D structure writing with high aspect ratio ($\approx$40) by Munnik et al [38].

SU-8 is also widely used for conventional UV-lithography for high aspect ratio structure writing. The highest aspect ratio reported using UV-lithography is 190:1 (1150 μm: 6 μm) by Yang et al [39]. Glycerol was used between the mask and the solid SU-8 resist to compensate effects of air-gap between these layers.

Several publications report on models to predict final structure based on the exposure dose, resist characteristics and other parameters. Griffiths [31] defined the limiting features of PMMA for the LIGA process. Moreover, Tina et al [40], Yang et al [39] and Reznikova et al [2] simulated the deep UV lithography process for SU-8 based on material and process parameters.

1.3 Summary

The TPA process has opened a window for 3D fabrication with a huge possibility of miniaturization. Different photonic and mechanical devices can be written with nanometer resolution with less complexity compared to the multistep conventional 2D fabrication process.

The unit block of a 3D structure, Voxel, can be of different aspect ratio based on the objective used to write it. For higher magnification objectives the ratio between width and height of a voxel is smaller compared to the that produced using lower magnification objective. Thus, high magnification objectives, for example 100x, will produce more spherical voxels which is better for complex 3D structure writing. On the other hand, lower magnification objective will produce more column shaped voxels, better to write high aspect ratio structures.

The maximum spatial resolutions reported to date were different for different materials used as well as for different techniques applied. In most cases Ti:Sapphire lasers with wavelength of 780 to 800 nm were used for microfabrication using TPA. 100x objective with around 1.4 NA objective was used for high resolution 3D structure writing. To date, the maximum resolution reported using TPA photopolymerization process is 120 nm demonstrated by Kawata et al [20] using SCR 500 resin. The height of such a small voxel was around 500 nm. The minimum width and corresponding height for the Ormocore are 150 nm and 550 nm [23]. SU-8, a solid resist before exposure, can produce voxels of 300 nm with a aspect ratio of nine using TPA writing [25]. High aspect ratio pillars (50:1) and planes (23:1) were produced in SU-8 using 10x objectives with widths close to ten microns [26]. Complex structures were also produced by research groups to demonstrate 3D writing capability.

In the present thesis high aspect ratio structures with nanometer scale resolution using two commercially available resists are reported and experimental details to characterize the resists are also presented. The TPA coefficients that determine the absorbed energy due to TPA process were determined. The effective or reaction TPA cross-section of Ormocore measured from variation of voxel dimension was reported by Serbin et al [23]. Moreover, the etch rate for different absorbed energy were characterized based on SPA phenomenon. Parameters reported in this work can be used in the future to predict the final structures produced using TPA writing.

The rest of the thesis is arranged as follows. Chapters 2 and 3 describe the experiments used to characterize the resists for the SPA and TPA processes. Etch rate variations with absorbed energies are experimentally determined using the UV-lithographic process in Chapter 2. Chapter 3 presents the TPA coefficients for the resists determined using standard methods. Chapter 4 reports different 3D structures produced using the TPA process and characterizes 3D writings for different control parameters. Finally, Chapter 5 summarizes the results and observations and suggests future directions for improved performances.

Chapter 2

Single photon absorption experiment

In a standard lithographic process single photon absorption (SPA) phenomenon, as mentioned in section 1.1.2, is widely used to transfer patterns to the photoresists, coated on the substrate. The photoresists are exposed using a narrow bandwidth light source of particular wavelengths with uniform spatial distribution. The resists that have significant absorption in that wavelength are exposed in a selective manner using an optical mask to produce different 2D structures. After exposure the resists are developed using a suitable developer. The developer etches away either exposed or unexposed portions of the sample depending on the type of the resists. This etch rate is dependent on the absorbed energy per unit volume of the photoresists. In this chapter experimental procedures are reported to find the dependency of the etch rate on the absorbed energy.

Absorbed energy in a sample due to SPA process can be easily calculated from the SPA coefficient, the intensity of the light source and the exposure time as mentioned in section 1.1.1. The exposure time is a suitable parameter for controling the absorbed energy. For an insignificant change of SPA coefficient of the material over the exposure, the absorbed energy can be considered a linear function of exposure time. Straight line arrays with different widths are exposed for different time during the SPA based fabrication process. Final dimensions of the transferred pattern for

different exposures were measured using a surface profilometer. The final dimensions are related to the etch rates of the photoresists that should vary with the absorbed energy. Finally, a correlation between absorbed energy and etch rate of the photoresists in the developer is established.

2.1 Energy absorbed in a SPA process

Absorbed energy in the photoresists for a SPA process is dominated by two phenomena, reflection at different surfaces and absorption inside the medias. A finite reflection at the transition surface of two materials having different refractive indices reduces the transmitted power to the next material. Moreover, the absorption coefficient for a material along with its thickness plays a vital role in determining how much energy will be absorbed(Section 1.1.1) inside the material.

Fresnel reflectance, R, at the surface of two materials having refractive index $n_1(\lambda)$ and $n_2(\lambda)$ for perpendicularly incident light can be expressed as,

$$R(\lambda) = \left[\frac{n_1(\lambda) - n_2(\lambda)}{n_1(\lambda) + n_2(\lambda)}\right]^2 \tag{2.1}$$

Transmittance through the surface is defined as 1-$R(\lambda)$. So, the transmittance in term of refractive index is,

$$T(\lambda) = 1 - \left[\frac{n_1(\lambda) - n_2(\lambda)}{n_1(\lambda) + n_2(\lambda)}\right]^2 \tag{2.2}$$

As seen in the equations, both transmittance and reflectance is a wavelength dependent parameter.

Let us consider a generalized arrangement of materials for the SPA experiment performed to find the etch rate of the resists for different energy exposure. Figure 2.1 shows different layers of materials arranged in a manner to represent the SPA experiment. There was an intermediate layer of air for Ormocore since it was fabricated using proximity-printing process. On the other hand, SU-8 was exposed using contact printing and there is no intermediate layer to represent the arrangement. Another layer of SU-8 can be considered as an intermediate layer while calculating the

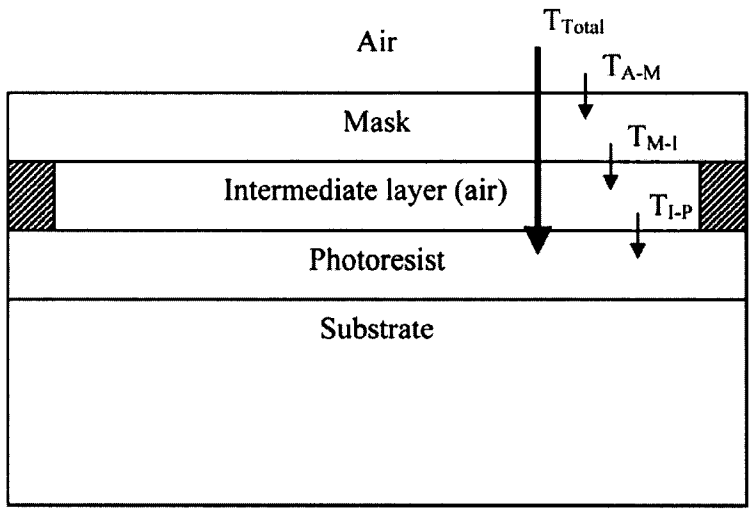

Figure 2.1: Generalized layer-assembly for the SPA experiment. A layer of SU-8 may be considered as the intermediate layer for analyzing transmission for SU-8 since the resist is exposed using the contact-printing process.

transmittance. Total transmittance into the resist can be calculated by multiplying the transmittance at different surfaces as,

$$T_{Total}(\lambda) = T_{A-M}(\lambda) \times T_{M-I}(\lambda) \times T_{I-P}(\lambda) \tag{2.3}$$

where T is the transmittance and the subscript A, M, I, and P represents the air, mask, intermediate and photoresist layers, respectively. The back reflection from the photoresist to glass interface is neglected because of the insignificant refractive index mismatch. The absorption inside the mask and intermediate layer is also neglected. The transmittances are function of wavelength as mentioned before. So, for a light source with a spectral intensity (per unit wavelength) distribution $S(\lambda)$, the incident spectral intensity energy on the resist, $I_0(\lambda)$, is simply

$$I_0(\lambda) = T_{Total}(\lambda) \times S(\lambda) \tag{2.4}$$

The absorption coefficient, α, of a material also varies with the wavelength of the incident light. If a materials of thickness, Δd, absorbs $E(\lambda)$ amount of energy per unit area per unit wavelength for an incident intensity $I_0(\lambda)$ then

$$E(\lambda) = I_0(\lambda) t_{\exp} \left[1 - \exp\left(-\alpha(\lambda)\Delta d\right)\right] \tag{2.5}$$

where t_{exp} is the exposure time. From the Equation 2.5 it is evident that absorbed energy in the resist can be varied linearly by varying the exposure time. $E(\lambda)$ can be also calculated from absorption in dB/m, α_A, using

$$E(\lambda) = I_0(\lambda) t_{\text{exp}} \left(1 - 10^{\frac{\alpha_A \cdot \Delta d}{10}}\right) \tag{2.6}$$

2.2 Experimental details

In order to characterize the photoresist using SPA process we need a suitable optical source that has a spectrum within the absorption band of the resists. An ultraviolet (UV) source with uniform spatial distribution is used in the experiment since the resists absorb lights below 400 nm wavelength. A mask with arrays of lines of different width was used to transfer the pattern. Finally, a high-resolution profilometer, AlphaStep 200, was used to obtain the information regarding height and/or width of the transferred pattern on the photoresists.

2.2.1 Light source

A UV light source together with a mask aligner was used for SPA experiments for two photoresists, Ormocore and SU-8. Both of the resists are commercially available resists and widely used for two photon absorption writing. The performance of the light source of UV mask aligner named 'Oscar' (manufactured by AB-M) at the NanoFab of the University of Alberta, was analyzed to determine the absorbed energy by the resists.

Spectra of the light source

The UV source is designed for light emission at 365 nm and 405 nm wavelength. Mercury and Xenon lamps inside the system produce light of several discrete wavelengths in the UV region. An Ocean Optics spectrometer (USB 2000, #2, minimum resolution 1.34 nm) was used to find the spectrum of the source. Figure 2.2 shows the spectrum with clear peaks at 365 nm, 405 nm, 437 nm and minor peaks at 550

nm and 582 nm as reported by other researchers [2, 39]. The spectrum was corrected for efficiency of Ocean Optics (Appendix A.1) at different wavelengths.

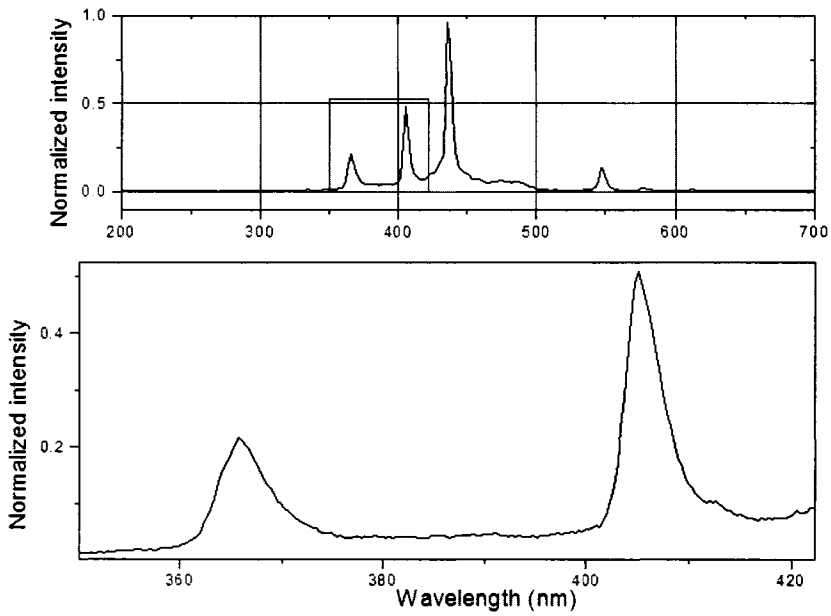

Figure 2.2: Spectra of Mask Aligner's UV source('Oscar').

Uniformity of the source

Uniform distribution of light intensity over the substrate is important especially for a four square inch substrate used in the experiment. The NanoFab source specifies intensity distribution within 6% over the four square inch substrates. A power meter, specially calibrated for 365 and 405 nm wavelengths, is placed in different locations of the substrate holder to carry out the intensity measurements. Figure 2.3 shows an example of the typical performace of the source for those two wavelengths.

Intensities at different wavelengths

The line widths of the UV source at the operating wavelengths are wide and there are lines with wavelengths other than the specified operating wavelengths as shown in the spectrum of the UV source (Figure 2.2). Moreover, there is background continuum

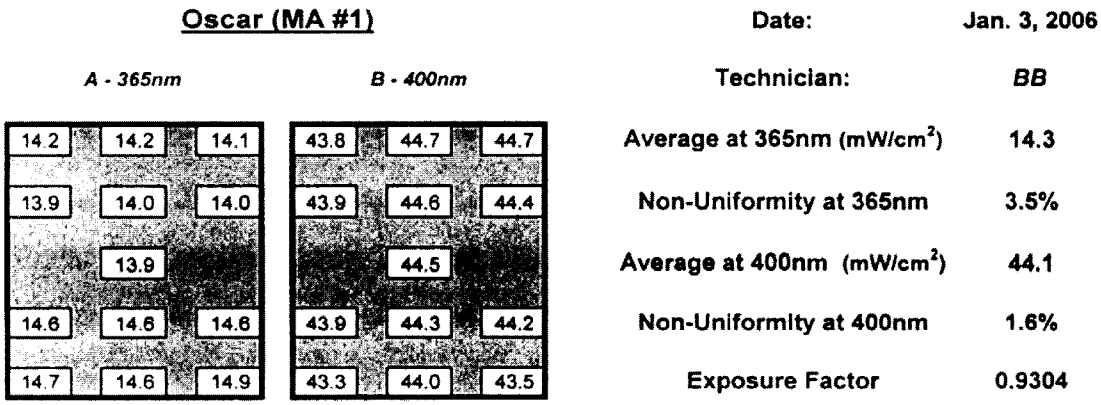

Figure 2.3: Uniformity of Mask Aligner's UV source('Oscar').

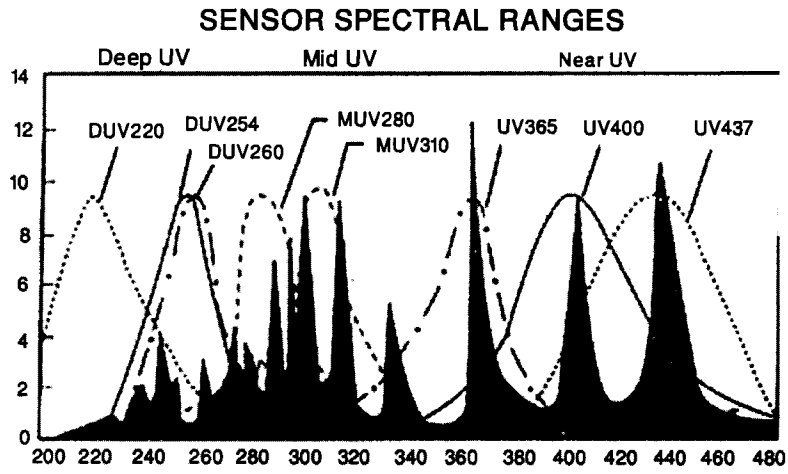

Figure 2.4: Relative intensities of different UV-sources and spectral ranges of different power meters supplied by the manufacturer. Power meters for 365 nm and 405 nm were used in the experiment.

between two peaks which may lead to significant contribution to the absorption especially, for the radiation between 365 and 405 nm. So, it is important to determine the intensities at different wavelengths. The spectrum obtained by the spectrometer can be scaled to get the intensity distribution at different wavelengths.

The NanoFab provides information about the power measured at 365 nm and 405 nm. Two different settings were utilized for these measurements and the normalized sensitivity of these two options for different wavelengths was taken from the manufacturer specification. Figure 2.4 shows relative source intensities and spectral ranges of the sensors or power meters for different sources and power meters supplied by the manufacturer. As shown in the figure the sensitivity of a particular sensor is relatively wide. The normalized spectrum of the UV source used in the experiment was scaled to give the total intensities integrated by the power meters to match the measured values. The resulting scaling factor was different ($\approx 30\%$) for 365 nm and 405 nm power meter to match the power measured at these wavelengths. The scaling factor for 365 nm was considered for the experiment since the resists have more absorption at this wavelength. Scaling factors were 2.84 and 2.59 for the experiments on Ormocore and SU-8, respectively. Performing the experiments on two different days caused the power variation of the UV source. The intensity distributions during the experiments for Ormocore and SU-8 are given in Figure 2.5 and 2.6.

2.2.2 Fabrication process

0211 glass substrates cleaned with Piranha etch (H_2SO_4:H_2O_2 3:1) were used for both SU-8 and Ormocore sample. Acids were produced by J. T. Baker and concentrations of H_2SO_4 acid and H_2O_2 were 51% and 30%, respectively. The substrate was also dried and baked at 200°C for a minute to drive away the moisture. A 50 μm layer of SU-8 from MicroChem Corporation was coated on the substrate by spinning the photoresist at 3000 rpm. The detailed parameters for spin-coating for the resists are given in Table 2.1. The substrate was then prebaked at 65°C for 3 minutes and at 95°C for 6 minutes according to the manufacturers recommendation. It was then exposed for different time periods using the UV mask aligner 'Oscar' as mentioned

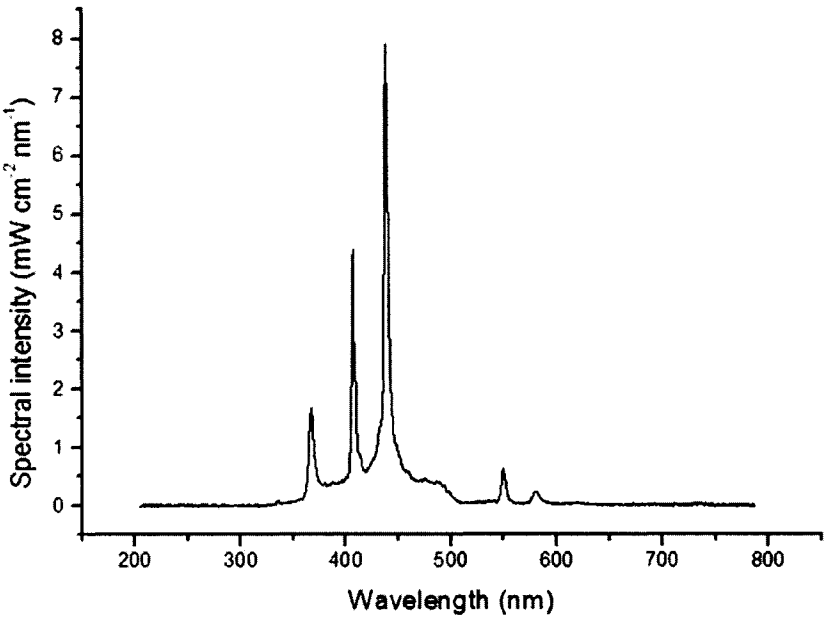

Figure 2.5: Incident spectral intensity versus wavelengths for Ormocore exposure experiments.

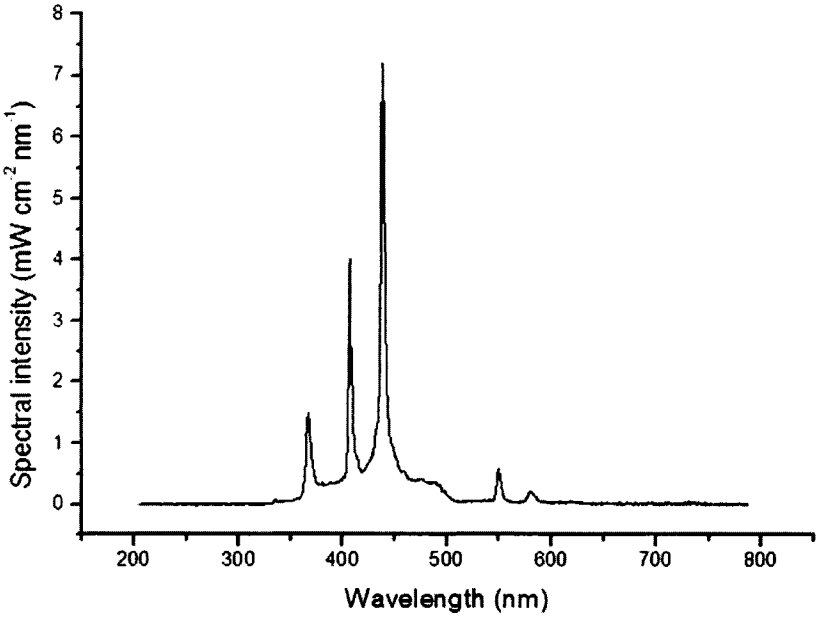

Figure 2.6: Incident spectral intensity versus wavelengths for SU-8 exposure experiments.

in section 2.2.1. Post exposure baking was 1 minute at 65°C and 5 minutes at 95°C. Then it was developed for 4 minutes in SU-8 developer, Methoxy 2-propanol acetate, rinsed with isopropyl alcohol (IPA) and dried out by N_2 gas flow. SU-8 had poor adhesion to glass and that problem was solved by adding an extra thin layer of XP Omnicoat between the SU-8 and glass. This additional thin layer was coated at 3000 rpm (see, Table 2.1 for details). The adhesive layer was hard baked for 1 minute at 200°C. The adhesive layer was around 1 μm thick. The adhesion layer remained on the substrate after all the processing.

Ormocer is designed for proximity printing and the NanoFab only provides facilities for contact printing. Ormocore is not solid or a hard material after pre-baking. This makes it difficult to process using contact lithography technique. This viscous material gets squeezed when the mask is pressed on top of the layer during contact printing. Moreover, there is a large possibility of deformation of the transferred pattern while removing the mask since the resist tends to stick to the mask.

To solve the problem one more step was taken for Ormocore. A 100 μm thick spacer (Myler) was set at the boundary leaving the inside region for the photoresist. At first a 35 μm thick layer was coated on the glass substrate by spin coating at 2000 rpm. The Fresnel diffraction due to the spacing between the resist and the mask is negligible for the designed line-widths greater than 32 μm. [1] After baking the resist for 2 minutes at 80°C the spacer was set on top of it. The spacer was designed to let a small amount of photoresist below the spacer sqeeze out sideways of the substrate when the mask was pressed on top of the the spacer. After exposing the resist to UV light it was developed in OrmoDev for 1 minute and kept in IPA for 15 sec and then left in Deionized (DI) water for about a minute. All solutions were kept at room temperature of 18° C. The resist was then dried by N_2 gas flow.

[1] A Fresnel number, N_F, of 10 gives a reasonable replication of the mask pattern after diffraction. In this case the Fresnel number is defined as $N_F = a^2/(\lambda d)$, where $2a$ is the slit width, d is the spacing between the mask and observation plane and λ is the wavelength. For the calculation λ was 400 nm, d was 65 μm.

Table 2.1: Spin coating settings for coating different photoresists. Ramp is the time to ramp up to the speed mentioned in RPM and then it will rotate at that speed for the time mentioned in the time column. The ramp down time was 4 seconds for all the settings mentioned in the table.

Material	Spinning cycle	Ramp (sec)	RPM (rpm)	Time (sec)	Thickness (μm)
Ormocore	1	5	100	5	35
	2	5	500	10	
	3	5	2000	30	
XP Omnicoat (Adhesive layer for SU-8)	1	5	100	5	< 1
	2	5	500	10	
	3	9	3000	30	
SU-8	1	5	100	5	55
	2	5	500	10	
	3	9	3000	30	

2.2.3 Different time exposure scheme

The main objective of this experiment was to expose the photoresist with different exposure times while maintaining other processing parameters constant. Multiple substrates can be used to expose for different time durations. But it is a time consuming and expensive process for a relatively large number of data sets. Moreover, it is difficult to maintain the same baking temperature and time, as well as developing conditions for all the samples. To solve the problem two masks one with many replicas of the linewidth series exposure pattern and the other with an aperture window for each exposure region are used as shown in Figure 2.7 (a). Dark regions blocked the light and white portions are transparent to the light source. The second mask was simply a thick and opaque board as shown in Figure 2.7 (b).

One block in the mask consists of patterns made up of straight lines with different widths. Line widths varied from 10 μm to 500 μm and the length of the lines was

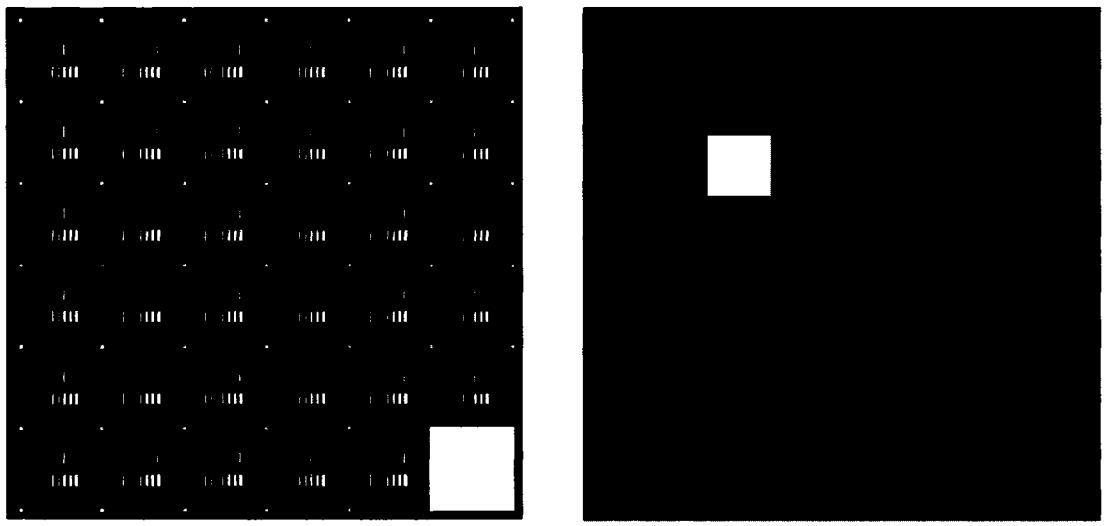

(a) (b)

Figure 2.7: Masks for SPA experiments (a) the mask designed to transfer the pattern to the photoresists and (b) mask to choose the region of the main mask to be exposed.

2000 μm. The width variation ensures several observations for a particular setting. One added advantage of lines with multiple widths is to give more accurate results. For smaller exposure time where etch rate is high, wider lines can survive the etching process and can be useful for finding the etch rate. On the other hand, for larger exposure time, where etch rate is small, the narrower line can provide information about the slightest change as the ratio of original width/height to the final will be more accurate than that for wider lines. The transparent region at the corner of the mask was utilized to find the transmission of the mask for the operating wavelength using a Monochromator (High Speed Monochromator System, HS-190) available at the NanoFab. Wider lines were chosen in the experiments because the etching process can be considered one dimensional, at least at the center of the line.

2.3 Results

As mentioned earlier, the photoresists used in this experiments are negative resists. Therefore, for high energy exposure the resists are not removed during the development process. So, the dimensions of the transferred bar shaped structures should

gradually increase to the design-dimension for higher energy exposure. However, over exposure can cause chemical reaction in the adjacent area of the exposed region resulting in final dimension greater than the designed width.

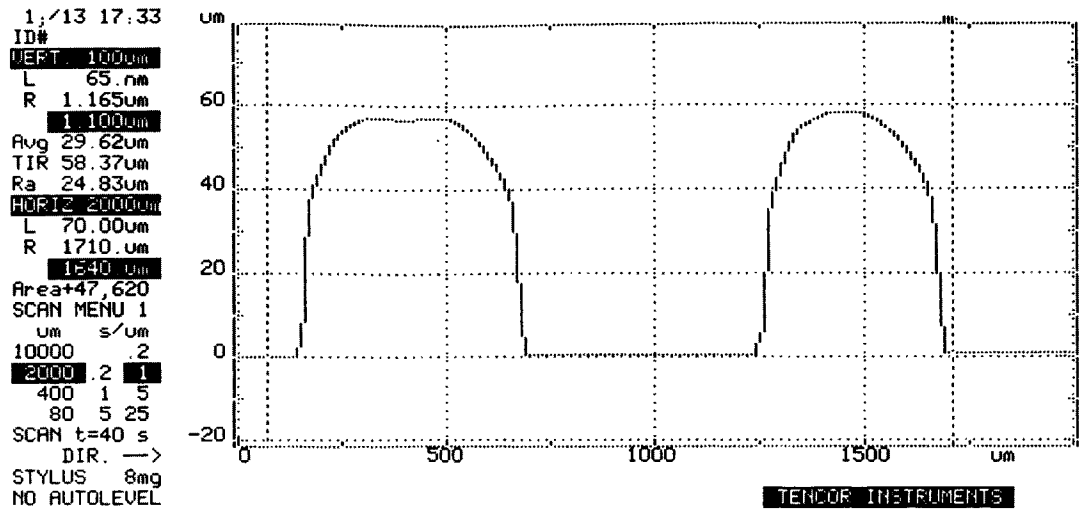

Figure 2.8: Surface profile measured using Alpha Step 200 profilometer. SU-8 bars with design width of 500 and 400 μm were produced by exposing the resist for 5 seconds at the UV source.

2.3.1 Line heights for different exposure time

The surface profile was measured using the Alpha Step 200 contact profilometer available at the Nanofab at the University of Alberta. The device can measure profiles with a $\pm$ 0.25 μm accuracy in height. So, for the dimensions greater than several microns this error is insignificant. The resolution of the profilometer along the width is limited by the dimension of the tip, used to scan the surface. The stylus which can be modeled as a 60° cone rounded to a spherical tip with a 5 μm radius gives a lower limit for the vertical resolution. It also depends on the height and shape of the grooves. The shape of the tip basically limits scanning of a steep change of height. This makes the profilometer more suitable for measuring height between two extended surfaces. An optical profilometer (Zygo) can be also used to record the

surface profile and analyze it after proper calibration. Three samples of each resist were fabricated and similar performance was observed. Heights and/or widths of two different design-widths were collected from one sample for Ormocore. Two samples of SU-8 were measured as there was a rapid transition from no structure to structures with heights equal to the resist thickness. For Ormocore, the transition was gradual.

A typical output of the Alpha Step 200 profilometer is shown in Figure 2.8. The profile presented in the figure is for 500 μm and 400 μm wide bars exposed for 5 seconds in the UV source. Surface profiles of SU-8 at different exposures are given in Appendix A.2 to show the change of the shape of the transferred pattern. Summary plots for heights of the bars due to different exposures are presented in Figure 2.9 and Figure 2.10 for Ormocore and SU-8, respectively.

Final structures remaining on the substrate are obtained after developing for a finite time. The changes in dimensions can be used to determine the etch rate per unit developing time.

2.3.2 Absorbed energies for different exposure time

Refractive indices of two materials define the transmission at the interface surface. Refractive indices of Quartz, SU-8, Ormocore are given in Appendix A.3. The wavelength dependent transmittances were used to calculate the incident intensities on the resists for different wavelengths. The absorption in the material was calculated based on the SPA coefficients or absorption coefficients as described in Section 1.1.1. Figure 2.11 and 2.12 show absorbed intensities versus wavelength for the Ormocore and SU-8 resists, respectively. Total absorbed intensities for Ormocore and SU-8 were 2.7 mW cm^{-2} and 4.13 mW cm^{-2}, respectively. The absorbed intensity or the absorbed energy per unit volume per unit time can be easily found by dividing the the total intensity with the thickness of the resist. For a 35 μm Ormocore layer the absorbed energy per unit volume per second is 0.77 J cm^{-3} s^{-1} while that for SU-8 is 0.75 J cm^{-3} s^{-1} for a 55 μm thick layer. Energy per unit volume can be obtained by multiplying by the exposure time.

The lower intensity values for deep UV-wavelengths were noisy and the noise was

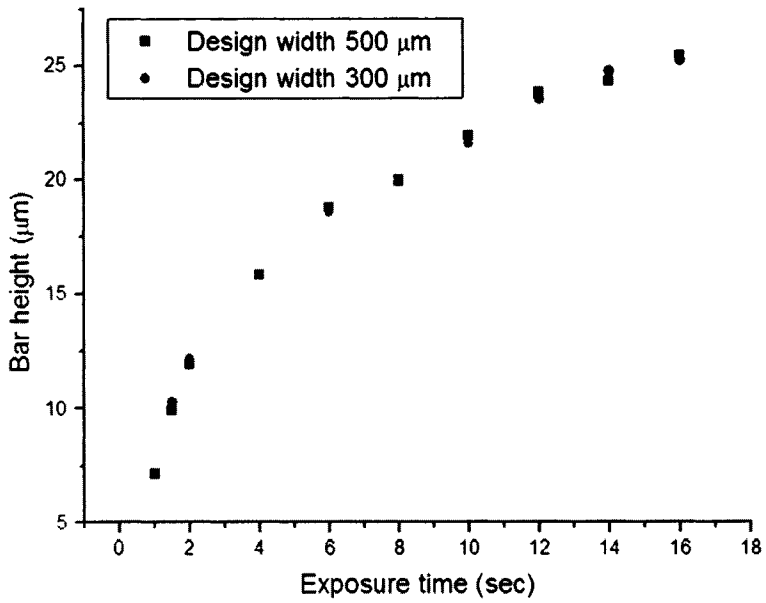

Figure 2.9: Height variation of Ormocore for different exposure time for two design widths of 500 and 300 μm.

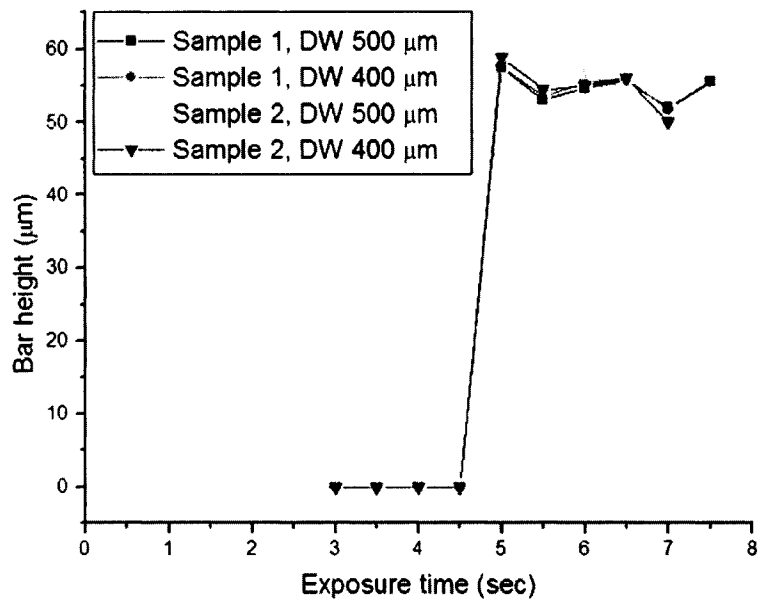

Figure 2.10: Height variation of SU-8 for different exposure time for two samples and two design widths (DW) of 500 and 400 μm.

magnified by the high absorption at those wavelengths. We assume the effect of noise can be neglected compared to the integrated intensity for the whole bandwidth of the spectrum.

2.3.3 Etch rate for different absorbed energy

After establishing a relationship between exposure time and the absorbed energy in the resist in Section 2.3.2, the variation of etch rate with absorbed fluence can be easily established. The absorbed energy density can be obtained by multiplying the x axes of Figure 2.9 and 2.10 representing exposure time with the absorbed intensity as reported in Section 2.3.2. The height information can also be converted to etch rate using

$$\text{Etch rate} = \frac{\text{Resist's initial thickness} - \text{Final height}}{\text{Developing time}} \tag{2.7}$$

As mentioned in the fabrication process (Section 2.2.2) the resist thicknesses for Ormocore and SU-8 are 35 and 55 μm, respectively.

So, with the height converted to etch rate and time converted to absorbed energy the desired etch rate dependency on absorbed energy are given in Figure 2.13 and 2.14 for Ormocore and SU-8, respectively. The dependency nicely matches a logarithmic behavior for Ormocore as shown in the Figure 2.13 with solid fitted lines. For SU-8 there is a rapid transition between no structure and structures with full heights when the exposure dose was increased to 3.8 J cm^{-3} from 3.4 J cm^{-3}. Given the thick resist (55 μm) used, undercutting is a possible reason for this steep transition. Reznikova et al [2] reported height variation with absorbed energy as shown in Figure 2.15. The resist thickness for the experiment was 12 μm and the structure formation started from $\approx$2 J cm^{-3} and full height was achieved for an exposure dose of $\approx$8 J cm^{-3}. The SU-8 used in their experiment was SU-8 5 from the MicroChem Corp. which is different from the SU-8 that we have used. The minimum exposure dose for structures with full height in our experiment was lower than that reported by Reznikova et al. The use of SU-8 2050, a product designed for better adhesion and other improved performances, may be the reason for the lower threshold value(see

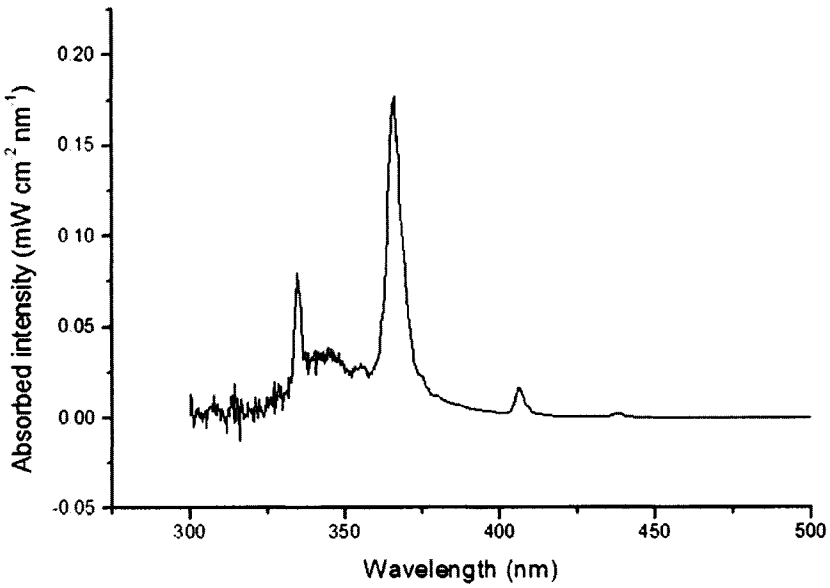

Figure 2.11: Absorbed spectral intensity versus wavelength for Ormocore.

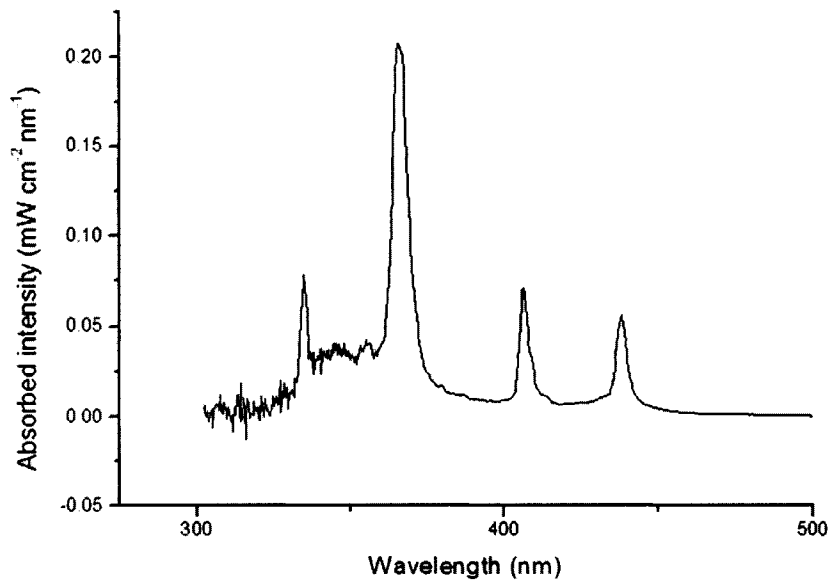

Figure 2.12: Absorbed spectral intensity versus wavelength for SU-8.

www. microchem.com for details). A modification to this experiment can be made by making a mask and coating the resist on the mask. Exposure in such an arrangement will result in structure formation starting from the surface of the mask. So, structures with heights smaller than the thickness will remain on the substrate. The problem was not as severe for Ormocore due to its low contrast and lower resist thickness.

The sensitivity and contrast (see Figure 1.2 in Section 1.1.3) for Ormocore were (54 $\pm$ 2) J/cm^{-3} and (15 $\pm$ 1) μm J^{-1} cm^3 per decade, respectively. On the other hand, The sensitivity for SU-8 was (3.8 $\pm$ 0.2) J/cm^{-3}.

2.4 Summary

The main objective of the single photon absorption experiment was to determine the behavior of the photoresists for different absorbed energy fluences. Absorbed energy contributes to bond breaking or bond forming of polymers based on their properties and chemicals used in the resists. For a negative photoresists, like those used in this experiment, more absorbed energy means stronger bond linking or more bonds among molecules. During the developing process, the developer washes away loosely bound or unbound molecules. Thus, molecules exposed to higher energy fluences are resistant against the developer, resulting in low etch rate.

Direct measurement of final height of test lines with different widths were utilized to determine the etch rate for different energy exposures. Energy variation was achieved simply by exposing the resists for different times. Detailed parameters such as transmittance, and absorption at operating wavelengths of the light source were considered to calculate the true absorbed energy.

The measured etch rate variation with absorbed energy for Ormocore followed expected logarithmic pattern. The sensitivity for Ormocore and SU-8 were (54 $\pm$ 2) J/cm^{-3} and (3.8 $\pm$ 0.2) J cm^{-3}, respectively. Moreover, the contrasts for the Ormocore was (15 $\pm$ 1) μm J^{-1} cm^3 per decade.

The height of structures in Ormocore rises gradually in a logarithmic manner. For, SU-8 the transition was very sharp. Structures with heights equal to the resist

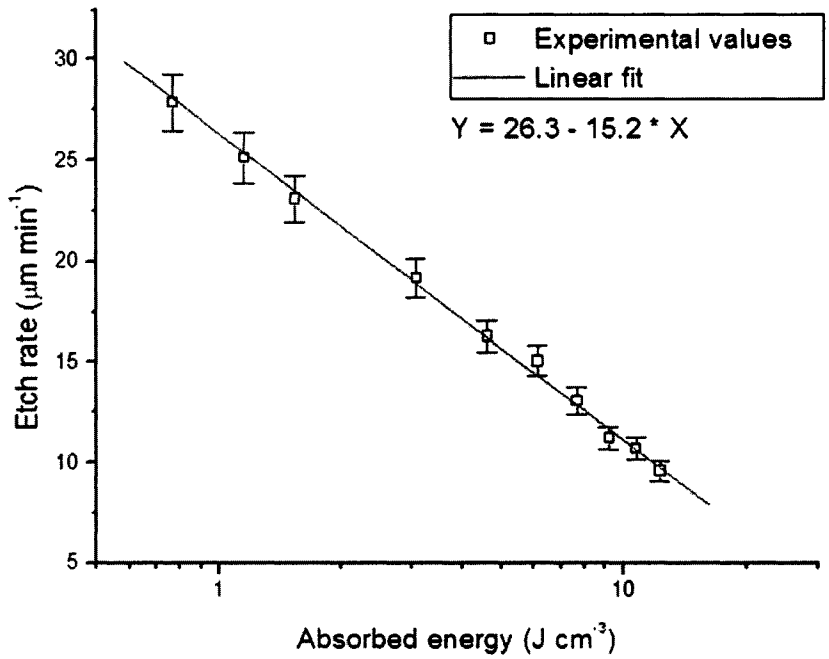

Figure 2.13: Etch rate variation with the absorbed fluence for Ormocore.

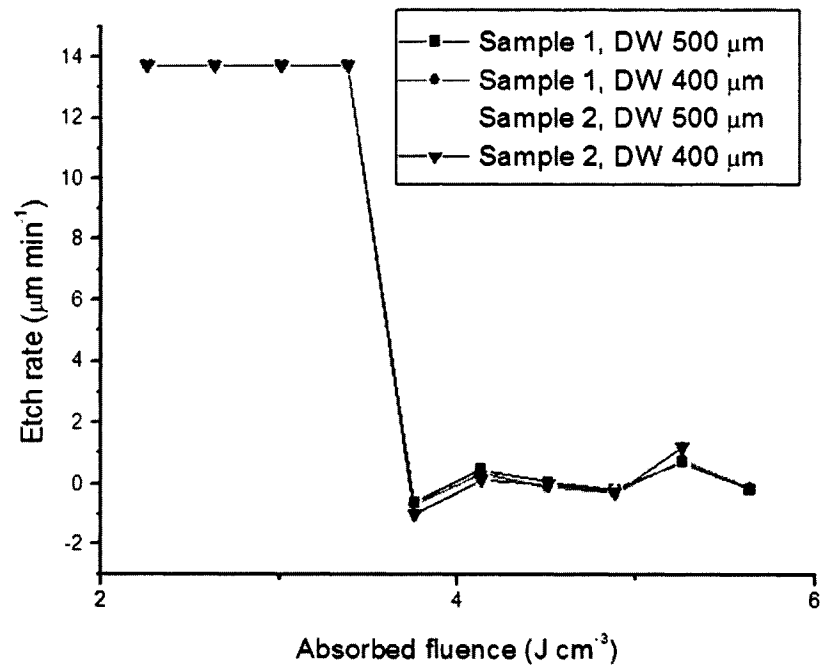

Figure 2.14: Etch rate variation with the absorbed energy for SU-8.

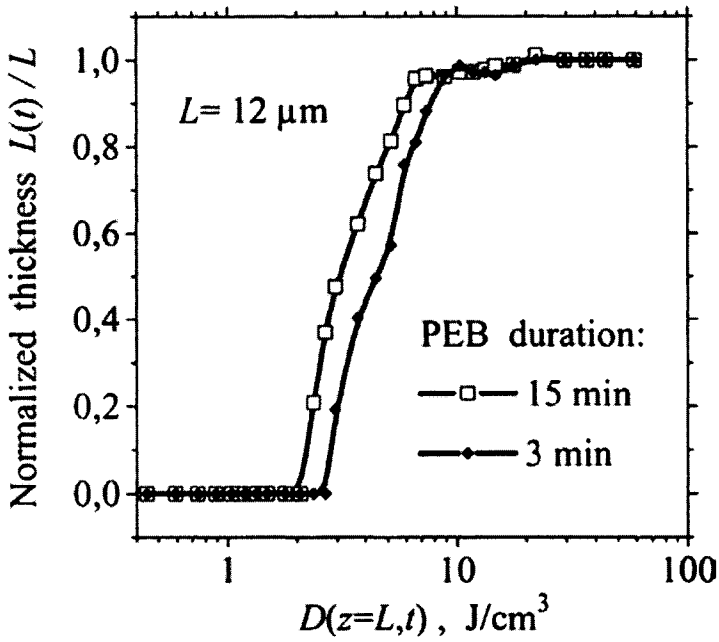

Figure 2.15: Thickness for different energy exposure for 12 μm thick SU-8 resist for two different post exposure baking (PEB) times [2].

thickness were observed for absorbed fluences above $\approx$3.8 J cm^{-3} while there was no structure remaining on the substrate for 3.4 J/cm^{-3} and below absorbed energy. These parameters will be an important factor to determine the structures written using TPA writing once the absorption due to the process is known.

Chapter 3

Two photon absorption experiments

Two photon absorption is a non-linear phenomenon that was first reported by Kaiser and Garrett [41], shortly after the first demonstration of a laser in 1960. Prior to the invention of the laser the response of a material in the electromagnetic field was normally found to be linear because of the small value of the applied field compared with the fields that naturally occur in atoms and molecules. For example, the electric field at the first Bohr orbit of a hydrogen atom is $E_0 \approx 5 \times 10^{11}$ V/m, which is large compared with the fields with which we ordinarily deal with in the laboratory. Fields of this magnitude can be achieved at the front face of a very fine needles. Nowadays electric fields of such a high magnitude are more commonly found near the focus of a very intense laser beams. Modern high power lasers, for example chirped-pulse amplifiers, produce pulses of light with a peak power of the order of 10^{13} W at a wavelength near 1 μm. Focused with an f/10 optical system to a spot 10 μm across, the beam has a peak intensity close to 0^{23} W/m^2. The electric field near the focus is on the order of 6×10^{12} V/m, which exceeds the electric field at the first Bohr orbit in a hydrogen atom by more than an order of magnitude. That is why nonlinear effects become important for an intense laser beam.

It was also possible to observe nonlinear effects by using a dc electric or magnetic field before development of lasers. In such cases the symmetry of an otherwise

isotropic substance such as a liquid or a cubic crystal is broken by applying the field. The optical activities induced in the medium due to this process can be observed and identified as a nonlinear process. For example, a strong electric field in a liquid such as nitrobenzene causes the molecules to be oriented preferentially in the direction of the electric field. The index of refraction of the material then becomes larger for parallel polarized light than for the perpendicularly polarized light. Light waves propagating through the liquid in this anisotropic state have their polarization altered in an observable fashion, as discovered by Kerr in 1876. In particular, light that is linearly polarized obliquely to the dc field is converted to elliptically polarized light, as the component of polarization parallel to the dc field is retarded relative to the component polarized perpendicular to the applied field. Clearly, Kerr effect is quadratic in the electric field, since the anistropy induced in the liquid depends on the direction but not the sign of the electric field. Similarly, a magnetic field can be used to break the symmetry of a liquid or solid medium and create what are called magneto-optical effects.

Nonlinearity due to very high intensity will be considered in this thesis. Pulsed lasers with femtosecond pulses will be tightly focused in to a sample to achieve a very high intensity. Energy absorbed due to nonlinear phenomenon by the material which is otherwise transparent to the light source will be utilized to change the chemical properties of the material. Finally selective transformation of material can be used to transfer different patterns into the material.

3.1 Theory to find the TPA coefficient

The photoresists used for TPA writing have negligible single photon absorption (SPA) for near infrared laser wavelengths. Thus the TPA coefficient basically determines how much energy is absorbed in the resist at a particular intensity. The behavior of the exposed photoresist with the developer also depends on the absorbed energy as shown in Chapter 2. For that reason, the TPA coefficient is an important parameter to predict the final structures produced in the photoresist.

3.1.1 TPA coefficient for a single layer material

Dragomir et al [42] and Chróinín et al [43] demonstrated a method to determine TPA coefficient of a bulk material and used the method to find the coefficients for different types of commercial fused silica and crystalline quartz. The basic theory proposed by those papers are utilized to determined TPA coefficients with modification, in some cases, for a two layer system.

The intensity distribution of a beam with spatial and temporal Gaussian profile with a beam waist ω at a particular location along its propagation can be described as

$$I_i(r,t) = I_{i_{max}} \exp\left[-2\left(\frac{r}{\omega}\right)^2\right] \exp\left[-\left(\frac{2t}{\tau_p}\right)^2\right], \tag{3.1}$$

where $I_{i_{max}}$ is the maximum on-axis intensity, τ_p is the pulse width at e^{-1} level. The FWHM pulse width τ is equal to $\tau_p\sqrt{ln2}$. Moreover, at $\omega/\sqrt{2}$ radius the intensity drops to e^{-1} level of the peak intensity at that particular time. Incident pulse energy, the integration of intensity over space and time can be expressed as,

$$E_i = \frac{\pi\sqrt{\pi}}{4} I_{i_{max}} \tau_p \omega^2 \tag{3.2}$$

Now let's consider the pulse is incident on a medium of thickness Δd and having a linear absorption coefficient, α, TPA coefficient , β, and refractive index, n. At low intensities and/or for a low value of β the transmittance, the ratio between transmitted and incident energy can be found to be,

$$T \equiv \frac{E_t}{E_i} = T_0\left[1 - \frac{\beta I_{i_{max}}(1-R)\{1-\exp(-\alpha\Delta d)\}}{2\sqrt{2}\alpha}\right] \tag{3.3}$$

where R is the reflectivity of the sample at normal incident and T_0 is the transmittance at zero-intensity. The reflectivity can be defined in term of refractive index of the material, n, and that of the surrounding material, n_0. T_0 can be defined in terms of the R, t and α as shown in the following equations,

$$R = \frac{(n-n_0)^2}{(n+n_0)^2} \tag{3.4}$$

$$T_0 = (1-R)^2 \exp(-\alpha\Delta d) \tag{3.5}$$

To measure the TPA coefficient the transmittance through the sample is measured for different intensities as mentioned in [42] and [43]. The TPA coefficient, β, can be easily calculated from the rate of change of transmittance with intensity, $\mathrm{d}T/\mathrm{d}I_0$, since,

$$\beta = \frac{2\sqrt{2}\alpha\left(\mathrm{d}T/\mathrm{d}I_{i_{max}}\right)}{(1-R)\left[1-\exp\left(-\alpha\Delta d\right)\right]T_0} \tag{3.6}$$

Moreover, for cases where $\alpha\ \Delta d << 1$ Equation 3.6 can be simplified as

$$\beta = \frac{2\sqrt{2}\left(\mathrm{d}T/\mathrm{d}I_{i_{max}}\right)}{\Delta d\,(1-R)\,T_0} \tag{3.7}$$

The slope should be calculated from the linear region of the transmittance change with peak intensity.

3.1.2 TPA coefficient for a double layer system

The photoresists used for TPA writing are coated on a Corning 0211 glass substrate. In order to get the coefficient of the resist from a double layer system the theory mentioned in Section 3.1.1 needs to be modified. During the experiment the substrate-resist layer were placed in such a way that the beam at first went through the resist then the transparent substrate. Refractive index and SPA coefficient of the substrate were experimentally determined using a monochromator (High Speed Monochromator System, HS-190, from J. A. Woollam Co., Inc) available at the Nanofab, U of A. TPA coefficient of the substrate was calculated using the method described for single layer system. All optical properties but TPA coefficients of the resists were collected from different sources and given in Appendix A.3. These parameters are essential to find the TPA coefficients as described in the rest of this section.

Let us consider a laser beam is going through two layers of different materials A and B as shown in Figure 3.1. Pulses with incident pulse energy, E_{i_A}, leave the system with transmitted energy, E_{t_B}. The ratio between E_{t_B} and E_{i_A} can be represented by Equation 3.3 as transmittance through B when one side is in material A and the other side is in air. The equation can be re-written to represent the case as,

$$T_{B_{A-B-0}} \equiv \frac{E_{t_B}}{E_{i_B}} = T_{0B_{A-B-0}}\left[1-\frac{\beta_B I_{iB_{max}}\left(1-R_{A-B}\right)\left\{1-\exp\left(-\alpha_B\Delta d_B\right)\right\}}{2\sqrt{2}\alpha_B}\right] \tag{3.8}$$

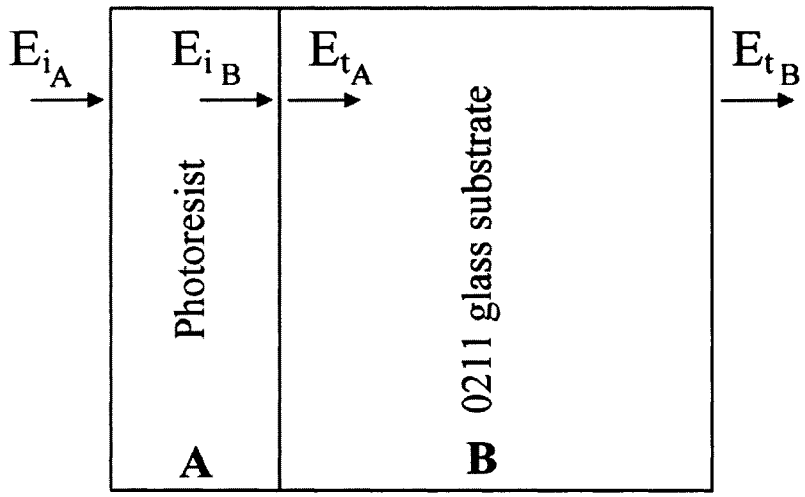

Figure 3.1: Geometric layout for TPA coefficient determination of a two-layer system.

where R_{A-B} is the reflection at the surface between A and B and $T_{0B_{A-B-0}}$ is the zero intensity transmittance for the arrangement. The parameters can be defined as,

$$R_{A-B} = (n_A - n_B)^2 / (n_A + n_B)^2 \tag{3.9}$$

$$T_{0B_{A-B-0}} = (1 - R_{A-B})(1 - R_{B-0}) \exp(-\alpha_B \Delta d_B) \tag{3.10}$$

$$\tag{3.11}$$

where, $R_{B-0} = (n_B - 1)^2 / (n_B + 1)^2$.

The incident intensity on B depends on incident energy E_{i_B}. Replacing $I_{iB_{max}}$ by $4E_{i_B}/(\pi\sqrt{\pi}\tau_p\omega^2)$ in Equation 3.8, E_{i_B} can be expressed in terms of a quadratic equation like $aE_{i_B}^2 + bE_{i_B} + c = 0$ where,

$$c = E_{t_B} \tag{3.12}$$

$$b = -T_{0_B}$$

$$a = \frac{4T_{0_B}\beta_B(1 - R_{A-B})[1 - \exp(-\alpha_B \Delta d_B)]}{2\pi\sqrt{2\pi}\tau_p\alpha_B w^2}$$

Solution of the quadratic equation can be used to find transmitted energy after A when it is sandwiched between air and B as $E_{t_A} = E_{i_B}(1 - R_{A-B})$. Once incident and transmitted energy of A is known the TPA coefficient can be found using similar method mentioned for a single layer material (Section 3.1.1). We have to keep in mind that in this case, the surrounding material is not only air.

3.2 Sample preparation

Samples for the TPA experiments were prepared in the same way as mentioned in Section 2.2.2.

3.3 Laser system and experimental setup

A 110 fs, 800 nm Ti:Sapphire laser amplifier (Spectra Physics Hurricane) was used in a single shot basis to determine the properties of the photoresists. The incident and transmitted pulse energy was measured using photodiodes calibrated with a Spectra Physics (Model 407 A) power meter. Maximum output power of the laser system was around 500 mW with a pulse repetition rate of 1 KHz. The experiment was performed in a single shot basis with pulse energies from 100 to 400 μJ.

The laser beam was focused with a 75 cm focal length lens manufactured by Newport. The specified focal length was for 589 nm light and with a $\pm 1\%$ tolerance. The sample was placed around (74.5 ± 0.1) cm away from the lens which is still 5.5 cm ahead of the true focal plane for 800 nm radiation (see 3.4.2). The sample was mounted on a 3D stage assembly made of three dc-motor stages. The sample was mounted vertically so that transmitted signal can be easily measured by the photodiodes. The stage had a resolution of 7 nm with a total span of 19 mm in x, y and z directions. The schematic diagram of the experimental setup for the TPA coefficient determination experiment is given in Figure 3.2. Mirrors M_1 and M_2 were used to align the beam. One photodiode (PD 1) measured the input beam energy before the lens. PD 2 measured the transmitted beam power after the sample when the beam was focused by a lens (L). PD 2 was placed around 9 cm away from the focal plane of the lens. Absorbing filters used during beam profiling were placed before the lens to reduce spatial distortion.

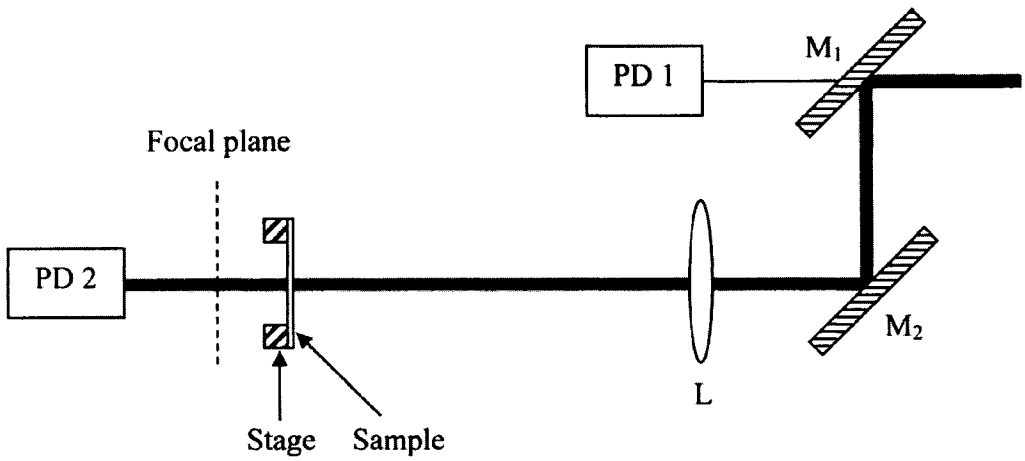

Figure 3.2: Experimental setup to determine the TPA of different photoresists.

3.4 Beam profiling of the laser beam

The beam waist is an important parameter to determine the TPA coefficients as the coefficient depends on the intensity. The intensity of a beam quadratically depends on the beam waist and the intensity is more for smaller beam-waist. A Cohu camera from Opticon Inc. and Spirikon software were used to capture and analyze the images of the beam after the lens. Sufficient filters were placed in the beam path to reduce the intensity of the beam in order to avoid damage of the camera. Knife edge experiments were also performed at the lens position and positions prior to the lens.

3.4.1 Before the lens (knife edge experiment)

Knife edge experiment is a well known technique to determine the beam waist. A sharp object was scanned along the beam so that it gradually revealed the beam and the transmitted power was recorded using photodiodes in a single shot basis. For a Gaussian beam with a beam waist ω the variation of transmitted power while scanning the beam in x direction can be fitted by

$$P(x) = P_0 \frac{\pi}{4\omega^2} \mathrm{erf}\left\{ \frac{\sqrt{2}\,(x - x0)}{\omega} + 1 \right\} \tag{3.13}$$

where P_0 is the power of the unblocked beam and x_0 is the center of the beam along x. Photodiodes were calibrated against Spectra Physics powermeter.

The very sharp edge of a knife was horizontally and vertically positioned and scanned to get the beam profiles along those axes at three different locations. Beam waists at these three locations were later used to predict the divergence of the beam, essential to predict the beam waist after the lens. The knife was moved with steps of 50 μm in the experiment. The step size was very small compared to the beam waist. Figure 3.3 to 3.8 show the photodiode voltages measured for different knife-positions and fitted curves to find the beam waists using Equation 3.13. The photodiode response fluctuates more at higher values as observed in these figures. The beam radii for different locations are tabulated in Table 3.1 and plotted in Figure 3.9. Linear fits to the beam radii variations give the divergence of the beam, θ_0.

The divergences for horizontal and vertical beam radii calculated were 0.16 and 0.15 mm/m, respectively. From the fitted curve the beam radius at the lens position should be 3.4 and 3.6 mm in the horizontal and vertical directions, respectively. The horizontal and vertical divergences obtained from the fits are slightly different indicating the presence of a very small astigmatism effect. The minimum beam waist, ω_0, before the lens can be calculated from the divergence values using,

$$\theta_0 = \frac{\pi\omega_0}{\lambda} \tag{3.14}$$

where λ is the wavelength and the position of the beam waist before the lens is given by,

$$z = z_0\sqrt{\frac{{w_z}^2}{w_0} - 1} \tag{3.15}$$

where, z_0 is the Rayleigh range of the beam defined as, $z_0 = \pi w_0^2/\lambda$.

3.4.2 After the lens (direct images)

The beam radius near the focus of the converging lens becomes much smaller and it can be determined more accurately and conveniently using a charge coupled device(CCD) camera. The pixel size of the CCD (Cohu C 6612D) used in the experiment is 9.9 μm. The area close to the focal spot, the scanning zone where the sample was placed during the experiment and halfway between lens and the focal spot are the three positions that were scanned for the thorough analysis of the beam. The camera

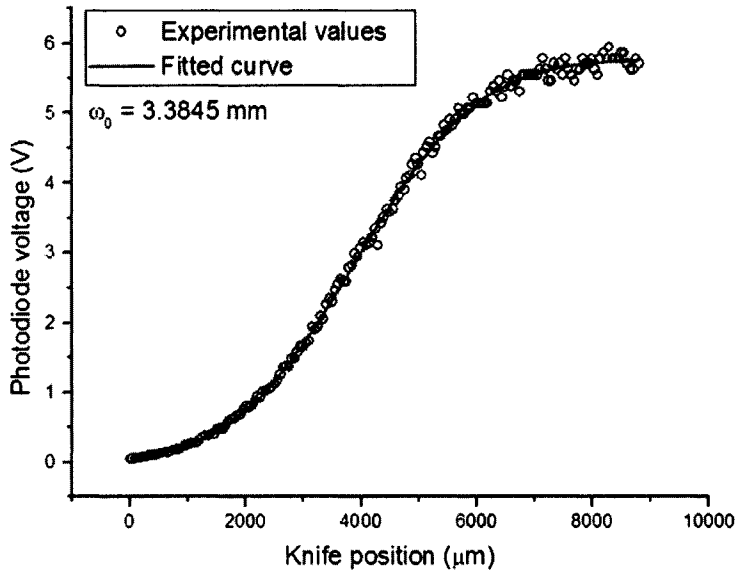

Figure 3.3: Knife edge experimental results to find horizontal beam radius at the lens position.

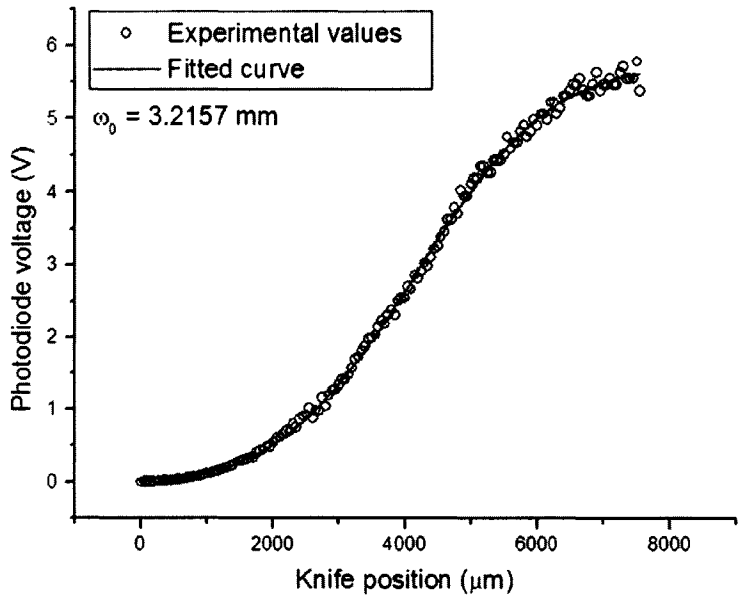

Figure 3.4: Knife edge experimental results to find horizontal beam radius at 1 m prior to the lens position.

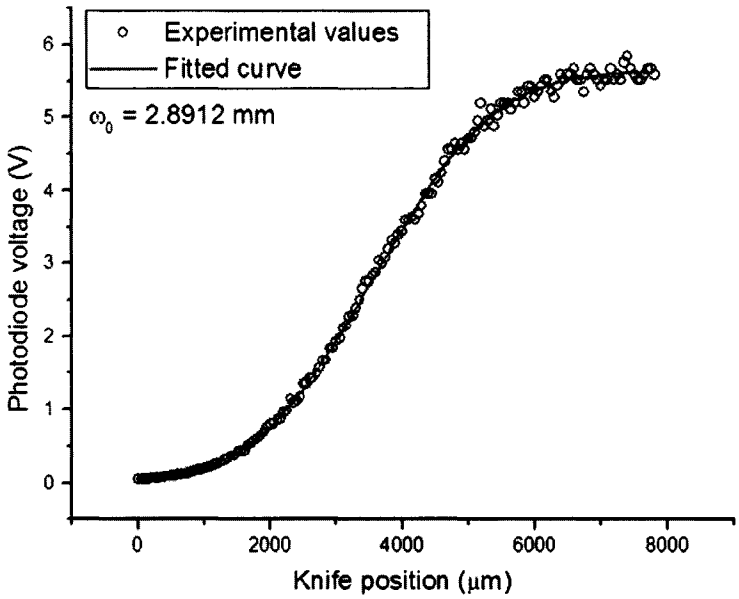

Figure 3.5: Knife edge experimental results to find horizontal beam radius at 3 m prior to the lens position.

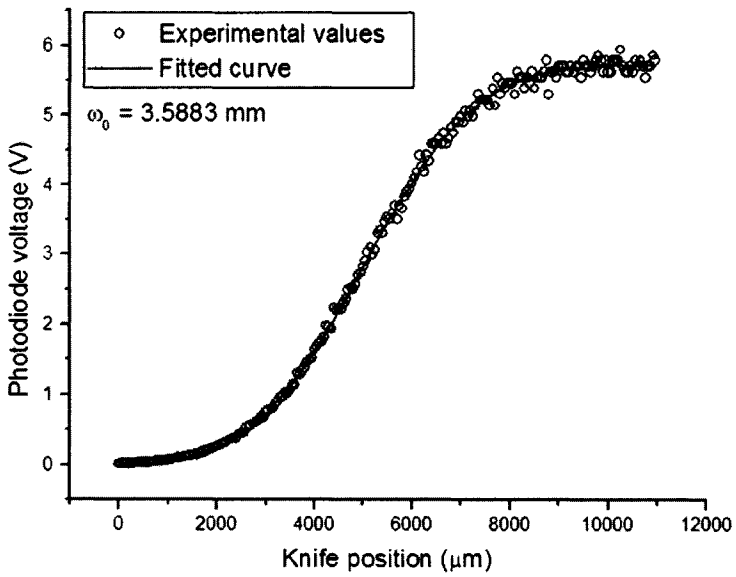

Figure 3.6: Knife edge experimental results to find vertical beam radius at the lens position.

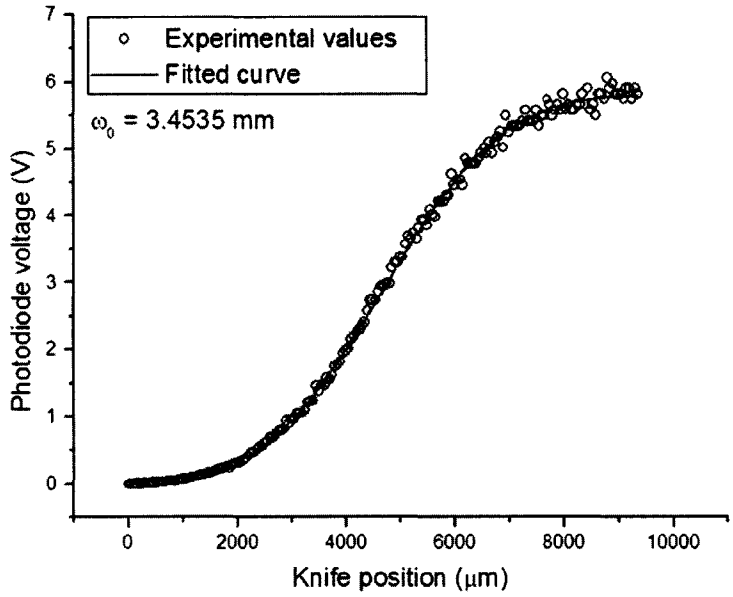

Figure 3.7: Knife edge experimental results to find vertical beam radius at 1 m prior to the lens position.

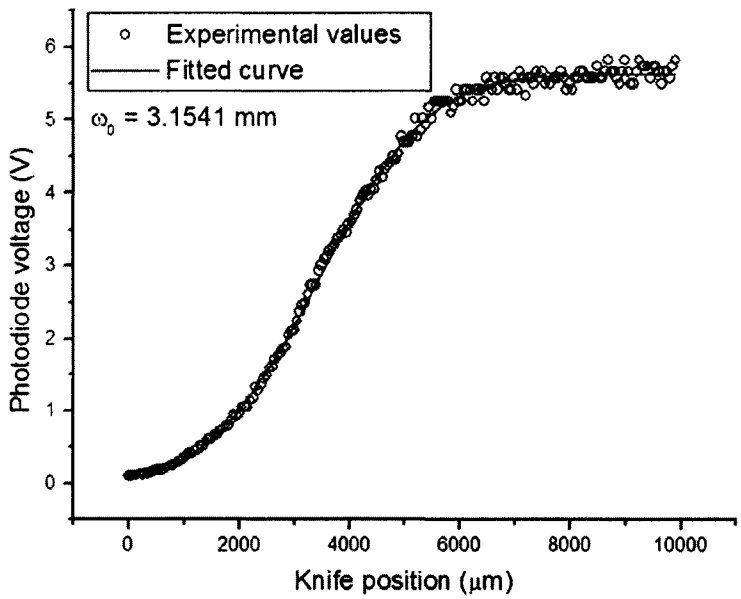

Figure 3.8: Knife edge experimental results to find vertical beam radius at 3 m prior to the lens position.

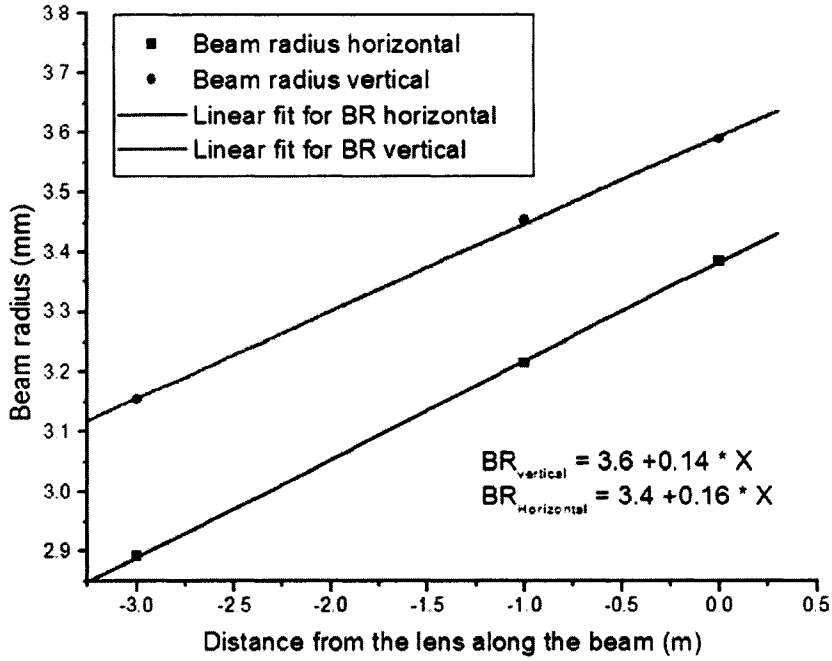

Figure 3.9: Beam radius variation along the beam path. The solid line is the linear fit to determine the divergence of the beam.

was set on a translation stage and the relative positions are recorded from the scale of that stage. Figure 3.10 shows the position of the CCD chip along the beam path when he translation stage is set at its zero position. The following subsections contain detailed analysis of the beam-profiling experiment in different regions. The image of the beam was captured in a single shot basis and the opening time of the aperture was adjusted so that it can capture the pulse triggered by the computer. In every spot, five shots were taken and then averaged to obtained the beam radius and other information. The vertical beam radii were measured and will be analyzed and compared to the theoretical values in the following sections. The variation of horizontal beam radii are given in Appendix A.5. The objective of this part of the experiment was to analyze the beam profile. Precision of the measurement was limited to some extent by the setup as the alignments such as tilt of the camera were not controlled with high accuracy. It is especially important for measurements at the focal region where the beam waist is very small ($\approx$50 μm). These limitations are negligible in the

Table 3.1: Variation of beam radii along the beam path before the lens

Position before the lens (m)	beam radius (mm)	
	Horizontal	vertical
0	3.3845	3.5883
1	3.2157	3.4535
3	2.8912	3.1541

scanning zone that we are really interested in as the beam radius is in the range of hundreds of microns.

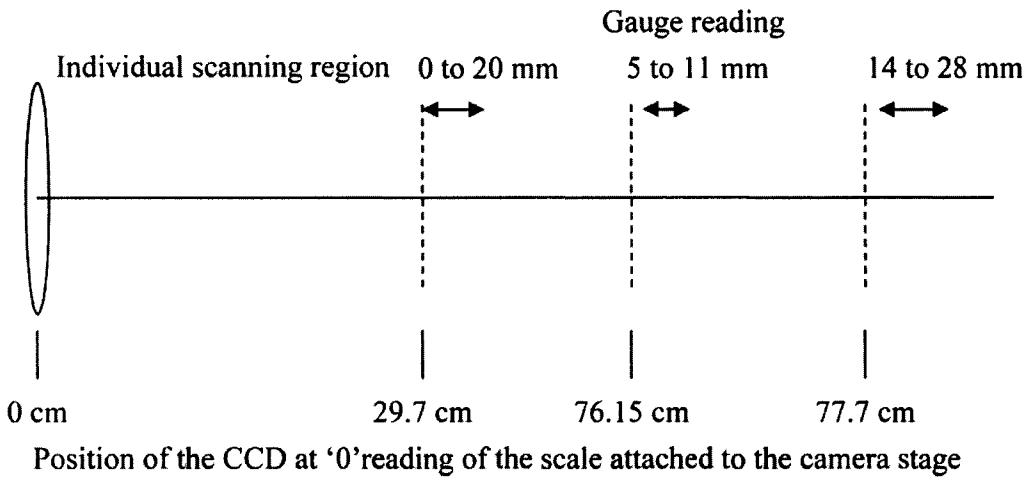

Figure 3.10: Positions of the different scanning zones along the beam path to find the beam profile.

Close to focal plane

Beam profiling of the focal region is important because it provides the information about the true focal length, beam waist at the focal point and M^2 parameter. As shown in Figure 3.10 the zero position of the scale was around (77.7 $\pm$ 2) mm away from the lens. Scanning was performed for the gauge position of 14 to 28 mm. The variation of beam radius along the beam is fitted to find the beam radiust at the

focus, ω_0 and the M^2 value using the following equation

$$d^2(z) = d_0^2\left[1 + \frac{16M^4\lambda^2}{\pi^2 d_0^4}z^2\right] \tag{3.16}$$

where $d(z)$ be the beam diameter which is twice the beam radius at position z. From the fitted curve, as shown in Figure 3.11, the beam diameter at the focus is 107.35 μm at a gauge position of 22.44 mm. The M^2 parameter extracted from the fitting is 0.97 ± 0.05. The minimum theoretical M^2 value is 1 for a Gaussian beam. Higher M^2 values mean that the beam diverges faster than a TEM_{00} Gaussian beam. Slightly different values may be due to small experimental errors. The true position of the focal spot can be determined by simply adding the gauge position that gives the minimum beam waist and distance of zero gauge position from the lens. The true focal position determined from the experiment is 79.9 cm.

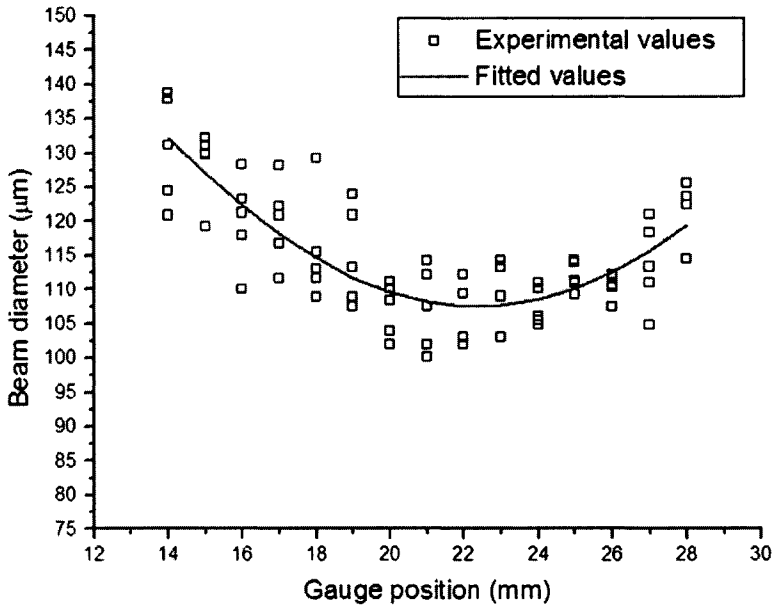

Figure 3.11: Beam diameter variation close to focus in the vertical direction.

The parameters defining the beam profile which are experimentally determined can also be calculated from the scan through the focal region at 77.7 cm and compared with the theoretical values. Appendix A.4 contains equations to calculate the parameters. Table 3.2 contains the experimental and theoretical values of beam waist

Table 3.2: Experimental and theoretical values of beam parameters after the lens

Parameter	Experimental values	Theoretical values for lens with	
		f = 75 cm	f = 77.5 cm
Slope(m/m)	-0.004865	-0.0047	-0.0045
Focal position(m)	0.799	0.7702	0.7966
beam waist(m)	5.37E-05	5.46E-05	5.65E-05
Rayleigh Range(cm)	-	1.17	1.25

at the focus, focal position, convergence and Rayleigh range of the beam after the lens. The experimental value of convergence is determined from the next section.

The experimental value for the position of the focal plane and the theoretical values for a 75 cm focal length lens are around 4% different than measured. The theoretical value of the focal position for a 77.5 cm focal length lens closely matches the experimentally obtaines value. This new value of focal length is valid if we consider the change in focal length due to operation at 800 nm compared to the specification at 589 nm and $\pm 1\%$ tolerance as specified by the manufacturer. But for the focal length of 77.5 cm the other parameters deviates $3-5\%$ more from the experimental values. We can conclude that most of the experimental values are close to the theoretical ones. The value of -0.0047 will be considered as the slope of beam waist change in the method to find the TPA coefficients.The experimentally measured values of divergence -0.004865 will give a calculated beam radius at the resist which is 0.8 μm larger than that for -0.0047 mm/mm divergence. The beam radius at the surface is around 200 μm as mentioned in a later section and thus this error is not very large.

Halfway between the lens and focal position

The face of the CCD camera was placed around 28 cm away from the lens and between the lens and the focal spot. The distance from the face of the camera to the CCD chip surface where the image was captured was 16.52 mm. That gave the true position of

imaging of around 29.7 cm. The gauge reading of the translation stage for the camera was set to 0 mm at this position. The scanning was performed from 0 to 20 mm of the gauge position. The gauge reading increased while going toward the focal spot. Figure 3.12 shows the variation of beam width, twice the beam radius, for different gauge position. The rate at which the beam waists changed with the position was -0.004865 m/m, as given in the figure. For a theoretical rate of change of beam radius of -0.0047 m/m the beam waist at zero gauge position should be around 2.2 mm ($3.5926 \times 10^{-3} - 0.0047 \times 29.6 \times 10^{-2}$ m). The experimental value of beam radius for the position was 2.34 mm.

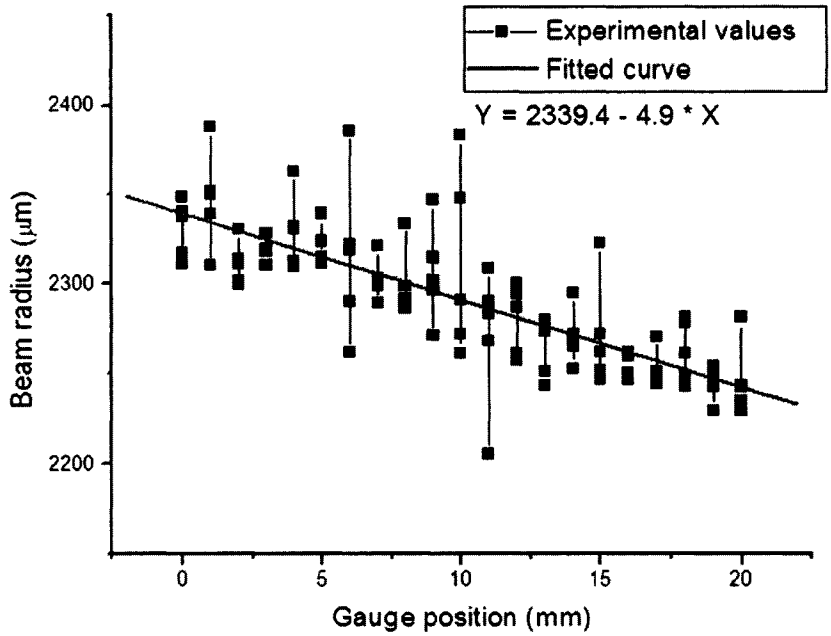

Figure 3.12: Beam radius variation at approximately halfway between the lens and the focal spot.

Scanning region

The plane that contained the front face of the camera at the starting of scanning region is around 74.5 cm away from the lens (CCD chip is $74.5 + 1.65 \approx 76.15$ cm away from the lens). As shown in Figure 3.10 the region of $6 - 11$ mm toward the focal spot from the starting was scanned to determine the TPA coefficient. The stage

to hold a square substrate 2 inches wide had a 1.5 inch opening so that the beam can pass through and transmitted beam power can be measured using a photodiode(PD 2). The face of the camera was placed against the surface that was used to mount the sample. At that position the gauge of the translation stage was 11.5 mm. As mentioned earlier the difference between the face of the camera and that of the CCD chip was 16.52 mm. That means the gauge position of -5.56 ($= 11.5 - 16.52 - 0.54$) mm captures the beam profile at the top surface of the the 540 μm glass surface. The body of the camera is too big to get through the openning of the stage when scanning for lower values of the gauge scale. So, the scanning was performed for 6 to 11 mm of the gauge scale and beam waist at -5.56 mm gauge reading was extrapolated from the trend.

Figure 3.13 and 3.14 shows the variation of beam radius in the scanning zone for different gauge scale reading. The rate of change of beam radius along the vertical direction for the scanning region is -0.004722 which is very close to the values of the slope tabulated in the Table 3.2 for the vertical direction. If we extrapolate the equations given in these figures the beam radius at the surface of the sample (X = -5.56) will be 237.2 μm and 203.4 μm in the vertical and horizontal direction, respectively. These values of beam waist will be used to find the TPA coefficients. Appendix A.7 contains the image of a typical beam profile at this region.

Beam diameters for different positions after the lens, i.e. at different regions, as mentioned in the previous sections, are given in Figure 3.15. For this fit the values for the M^2 parameter, the minimum beam diameter, the distance of the focal plane from the lens and slope of the beam radius variation are 0.96, 104 μm, 79.5 mm and -0.0047 m/m, respectively.

3.5 Results

Glass substrates coated with photoresists were mounted vertically on the sample holder. Different incident power on the sample and corresponding transmitted power through it were measured using the calibrated photodiodes. Every time a new spot

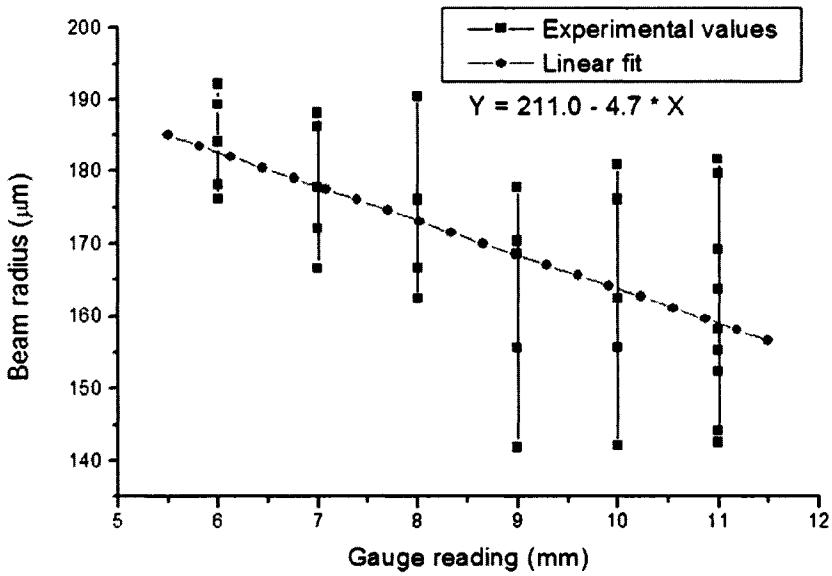

Figure 3.13: Beam radius (vertical) variation close to the scanning zone.

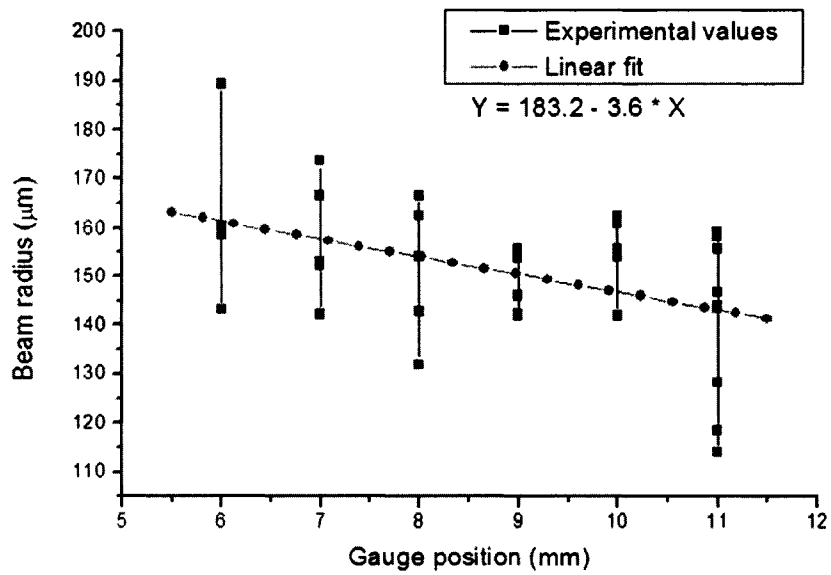

Figure 3.14: Beam radius (horizontal) variation close to the scanning zone.

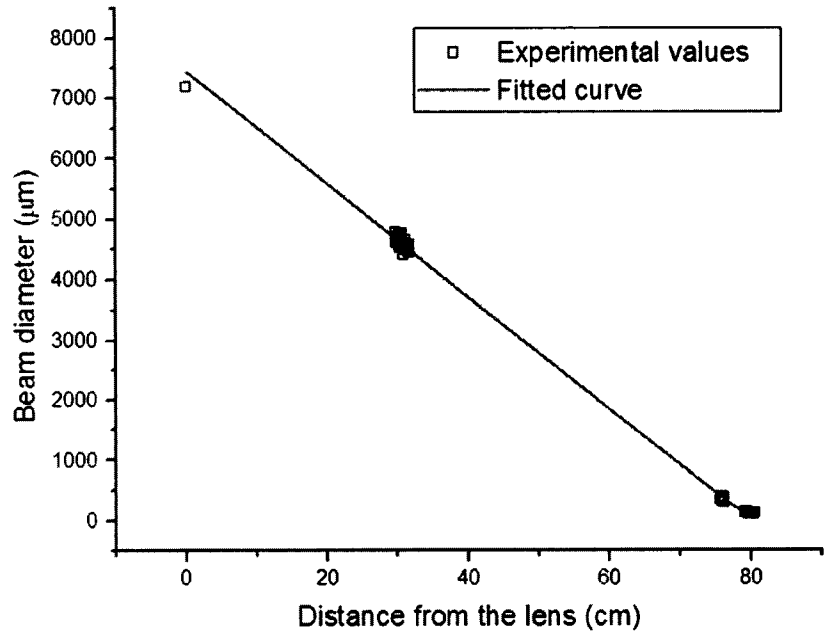

Figure 3.15: Beam diameter (vertical) at different positions after the lens.

was chosen to avoid incubation effects. For a given sample three sets of readings were taken and there were three samples to find parameters of a material. It is evident that there are different material properties we need to know to accurately determine the TPA coefficients as described in Section 3.1.

3.5.1 Experimentally determined parameters

The pulse width of the laser was measured using a Positive Light Autocorrelator (Model SSA) in a single shot basis. The gratings in the laser system were adjusted to produce minimum pulse width prior to the experiment. Figure 3.16 shows the pulse profiles of ten pulses recorded on the oscilloscope output of the autocorrelator trace. Pulse width in FWHM can be determined from the FWHM of the trace after scaling the FWHM of the trace with a factor of 0.30052 fs/μs assuming a Gaussian temporal profile. Variation in the FWHM of these pulses is plotted in Figure 3.17 for these ten cases. Matlab codes were used to filter out noises of the pulse profiles using a third order Butterworth digital low pass filter with cut-off frequency, $\omega_n = 0.15$ and to calculate the FWHM of the pulses. The average pulse width was (111 ± 3) fs.

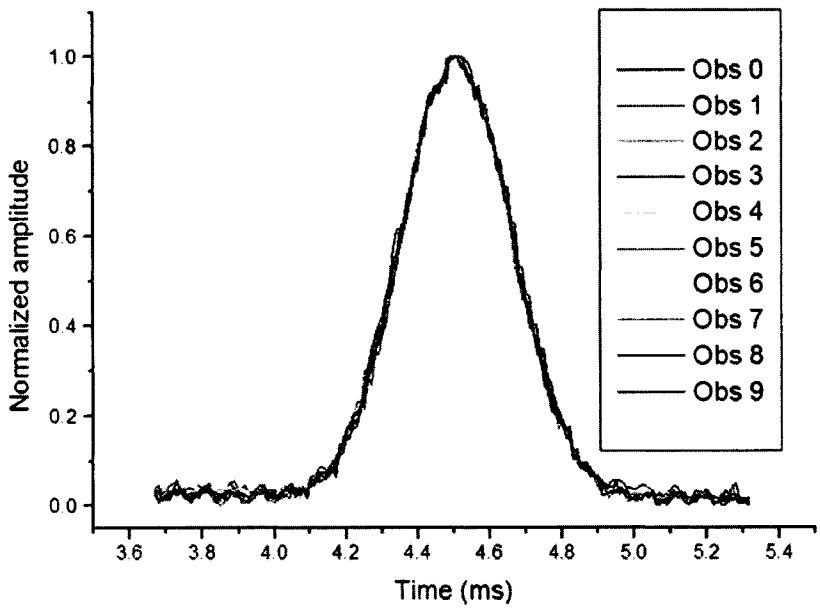

Figure 3.16: Normalized autocorrelation traces for ten observations versus oscilloscope sweep time.

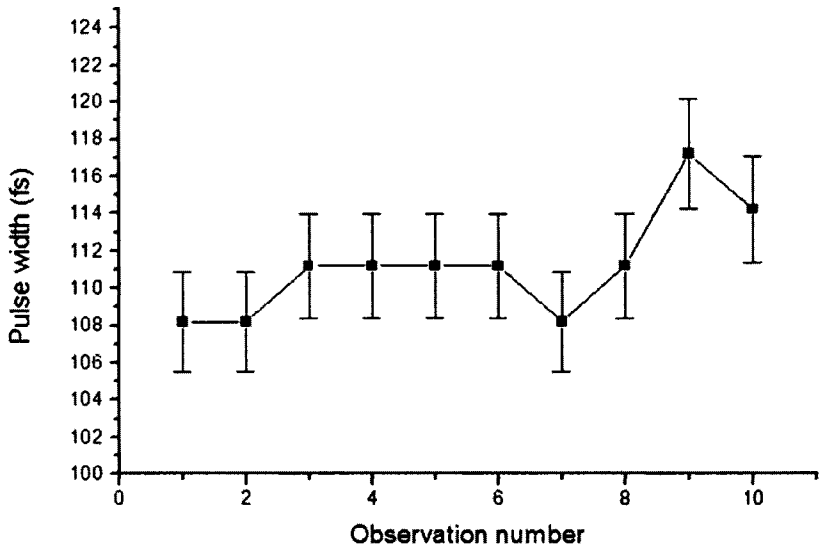

Figure 3.17: Measured pulse width for different observations.

The beam power for laser pulses at 1 KHz repetition rate was measured using a Spectra Physics power meter (Model 407 A). Afterwards, output of the photodiodes were captured on an oscilloscope for singe shots. Peak values of the signals recorded to the computer were calibrated with the power meter readings. The Photodiode output versus power are plotted in Figure 3.18. The linear equation to fit PD 1 calibration is Y = 488 X - 3.7 while the equation for PD 2 is Y = 88.4 X + 5.8. The photodiode voltages were multiplied by 10 in the figure. The offset from the origin could have been avoided by taing some more readings close to the origin. The value of the offset is negligible for the higher pulse energies used for TPA resist exposures.

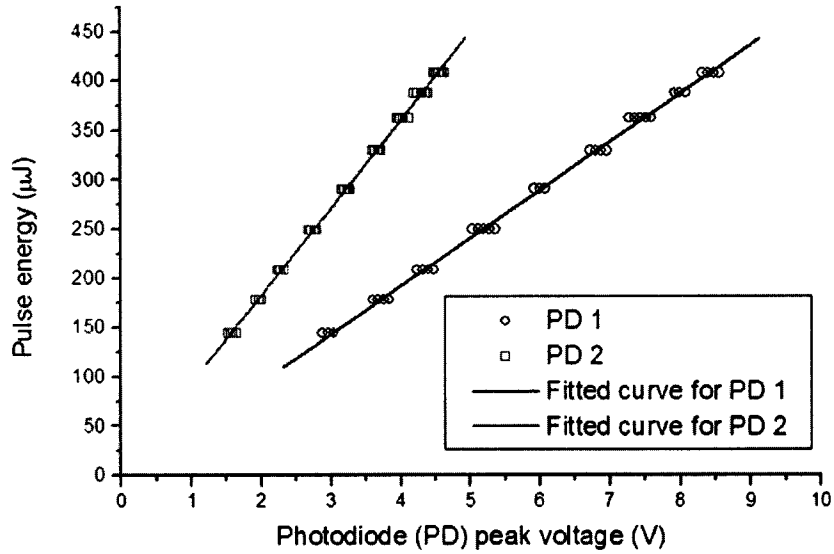

Figure 3.18: Photodiode calibration to measure the pulse energy.

3.5.2 Other optical properties

Material properties like refractive index and linear/single photon absorption coefficients also play a vital role in determining the TPA coefficient. Other than 0211 glass substrate most of the values representing essential optical properties are collected from different literature [4, 5, 6] or manufacturer's websites or manuals [3]. Refractive index and absorption coefficient of 0211 glass were determined using a Monochromator in the University of Alberta Nanofab. Appendix A.3 contains dif-

ferent parameters of different materials over a wide wavelength spectrum. Table 3.3 shows the values of important parameters used to determine TPA coefficients of the 0211 glass and resists.

Table 3.3: Essential optical properties of the materials and source of these information

Property	Material	Value	Source
Refractive index at $\lambda = 800$ nm	Ormocore	1.5482	[3]
	SU-8	1.5906	[5]
	0211 glass	1.51	see A.3.6
Linear absorption coefficient (m^{-1}) at $\lambda = 800$ nm	Ormocore	0.557	[4]
	SU-8	2.09	[6]
	0211 glass	3.80×10^{-04}	see A.3.6
Thickness (μm)	Ormocore	35	[3]
	SU-8	55	[3]
	0211 glass	540	measured

3.5.3 TPA coefficients

Input and transmitted pulse energy were recorded to calculated the incident peak intensity as well as transmission through the sample. For 0211 glass substrate the calculation was relatively easy and the TPA coefficient was calculated from the variation of transmission with intensity. This coefficient of beta was used for the samples where the resists were coated on the glass substrate. The TPA threshold for SU-8, as reported by Witzgall et al [24] is also in that order. Figure 3.19, 3.20 and 3.21 show the variations of transmission for 0211 glass, Ormocore and SU-8 layers, respectively. These figures contain data for one sample. TPA coefficients determined from these graphs and for other samples are tabulated in Table 3.4.

TPA coefficients drastically reduces with wavelength. Fused silica has a TPA coefficient of 0.75 cm GW^{-1} [44] for 212.8 nm wavelength. For 354.7 nm light it reduces

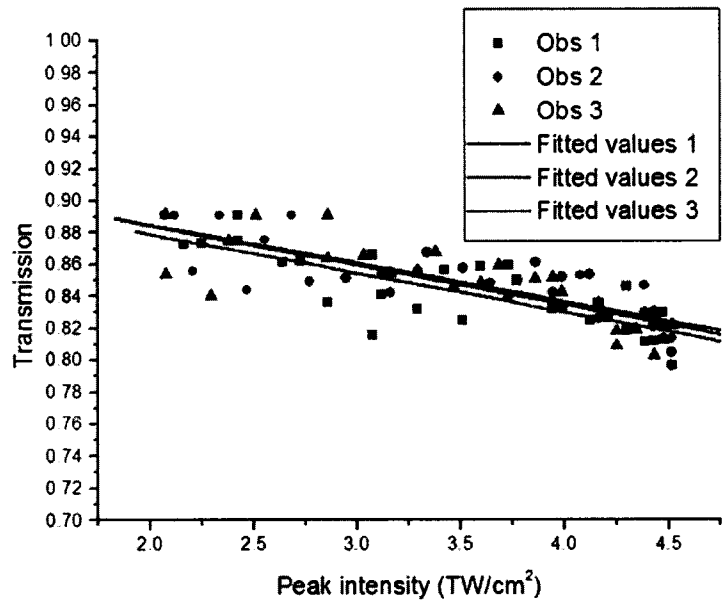

Figure 3.19: Variation of transmission for 0211 glass substrate with peak intensity. The TPA coefficient is determined using the slope along with other parameters.

to 0.00125 cm GW^{-1} or 1.25 cm TW^{-1} [45]. TPA coefficients of the material for other wavelengths are summarized in Appendix A.6. The measured TPA coefficient of 0211 glass at 800 nm is (1.42 ± 0.2) cm TW^{-1} which is comparable with the values for Fused silica in the near UV range. The coefficients measured for Ormocore and SU-8 are (33 ± 6) cm TW^{-1} and (28 ± 5) cm TW^{-1}, respectively. Ormocore is a viscous liquid and it moved very slowly when it was set vertically on the sample holder. This effect causes slight changes in the resist thickness over time and is a potential reason for the relatively high deviation of the value. A second set of measurements was carried out to reduce the effect. This was done by doing the experiment more quickly and flipping the sample vertically after each observation. Table 3.5 shows the values of the TPA coefficient for different samples and observations. The beam profile this time was determined directly from the CCD camera. To do this, the stage was moved 12 cm from the desired scanning surface (11.5 mm for the camera face to CCD chip distance and 0.5 mm for the substrate thickness) toward the lens. Then the face of the CCD was aligned with the surface of the sample holder and beam

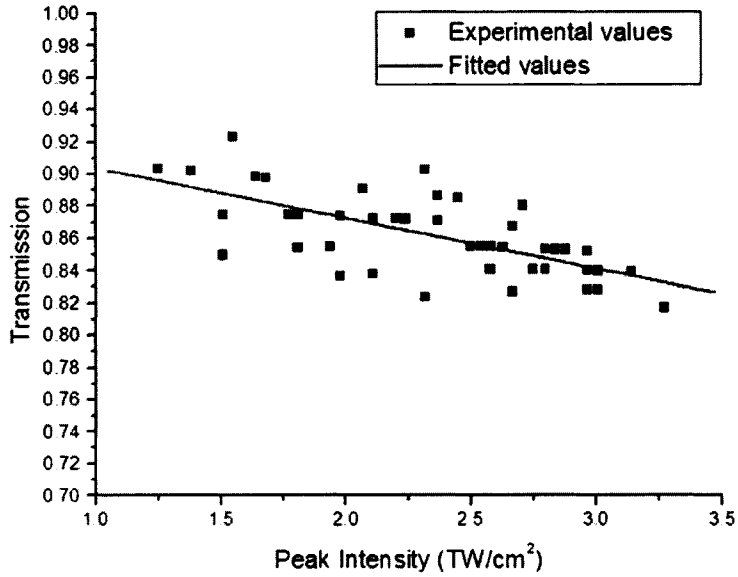

Figure 3.20: Variation of transmission for Ormocore layer when coated on 0211 glass substrate. The data points are for three observations of a sample.

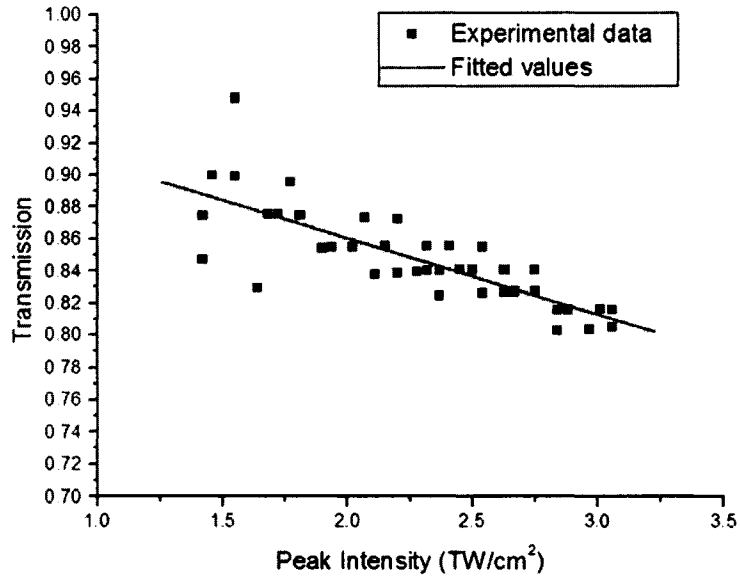

Figure 3.21: Variation of transmission for SU-8 layer when coated on 0211 glass substrate. The data points are for three observations of a sample.

measurement was done. The stage was moved again 12 cm toward the lens which is the plane that the CCD was used to image the beam. It should be mentioned that one of the elements joined to the face of the camera was removed and this reduced the camera face to CCD chip distance to 11.5 mm from 16.5 mm. The beam radii for this experiment were 174 μm and 120 μm in vertical and horizontal direction, respectively. Figure 3.22 shows the beam profile captured at this surface.

TPA coefficients obtained from the second attempt have much less standard deviation. The weighted average of these value will be considered to be the best experimental value. Thus the experimental value for ormocore is found to be (29.8 $\pm$ 1.5) cm TW^{-1}. Considering errors in measuring energy, spot size, pulsewidth and other parameters the overall error of β is $\pm$ 20 %. So, the TPA coefficients for Ormocore and SU-8 are (30 $\pm$ 6) cm TW^{-1} and (28 $\pm$ 6) cm TW^{-1}, respectively.

3.6 Summary

Two photon absorption coefficients of two widely used and commercially available photoresists used for TPA writing were investigated in this chapter. Well established method to determine the coefficients with slight modification were utilized to extract the parameter out of experimental transmission data. Detailed analysis of experimental parameters were also discussed in this chapter which was important for precise calculation of the values. Some material properties were also measured using different devices and methods.

The average TPA coefficients for Ormocore and SU-8 measured for three samples of each resist coated on glass are (30 $\pm$ 5) cm TW^{-1} and (28 $\pm$ 5) cm TW^{-1}, respectively. The coefficient measured for 0211 glass substrate was (1.4 $\pm$ 0.2) cm TW^{-1} . The value is comparable to similar materials, such as fused silica. TPA coefficients will be an important parameter to determine absorbed power in the material due to TPA process and subsequently predict the behavior of exposed resist during material processing.

Table 3.4: TPA coefficients for different samples of 0211 glass substrate and Ormocore and SU-8 resists.

Material	Sample number	β (cm TW^{-1}) for the				
		observations			sample	overall
0211 glass	1	1.46	1.44	1.48	1.46	1.4 ± 0.04
	2	1.34	1.32	1.39	1.35	
	3	1.26	1.50	1.60	1.45	
Ormocore	1	27.56	26.06	27.90	27.17	32.5 ± 2.9
	2	45.52	25.99	41.58	37.70	
	3	35.35	23.28	39.37	32.67	
SU-8	1	27.19	26.88	27.03	27.03	27.9 ± 1.1
	2	29.56	32.38	24.99	28.98	
	3	22.32	29.59	30.89	27.60	

Table 3.5: TPA coefficients for Ormocore (second attempt)

Material	Sample number	β (cm TW^{-1}) for the				
		observations			sample	overall
Ormocore	1	26.95	26.845	25.985	26.59	27.1 ± 0.3
	2	26.175	27.11	28.56	27.28	
	3	27.418	26.32	28.15	27.29	

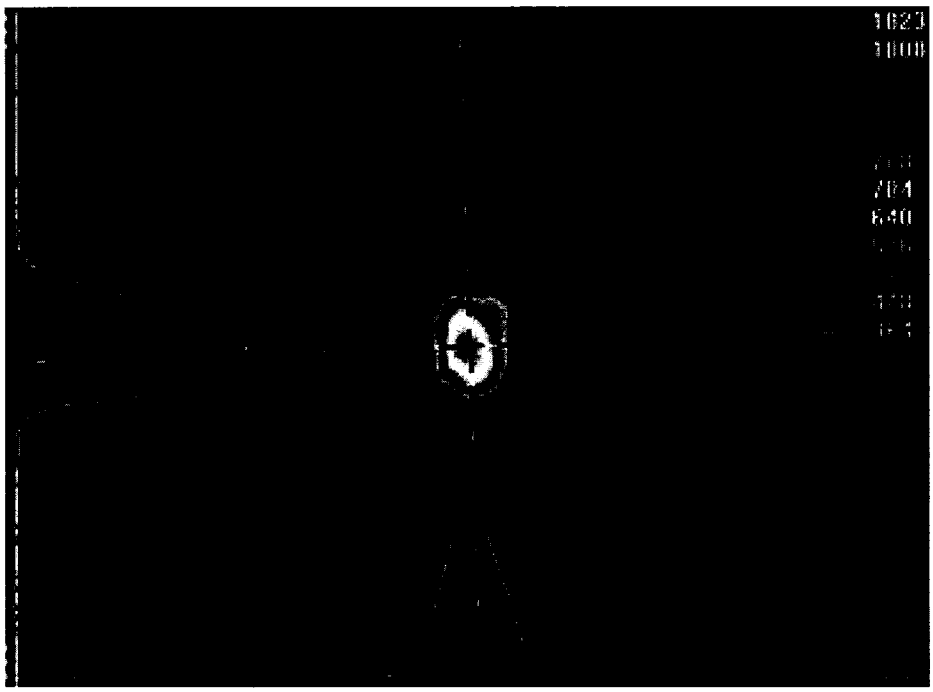

Figure 3.22: Beam profile at the position of the surface of the resist.

Chapter 4

3D structure-writing using TPA process

In a two photon absorption process the absorption is proportional to the square of the intensity. That is why for pulsed laser writing reducing the power to half requires four times the number of pulses to cause the same photophysical or photochemical change within the same volume. Moreover, the number of molecular bonds affected per pulse decreased rapidly for low pulse energy. This gives higher resolution and more control over precision writing as variations in the final structure due to variations over a few number of pulses is negligible. For these reasons, high repetition rate pulsed lasers are widely used for high resolution TPA writing.

Most of the research groups have used Ti:Sapphire laser oscillators for 3D writing to date. The average parameters for such laser oscillator systems are 80 MHz repetition rate, 100 fs pulse width, 800 nm wavelength. Exposing resists to very high power may cause damage in the resists. TPA writing in Ormocore and SU-8 has been demonstrated for powers within the range of 10 to 50 mW. The highest resolution recorded for Ormocore was for a 100x oil immersion objective with 1.4 numerical aperture (NA) value [20, 23, 27]. High aspect ratio structures in SU-8 were reported for 10x and 60x objective with NA values of 0.30 [26] and 0.85 [25], respectively. The best resolution reported for TPA writing was 120 nm using SCR 500 resin [20]. For commercially available resists Ormocore [23] and SU-8 [27] the minimum dimensions

written by TPA method were 150 and 475 nm, respectively.

Ormocore has mostly been used for high precision writing of complex structures. The average aspect ratio for structures produced in Ormocore using a 100x 1.4 NA objective is around 5:1 as reported by Serbin et al [23]. On the other hand, SU-8, a widely used resist for X-ray lithography, was explored for high aspect ratio structures. Teh et al [26] reported an aspect ratio upto 23:1 for vertical photoplastic planes and 50:1 for photoplastic pillars.

The structures reported in this chapter are also written by 800 nm Ti:Sapphire laser with typical laser parameters close to that mentioned above. Different structures were produced in both SU-8 and Ormocore to demonstrate the 3D writing capability. Moreover, simple lines and dots at different powers were produced to characterize the 3D writing process.

4.1 Experimental details

An 80 fs, 800 nm Ti:Sapphire laser oscillator (MaiTai, Spectra Physics) and a 40X objective with 0.65 NA was used was for writing of submicron resolution 3D structures. Figure 4.1 shows the setup utilized for 3D structure writing using the TPA method. Exposure time was controlled by a Newport electronic shutter having a minimum shutter openning time of 10 ms. A 3-axis computer controlled dc motor stage from Physik Instrument (PI) with a minimum resolution of 7 nm was used to control the sample position. The unidirectional repeatablity and backlash of the stage were 0.1 μm and 2 μm, respectively. Codes written in Labview 5.1 were used to write structures at different positions and at different powers with different control parameters. The half wave plate used in the setup to control the power of the beam was automatically changed for 3D structure writing. For characterization of lines and dots the power was set manually for better precision. The transmittance of the objective was measured to be 0.70 and power given in this chapter is the power after the objective considering this transmittance.

The fabrication process for the resists was similar to that mentioned in Section

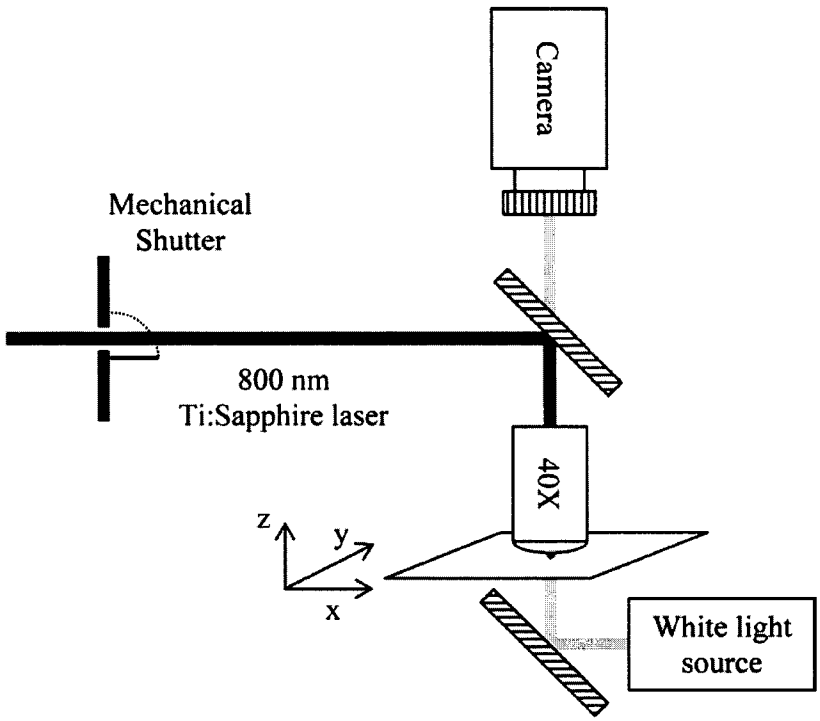

Figure 4.1: Setup for 3D structure writing using TPA process.

2.2.2 for the single photon absorption studies. The thickness of the Ormocore was 20 μm for TPA writing instead of 35 μm as stated in the earlier chapter. Ormocore was coated at 3000 rpm for 30 seconds in order to get this thickness. The ramp to reach this velocity from 500 rpm was 9 seconds. Settings for the initial two speeds were idential to the Section 2.2.2. There was no change in baking or development procedures for Ormocore compared to that given in Section 2.2.2. Processing of SU-8 for TPA writing was similar to that of the TPA experiment. Again a 50 μm thick SU-8 layer on glass was used for TPA writing.

4.2 3D structures

The TPA process allows change of the material properties due to light absorption within a small volume around the focal spot. This small modified region is called a volume pixel or voxel. We can neglect the change in the distribution of the intensity as a very small fraction of the energy is absorbed while propagating through focus,

one generally obtains ellipsoidal shaped structures if one writes with intensities more than a threshold value for a focused Gaussian beam. For a high NA objective the beam is focused to a smaller beam radius as well as it has smaller depth of focus compared to that with low NA objective. The ratio between longitudinal to lateral size of the voxel increases with decrease of the NA values.

The effective focal length of the 40X objective with NA 0.65 used in the experiment was 470 μm. When the aperture is filled with the beam the ratio between the depth of focus to the beam waist at the focal spot is much more than unity. When the beam is perpendicular to the substrate and an objective with low NA is used to focus the beam in the material coated on the substrate, the structure produced in the material will be like a post standing on the substrate with high aspect ratio. It basically limits the true 3D writing when a voxel is required to be more like a dot or sphere.

4.2.1 Designed structure

Considering the limitations of using a 40X objective several structures were designed to be implemented in the TPA absorption writing. The first of the designed structures are shown in Figure 4.2 and 4.3. The figure also shows the scanning scheme to produce such a structure. The final height of the structure is dependent on the vertical position of the sample, scanning speed and the power of the laser beam.

The base of the square spiral is a 10 μm wide. The height increases 2.5 μm from the starting point of one side of the wall to the end of it while scanning. The length of the arm to complete the square was scanned only for 7.5 μm. A floating vertical plane structure was also designed to demonstrate the feasibility of a floating structure. It is also a test to find the strength of the resist and show the stability of writing in a solid resist.

All the structures were written at different focal positions and at different scanning speeds. For a particular scanning speed the velocity components along different axes were distributed based on the distances to travel to the next end point. Then the movement for different axes was initiated at the set velocity so that they end up at the same time. The shutter was opened at the beginning of structure writing and closed

when one unit structure was completely written. The code waited for the end of that scan and as soon as it is over a translation from that position toward a new position was executed. The time duration of scanning between two points is small for high scanning speed and for small distance to travel. Thus the transition time from one line scan to another became comparable to the time required to draw a line. Moreover, the acceleration was set to the default value of 3500 μm s^{-2}. Acceleration time also became significant while drawing small structures at high scanning speed. That made the edge heights and widths non-uniform for different structures. There was also hysteresis in the motion of the stages that affected the writing of fine structures using the set-up. The performance of the stage is given in Appendix A.8.

4.2.2 SEM images of 3D structures

Scanning electron microscopy (SEM) is a good tool to give 3D images of different microstructures. The SEM available in the Earth and Atmospheric Sciences department at the University of Alberta was used to take images of structures produced in the resists. Figures 4.4 to 4.7 show the SEM images of different 3D structures produced in the resists. Projected square spirals and vertical planes were made for different powers and different scanning speeds. A beam power of 20 mW at 75 μm s^{-1} scanning speed has produced the best 3D structures. Lower power and/or higher scanning speed made the structures too weak. On the other hand, higher power and/or lower scanning speed produced long and wide voxels. As described in the previous section there are significant distortions due to the physical limitations of the scanning capability of the positioning stage assembly. Specially for the 'floating plane' writing when the stage changed directions to go down it also shifted in y axis. This shift was consistent for writing in both of the resists and it was evident in all the structures drawn at different heights. The hysteresis for the mechanical stage used in the experiment is around 2 μm (Appendix A.8). The stage can replicate the true scanning scheme when the dimensions of the structures were large and/or the scanning speed was very slow and also in one direction. SU-8 is a hard or solid resist during the exposure process and has produced more stable structures (Figure 4.7).

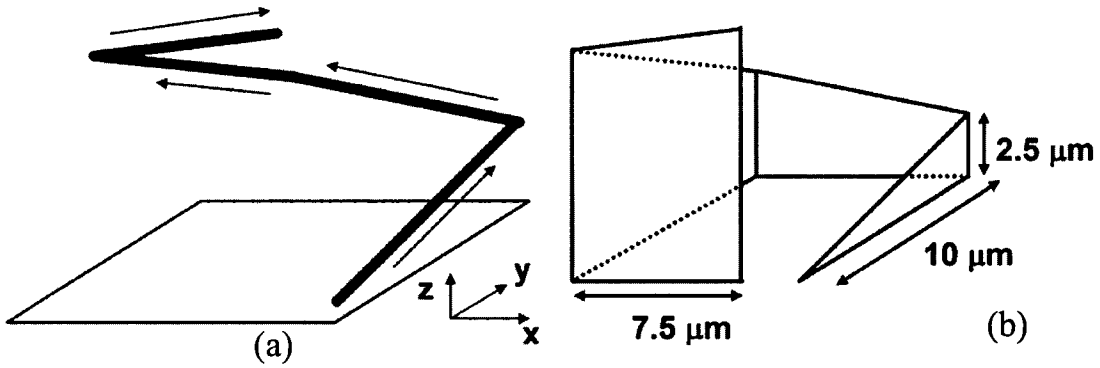

Figure 4.2: (a) Scanning sequence of and (b) schematic structure for a projection of a square spiral shaped structure. The height of the structure is dependent on the scanning speed, beam power and vertical position of the focal point above the substrate.

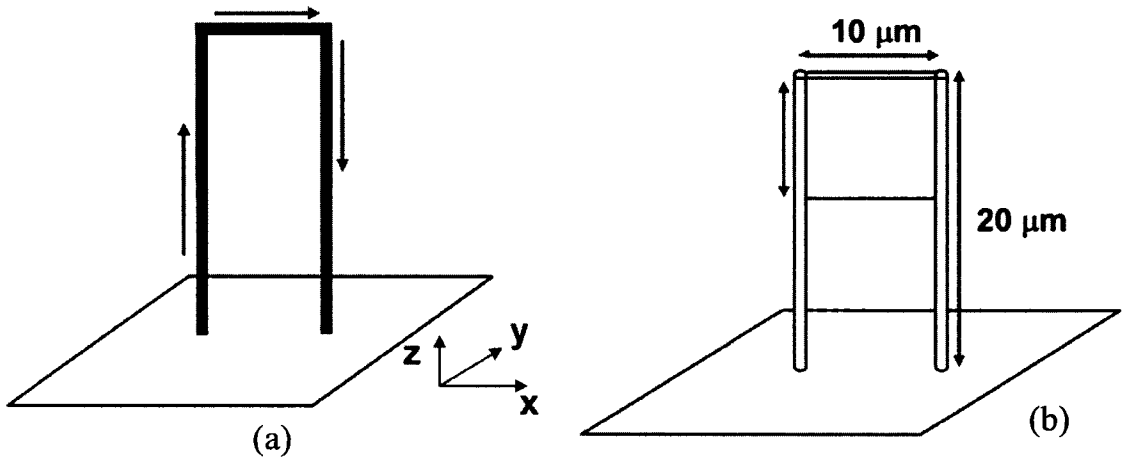

Figure 4.3: (a) Scanning sequence of and (b) schematic structure for floating vertical plane strucure.

Figure 4.4: Projection of a square spiral written in Ormocore. The structure was made at a scanning speed of 75 μm/s and with a beam power of 20 mW.

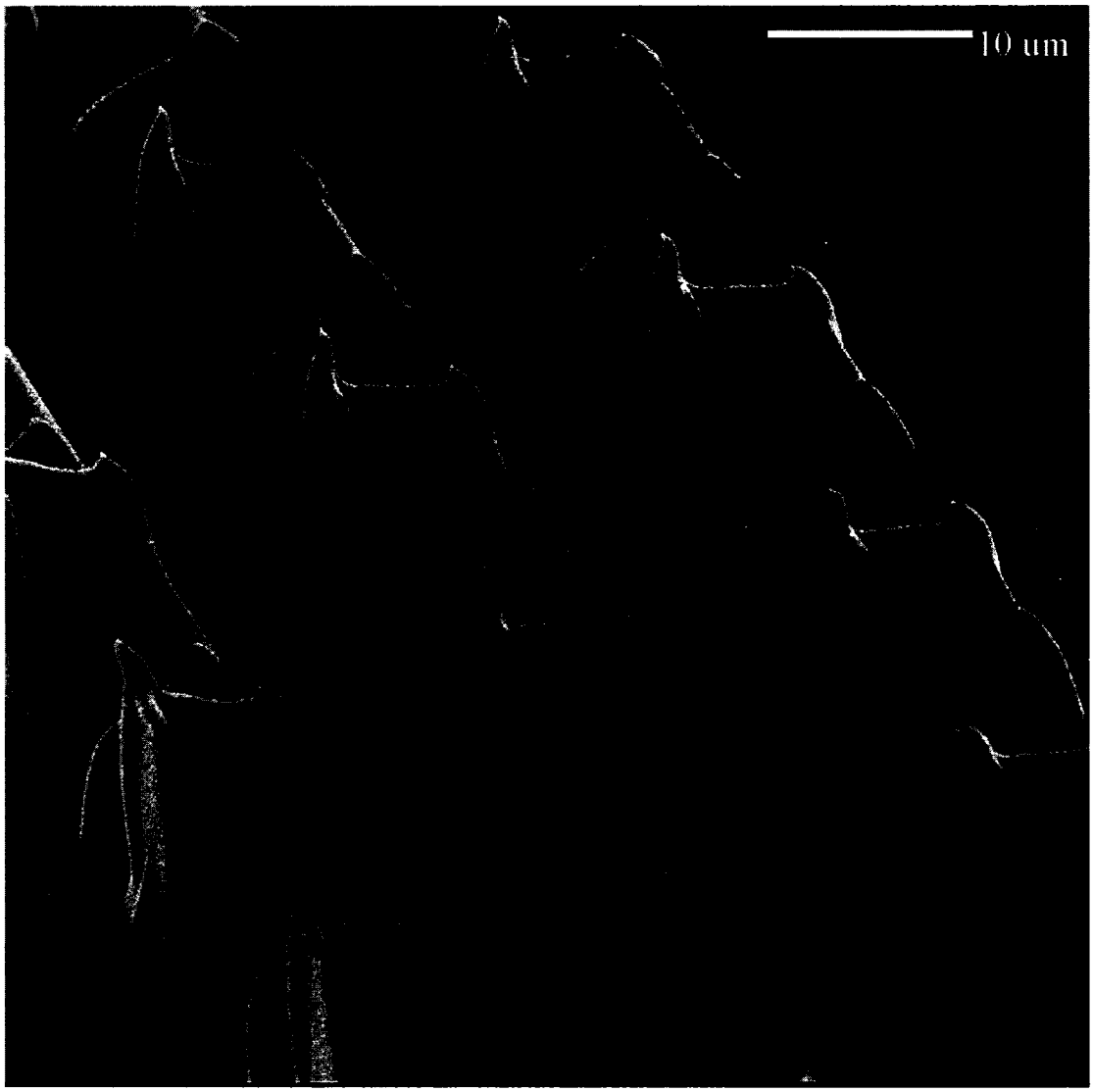

Figure 4.5: Projection of a square spiral written in SU-8 resist. Scanning speed as well as height of the focal point was varied during the experiment. Three rows are written at three different speeds, 25 μm/s (bottom-left column), 50 μm/s and 75 (top-right column) μm/s. The beam power was 20 mW.

Figure 4.6: Vertical planes produced in Ormocore. The beam power was 20 mW and scanning was done at 75 μm/s.

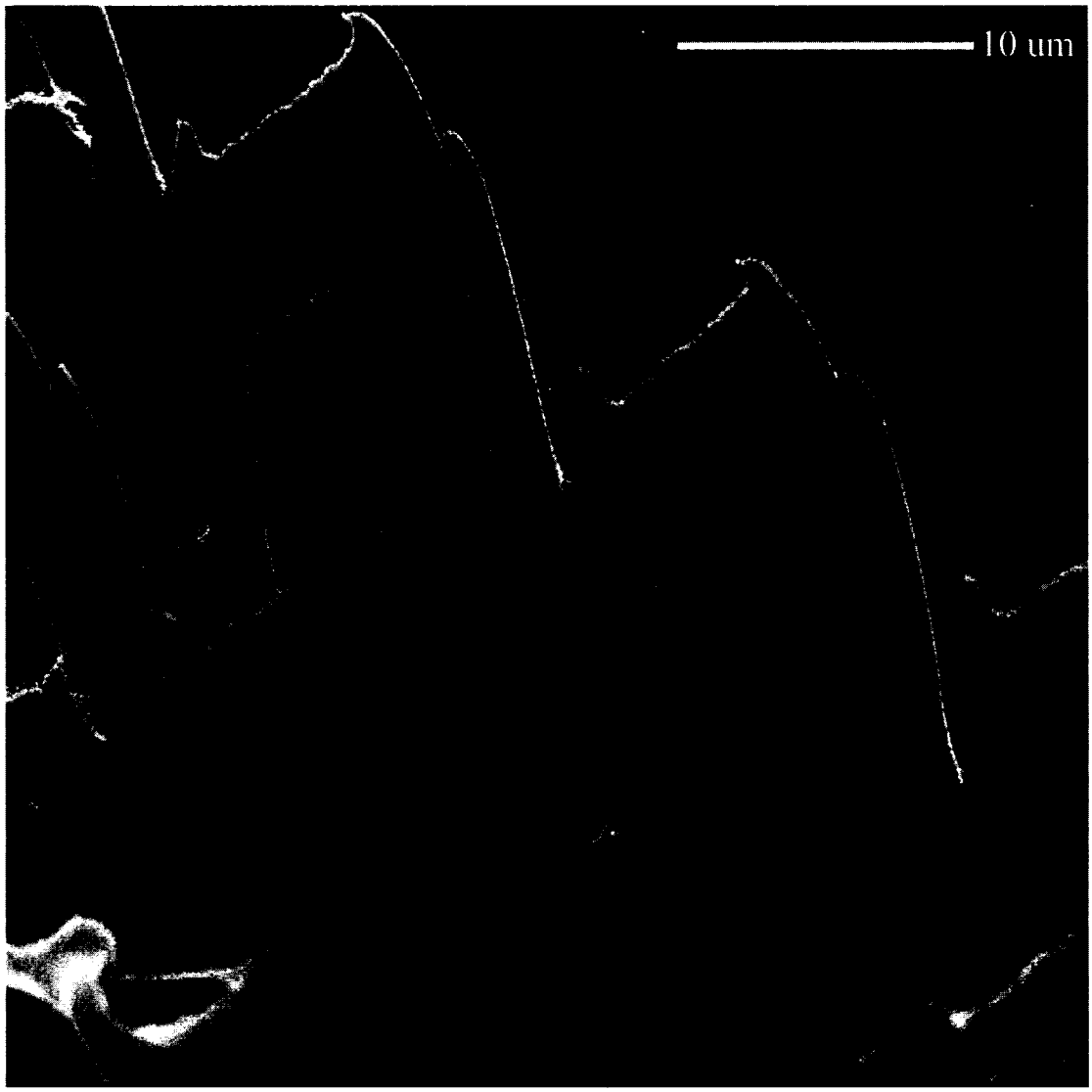

Figure 4.7: Vertical plane written in SU-8 resist. Scanning speeds of different columns are similat to that mentioned in Figure 4.5. The beam power was 20 mW. The right-top column was written at 75 μm s^{-1} while the next column was written at 50 μm s^{-1}.

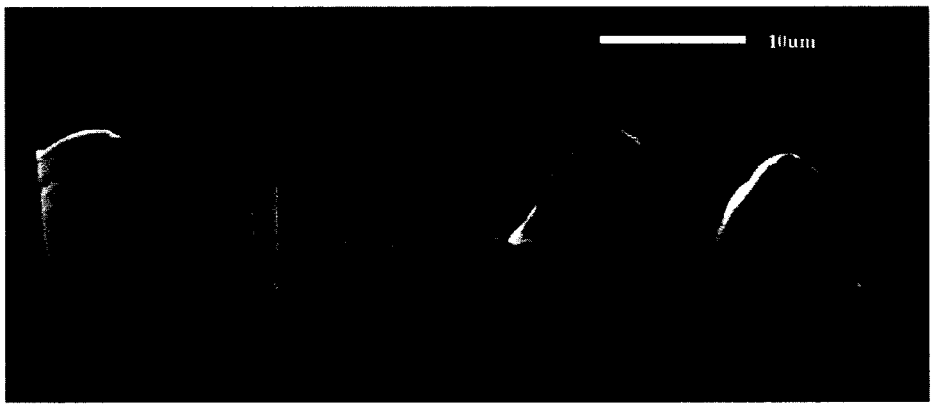

Figure 4.8: An attempt to write complex structure in Ormocore. The beam power was 20 mW. The structure was written at 75 μm s^{-1}.

In contrast, Ormocore being a viscous liquid moves slowly even after the stage stoped moving and this might cause the deformation of the vertical posts as shown in Figure 4.7. Figure 4.8 shows an attempt to write a complex structures. A 30° tilted 'U of A' was written in Ormocore at a beam power of 20 mW and the scanning speed was 75 μm s^{-1}.

4.3 Characterization of 3D writing

A 3D structure can be considered as a structure composed of voxels at different locations in space. The height and width of voxels for different exposure times and powers can be a suitable way to characterize 3D writing. The characteristic height of the voxel or line is taken as twice the distance from the center of the voxel where the radius is maximum to the upper tip of the voxel. This height was preferably measured using voxels standing up or just falling on the substrate or at least when the center of the voxel was clearly above the surface. This characteristic height is related to the Rayleigh range of the focused beam. Similarly for lines drawn at different scanning speed and beam power, measuring line widths and characteristic heights is an alternative approach for 3D writing charaterization.

4.3.1 Voxels at different control parameters

A mechanical shutter was used to control the exposure time of the voxel writing. The minimum exposure time using a Newport mechanical shutter was 10 ms. The resists were exposed for 10, 30, 70, 100, 300, 700 and 1000 ms for a particular focal position above the surface. A new spot was chosen for every exposure dose and after all the exposure doses the sample was moved closer to the objective by 1 μm and again exposed for different exposure times. Figure 4.9 (a) shows the SEM images of the voxels written in Ormocore at different heights and exposure times for a power of 20 mW. The dimensions of the voxel was measured from the SEM images of individual voxels captured at higher magnification. The voxel drops on the substrate when the voxel is produced with the focal point just above half of the height of a voxel. These fallen voxels were measured by measuring the lines drawn on the images as shown in Figure 4.9 (b). Voxels were written for 15 to 25 mW of laser power on the sample.

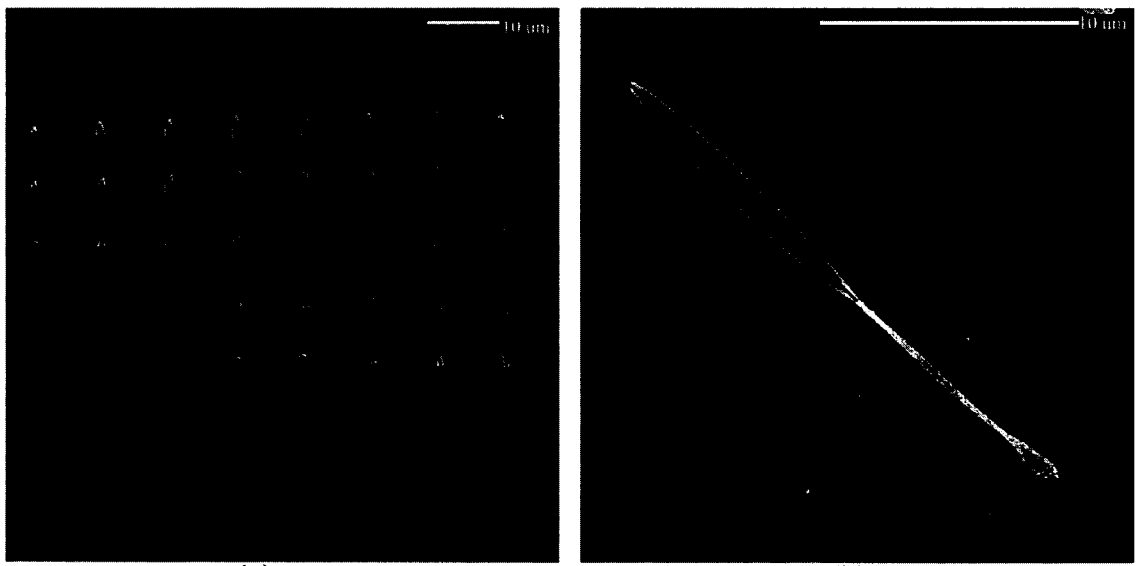

Figure 4.9: (a) Voxels with different heights and written with different exposure times in SU-8 and (b) Demonstration of voxel measurement procedure. The voxel has been produced in SU-8 with 20 mW and 10 ms exposure time.

When a spot is exposed to the laser beam for longer times the characteristic height and width of the voxel increases. Increased the beam power can produce the same

effect. The width or characteristic height of the voxel changes significantly for increase in power or exposure time. The width or characteristic height tends to saturate at higher power or exposure doses and the dimension change becomes slower and slower in this region. The measured characteristic heights and widths of different voxels are given in Figure 4.11 and 4.13 for Ormocore and SU-8, respectively. The minimum voxel width and characteristic height obtained in Ormcore were 1.04 μm and 4.85 μm, respectively. The minimum dimensions in SU-8 were 1.13 μm in diameter and 10.3 μm in length for 15 mW beam power and 10 ms exposure time. When the voxels of Ormocore fall on the substrate they may spread on the substrate resulting in wider voxel diameters. Such fallen over pillars were used for exposure dose of 10 to 300 ms for Ormocore and for 10 to 70 ms for SU-8, respectively. It will be reported in the next section that minimum width of lines produced in Ormocore is around one fourth of the voxel diameters measured here.

4.3.2 Lines at different control parameters

Lines were also drawn at different scanning speeds for different exposure times. The higher the scanning speed, the less time the resist is exposed to the beam. Lines were drawn at 3, 7, 10, 30 and 70 μm/sec for 15, 20 and 25 mW beam powers. All the lines were drawn for a total of 5 seconds to avoid the initial lower velocity region due to finite acceleration. There was 10 to 20 μm separation between lines at different velocities. The focal scanning with 1 μm steps was also performed for each speed. Heights and widths were measured from SEM images. Figure 4.14 shows lines drawn in Ormocore and SU-8 at different scanning speeds with each row at different focal position.

The measured characteristic heights and widths of different lines are given in Figure 4.16 and 4.18 for Ormocore and SU-8, respectively. There were no standing lines of Ormocore on the substrate for scanning speed greater than 10 μm/s at 15 mW beam power. Moreover, measuring the width was a difficult process for the standing structures as there was not a clear edge of the structure. Therefore, results of only 20 and 25 mW are presented in the graph.

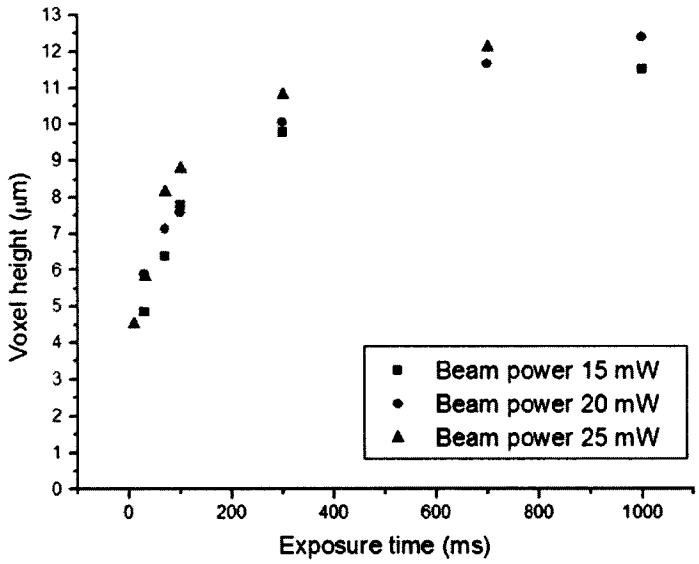

Figure 4.10: Voxel characteristic heights at different beam powers and exposure doses fabricated in Ormocore. The heights were measured from the fallen structure for exposure dose of 10 to 300 ms.

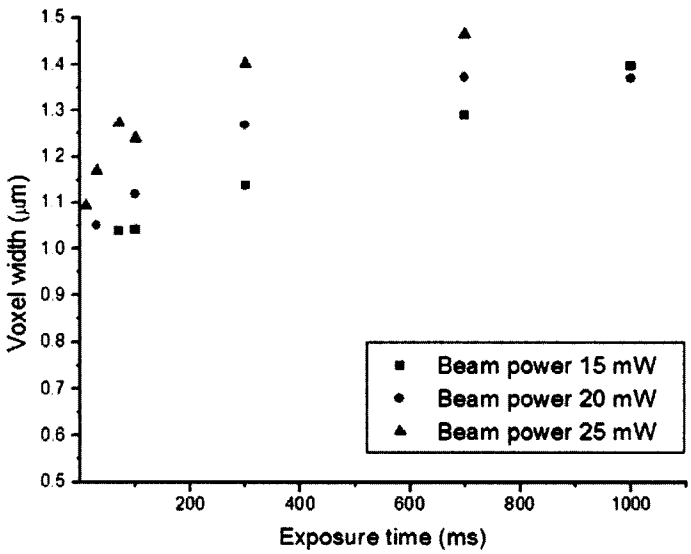

Figure 4.11: Voxel widths at different beam powers and exposure doses fabricated in Ormocore. The widths were measured from the fallen structures for exposure dose of 10 to 300 ms.

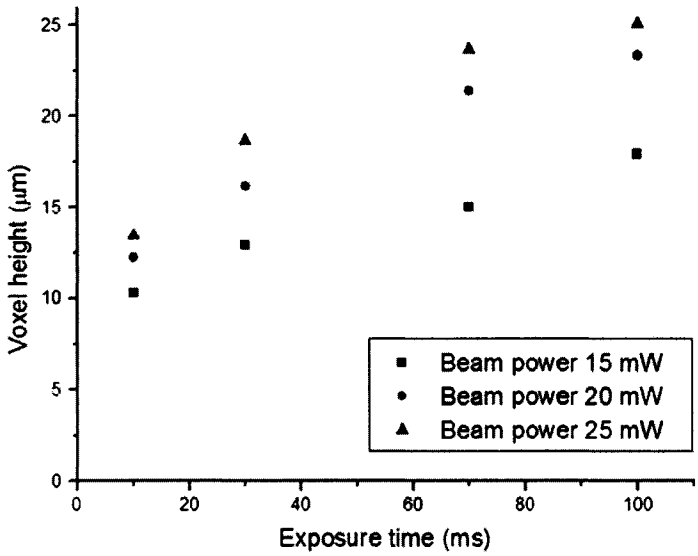

Figure 4.12: Voxel characteristic heights at different beam powers and exposure doses fabricated in SU-8. The heights were measured from the fallen structures for exposure dose of 10 to 300 ms.

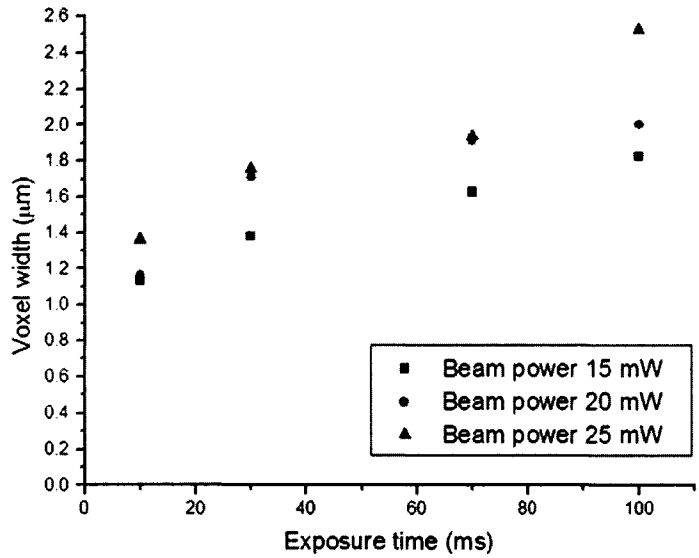

Figure 4.13: Voxel widths at different beam powers and exposure doses fabricated in SU-8. The widths were measured from the fallen structures for exposure dose of 10 to 30 ms.

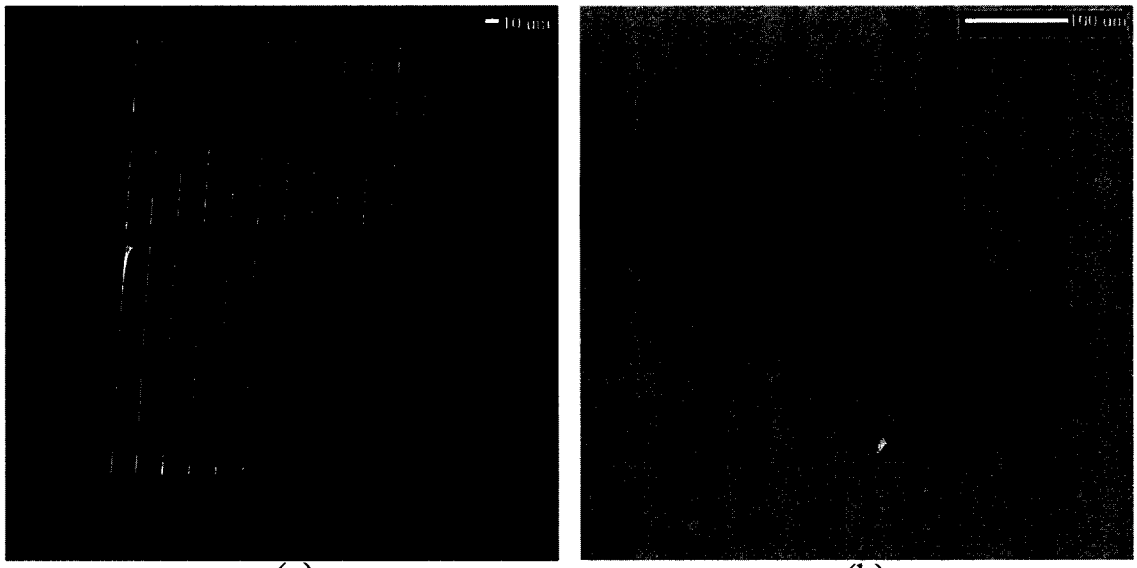

Figure 4.14: Lines drawn with different velocities. Longest lines were drawn at 70 μm/s. Other velocities are 30, 10, 7, 3 and 1 μm/s. The beam powers for (a) Ormocore and (b) SU-8 sample shown in the figure were 20 and 15 mW, respectively.

The minimum width and characteristic height obtained for Ormocore were 270 nm and 2.5 μm, respectively for 20 mW beam power and 70 μm/sec scanning speed. Lines with minimum width of 1.3 μm and 11.4 μm characteristic height were produced in SU-8 for 15 mW beam power and 70 μm/s scanning speed. Drawing lines produced more stable and high resolution structures in resists than making dots or voxels.

4.3.3 Ultra high aspect ratio walls

The real height of a line or wall was higher than the characteristic height of the line. The height of the floating vertical of the walls, as shown in Figure 4.6 and 4.7, are comparable to the measured characteristic heights as presented in the last sections. But for the same beam power and scanning speed, when the floating plane is closer to the substrate there is a secondary structure just beneath the vertical plane as shown in Figure 4.19 and there is a gap between these two planes. Surface adhesion chemistry, the catalytic effect of surface, and reflection enhancement of the field intensity near the surface may be possible reasons for such structures. Bogdanov

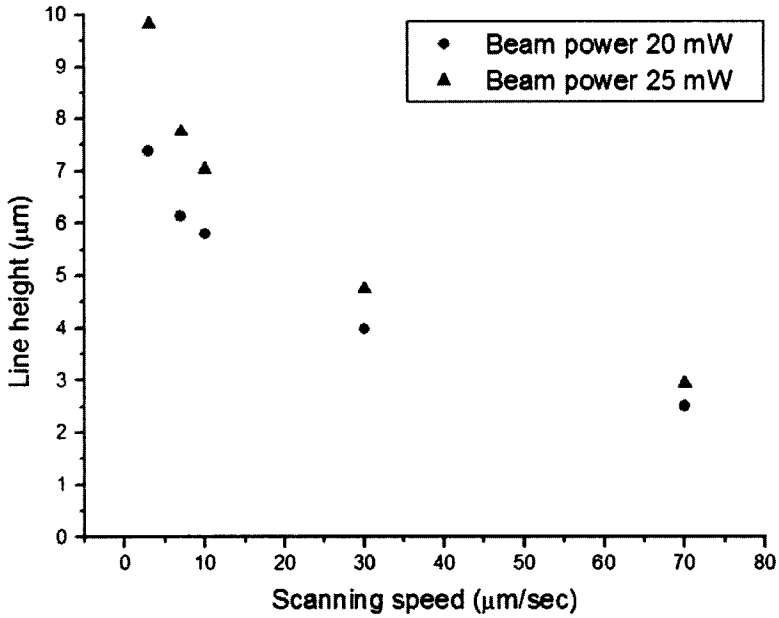

Figure 4.15: Line characteristic heights at different beam powers and scanning speeds fabricated in Ormocore.

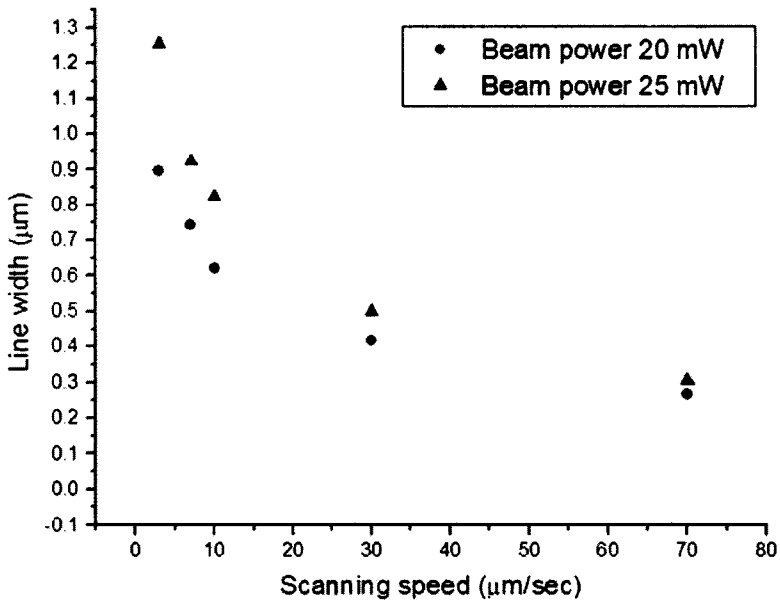

Figure 4.16: line widths at different beam powers and scanning speeds fabricated in Ormocore.

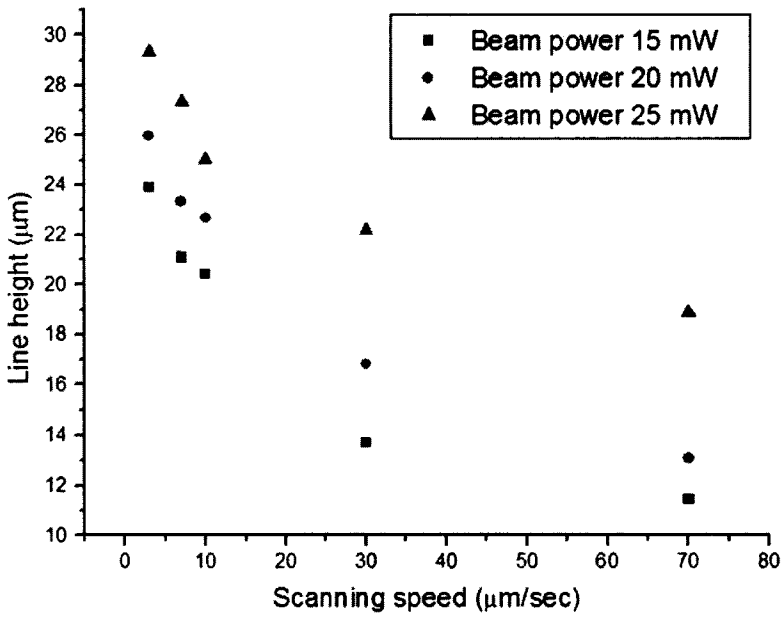

Figure 4.17: Line characteristic heights at different beam powers and scanning speeds fabricated in SU-8.

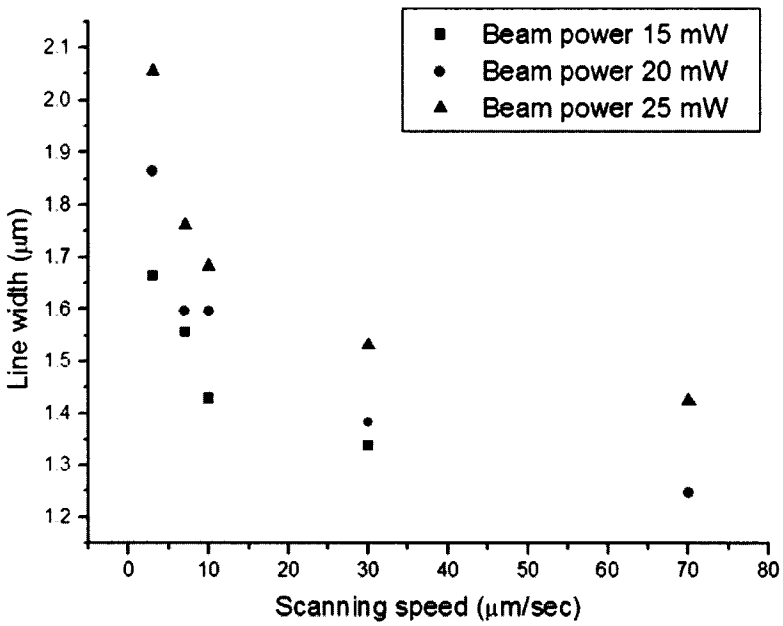

Figure 4.18: Line widths at different beam powers and scanning speeds fabricated in SU-8.

et al [32] reported wider base/foot of pillars due to emission of photoelectrons from the substrate surfaces. In this paper the 8 μm pillars were produced using x-ray lithography and the pillers were 9 μm wide at the bottom. For suitable distance between the substrate and the focal point of the beam there will be no gap between these two sections and it may make a tall wall with very small width. Figure 4.20 shows an ultra high aspect ratio wall fabricated in Ormocore with 20 mW beam power and 70 μm/s scanning speed. Similar structure can be produced even at 25 mW for similar speed. But there are additional fringes at the base of walls drawn at 25 mW but scanned at lower speed. Fringes like that is also visible in walls produced in SU-8 resists.

The apparent height of the wall observed in Figure 4.20 is 10.9 μm. However the images were taken at an oblique angle of 60°. The height appears 13.5% smaller for this angle. The real height is 12.6 μm and width is 310-330 nm Thus the aspect ratio for the wall is around 40.

4.4 Summary

Spatial confinement of photochemical reaction due to TPA process together with the high numerical aperture focusing allows 3D structure writing using this process. Different 3D structures were produced using two photoresists, Ormocore and SU-8, for an 800 nm, 80 fs, Ti:Sapphire laser pulses together with a 40X objective. The linear absorption was negligible in the resists for the fundamental laser wavelength.

Simple 3D structures were chosen to characterize the writing process and 3D writing capability. Various 3D structures were written using the resists. Heights and diameters of voxels produced at different power and for different exposure time were measured. The minimum diameter and characteristic height measured for voxels in Ormocore were (1.04 $\pm$ 0.1) μm and (4.85 $\pm$ .24) μm, respectively. For SU-8 the minimum diameter and characteristic height were (1.13 $\pm$ 0.1) μm and (10.3 $\pm$ 1) μm, respectively.

Lines with very high aspect ratio were also characterized experiment. The mini-

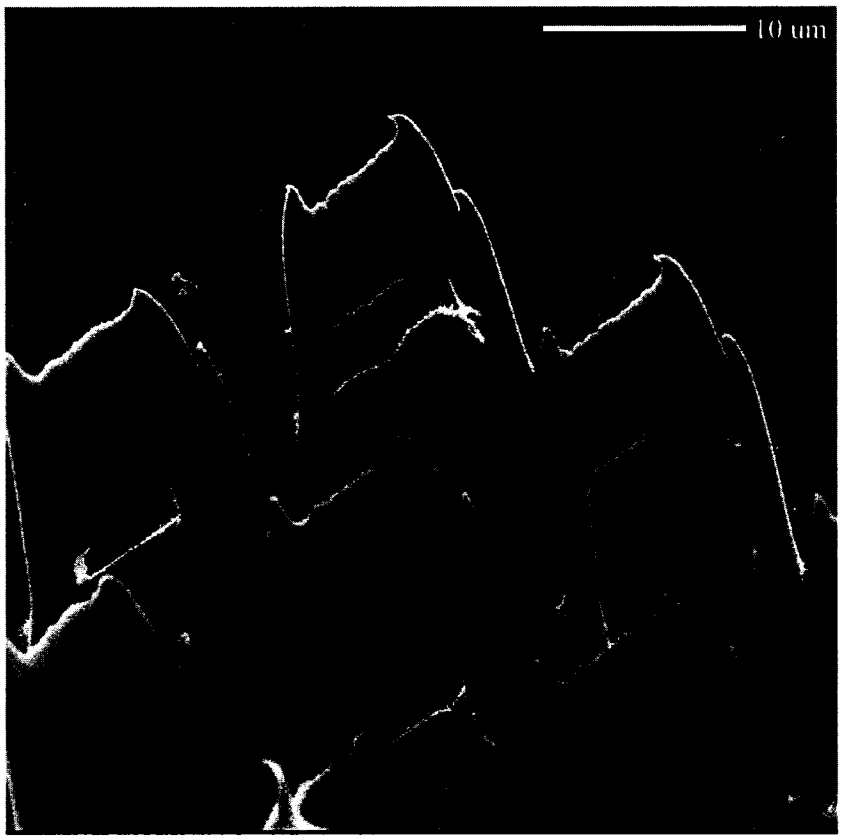

Figure 4.19: Formation of structures along beam path but at positions away from the focal point. Standing plate structures written in SU-8 resist for beam power of 20 mW and scanning speeds of 75 μm s^{-1} and 50 μm s^{-1}.

mum width measured for lines drawn at 70 μm/sec scanning speed at 20 mW laser power in ormocore was 310-330 nm. The height of the line was 12.6 μm giving an aspect ratio of $\approx$40. This is the largest aspect ratio reported for lines/walls written using TPA process. Previously the highest reported aspect ratio was 23:1 as produced by Teh et al [26].

A structure where height incresed gradually while moving along the arm of a square was the first one to demonstrate the performance. Secondly a floating vertical plane held by two posts at the ends of the plane was fabricated. To produce the structure, the focal spot moved vertically away from the sample then moved parallel to it and finally moved back into the sample surface. Mechanical strength and stability of the resist during the exposure and development process can be assessed by these

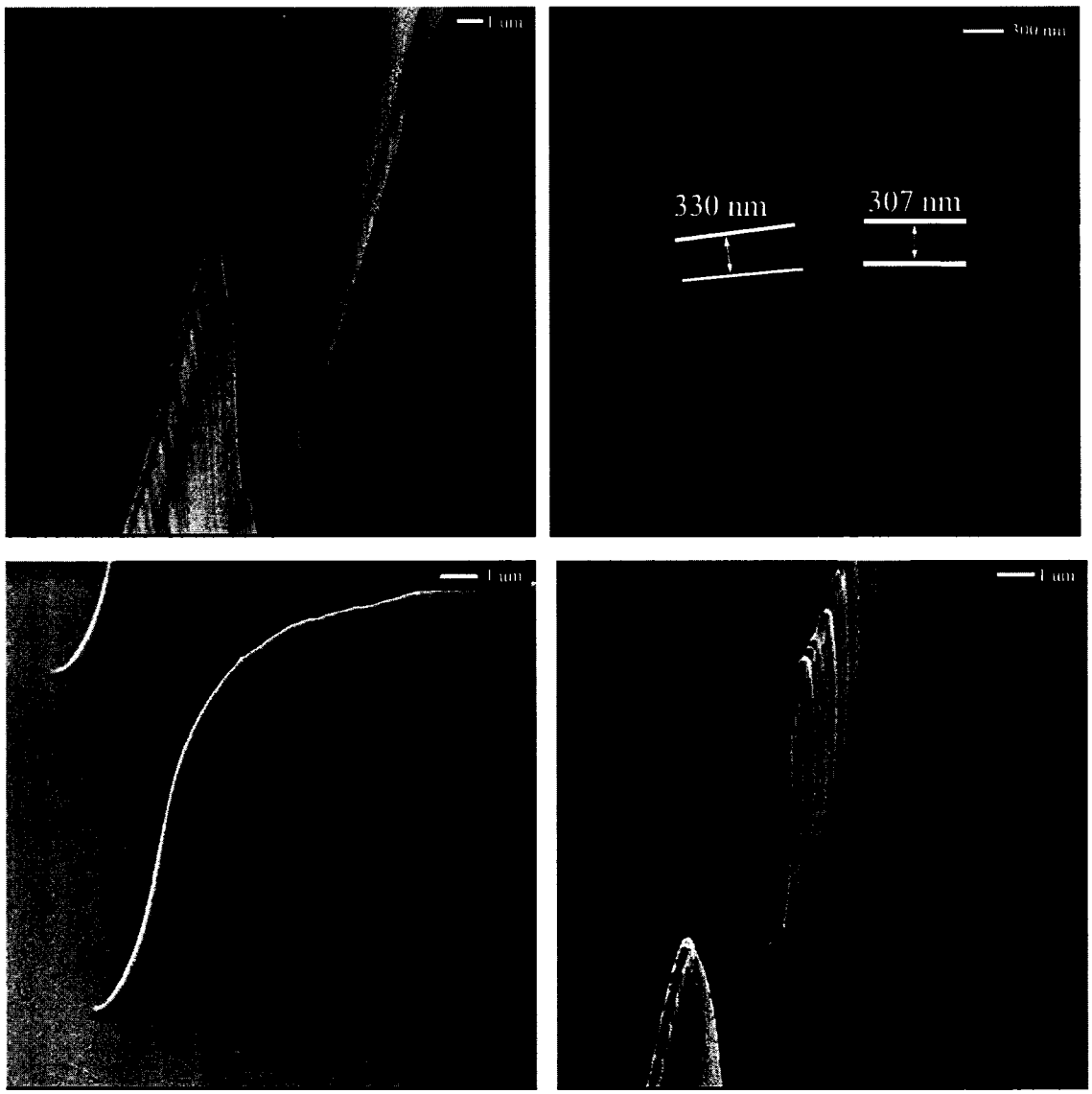

Figure 4.20: [CW from top-left picture] (a) Fringes at the base of a wall due to structures produced at locations other than focal points, (b) top, (c) side and (d) front view of the wall with ultra high aspect ratio. All the structure were fabricated in Ormocore. The beam power and scanning speed for (a) was 25 mW and 30 μm/s, respectively. Structure shown in (b), (c) and (d) were scanned at 70 μm/s with 20 mW beam power.

structures. Slow scanning speed was essential for the stability of the stage control program and for less vibration while writing of the samples.

Complex structures for photonic crystals or MEMS application can be produced using further modification of the scanning system. Moreover, use of 100X objective will open a new window as the lateral dimension of the voxel will be reduced producing more spherical voxels.

Chapter 5

Future work and conclusion

Laser-materials processing has promising applications in different fields of interest. Specifically laser micro-machining has potential applications in semiconductor industries, MEMS devices, biomedical chips, etc. Light absorption due to SPA process has been utilized in laser cutting, drilling, welding, writing and other processes. The limitation of SPA process is that it can not be used to write 3D structures since light absorbs throughout the material. The TPA process, on the other hand, is suitable for such 3D structure writing as the absorption occurs at the focal point of the laser beam where intensity is above some threshold value. 3D structure writing in different photoresists was performed and the performance was characterized in the thesis.

5.1 Future work

5.1.1 Modification to current setup and writing mechanism

Simple structures were written in the resists to demonstrate 3D writing capability. More complex structures can be written with modification in the scanning scheme, stage-assembly and shutter system. The mechanical stage-assembly used in the set up had very high resolution. The minimum step that it could take was 7 nm. It was suitable for drawing lines along single axes by controlling one stage of the assembly. It was complicated to move a very short distance when more than one stage was

involved. The time to accelerate to different velocities became significant compared to the time it has to travel. So, it was physically difficult to start and end all the stages at the same time when they are traveling different distances at different velocities. Slow scanning speed is a solution to this problem but it makes writing more time consuming. Piezo-stages are an alternative solution to DC motor stages which also have a very high resolution but would have similar mechanical problems for multi axes motion.

It is important to have an efficient scanning scheme while writing complex structures. A matlab code was developed to scan two dimensional (2D) images. A 3D object can be built up as a series of 2D surface profiles. The code calculates a trajectory to write that surface profile in an efficient way using raster and vector scan. In a raster scan all the points to be written are exposed to the laser beam using a shutter for the laser, while in a vector scan boundaries of different closed surfaces are scanned.

A 3D structure can be sliced into surfaces at different heights and then an optimized scanning scheme can be determined using the similar algorithm. The code to find the scheme for 2D cases is given in Appendix A.9. Commercially available piezo-stage assemblies sometimes comes with software to find the efficient scanning sequences.

The mechanical shutter used in the present study was too slow to allow fast writing of the resists. Moreover, too frequent on and off operation can break the plate used inside the shutter. An accousto-optic shutter/deflector that can control the deflection of the beam is a good alternative to the mechanical shutter. The beam can be deflected from 0 to 1.4° using the Accousto-optic deflector (AOD) currently available in the Laser Plasma lab. The deflection angle can be set to 0 degree when the writing is required. The 1.4 ° deflection is enough to take the beam out of the objective aperture if the deflector is placed far away. The transition time required to switch between these two positions is 15 μsec. By varying the RF frequency to the AOD the deflection angle can be varied and the AOD used as a rapid scanning system. Such a rapid scanning technique would solve many of the mechanical scanning problems

discussed previously. Thus, a combination of a precision mechanical positioning stage to move the substrate position together with an AOD to carry out rapid scanning in a specific region of the substrate is the ideal scanning combination.

However the deflection of the beam by AOD is wavelength dependent and the laser used in the experiment has a large band width of around 10 nm (FWHM). Thus the finite bandwidth causes significant spreading of angle leading to elliptical focal spots. Therefore, circular beams appear elliptical with 45° tilted axes after a two dimensional AOD system. The angular dispersion can be corrected to the first order for one deflection angle by introducing compensating angular dispersion from a prism. An SF14 prism that gives different angle of deflection dependent on wavelength when the beam passes through the prism can be used to correct the dispersion due to finite bandwidth. In the prism the dispersion is opposite to the AOD. The pulse width spread due to materials like the prism and AOD crystals can be compensated by adjusting the grating compressor in the chirped laser pulse amplifier.

The diffraction limited focal spot is smaller for shorter wavelength lasers. For this reason, higher resolution can be achieved by using shorter wavelength laser writing. Frequency doubled Ti:Sapphire fs lasers should be the next step toward that goal. Polymethyl methacrylate (PMMA) is a suitable candidate for the writing material. Yamasaki et al [46] demonstrated 3D optical memory writing in PMMA using single-pulse irradiation at 532 nm, picosecond and 400 nm, fs pulses. Further improvement in resolution can be obtained by going to the third harmonic, 266 nm, of the Ti:Sapphire laser system usin a VUV resist.

5.2 Conclusion

Two photon absorption, a nonlinear absorption process, has been investigated for applications in 3D structure writing. SU-8 and Ormocore, two widely used commercially available photoresists, were characterized and utilized for writing of 3D test structures.

Absorption of energy by the resist during the exposure and the etching behavior

of the resist for different absorbed power determine the final structures produced in the resist. The single photon absorption process was utilized to characterize the resist etching as a function of energy absorbed per unit volume. The absorbed energy was calculated from the absorption coefficients of the resists at different wavelength and the spectrum of the UV source. The etch rate was found to vary logarithomatically for Ormocore but appeared more as a step function for SU-8. Undercutting is a possible reason for such a step function. The sensitivity for SU-8 measured from the experiment was (3.8 ± 0.2) J cm^{-3}. On the other hand, the sensitivity and contrast for Ormocore were (54 ± 2) J cm^{-3} and (15 ± 1) μm J^{-1} cm^3 per decade, respectively.

Single photon absorption was negligible in the resists for the 800 nm femtosecond laser wavelength used for the TPA experiments. Single shot femtosecond exposures were used to determine the TPA coefficients from the measured transmission through the resists. The TPA coefficients measured for 0211 glass, SU-8 and Ormocore are (1.4 ± 0.2) cm TW^{-1}, (28 ± 6) cm TW^{-1} and (30 ± 6) cm TW^{-1}, respectively.

3D structures were written using this TPA process together with a 40X microscope objective. Projections of a square spiral and floating vertical plane were fabricated in the resists. Lines and dots were also drawn to find their width and/or height variations for different irradiation parameters. Vertical walls with very high aspect ratio up to 40 were produced as a result. These various test scans should be valuable as test cases for resist modeling codes for predicting resultant structures based on the above measured etch rates and two photon absorption coefficients.

In the future improved accousto optic scanning techniques and employment of the second and third harmonics of the Ti:Sapphire laser system should allow much higher resolution structures to be written. For frequency doubled Ti:Sapphire laser around 60 to 75 nm resolution should be ultimately achievable using PMMA, a resist used for X-ray lithography and for third harmonic illumination with VUV resists features below 50 nm may be possible.

Appendix A

A.1 Spectral efficiency of the spectrometer

The Ocean Optics spectrometer USB-2000 was used to analyze the spectrum of the UV source. The minimum resolution of the #2 spectrometer was 1.34 nm and it views a wide spectrum from 200 to 800 nm. The resolution and bandwidth is calculated from the slit width and type of the grating used which were 25 μm and 600 lines per mm, respectively. Figure A.1.1 shows the efficiency of the spectrometer while measuring intensities at different wavelengths of the operating region. The curve is provided by the manufacturer.

A.2 Surface profile SU-8

Surface profiles for two samples of SU-8 were measure using an Alpha Step 200 profilometer. Due to similarity of the patterns in these two samples, profiles for only one sample are shown in this section. Exposure time was varied from 2 seconds to 9 seconds with a step of 0.5 seconds. SU-8 had a very sharp transition with exposure time. Measurements were taken until the transferred pattern did not change considerably with increase of the exposure time. Figure A.2.1-A.2.6 shows the variation of surface profile with exposure time. No structures were observed below 5 seconds exposure time.

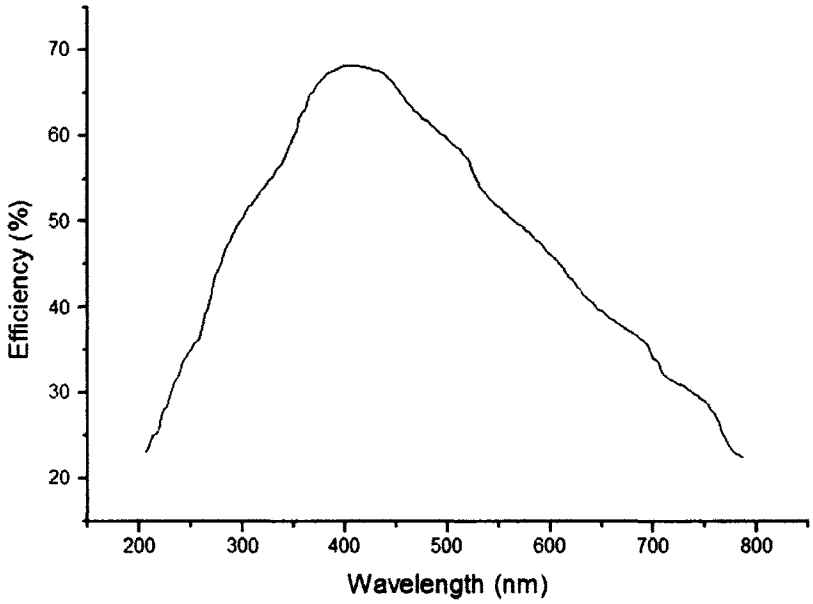

Figure A.1.1: Efficiency of the Ocean Optics spectrometer at different wavelengths.

A.3 Optical properties of different materials

Absorption coefficient in m^{-1} or absorption in dB m^{-1} determines the SPA inside a material. Moreover, refractive index is an important parameter to find the reflected and transmitted energy at the surface of two materials. Reflection at the mask to transfer a pattern to the resists, at the air-polymer or mask-polymer surface is important to accurately predict the resists behaviours. Important parameters collected from different sources or measured using available tools are presented in this section.

A.3.1 Refractive index of Ormocore

Refractive indices of the resist for 635, 830, 1310 and 1550 nms are available at the manufactururer's website [3]. Indices for operating wavelengths were found based on interpolation of the available data. Figure A.3.1 shows the variation of the indices with wavelengths.

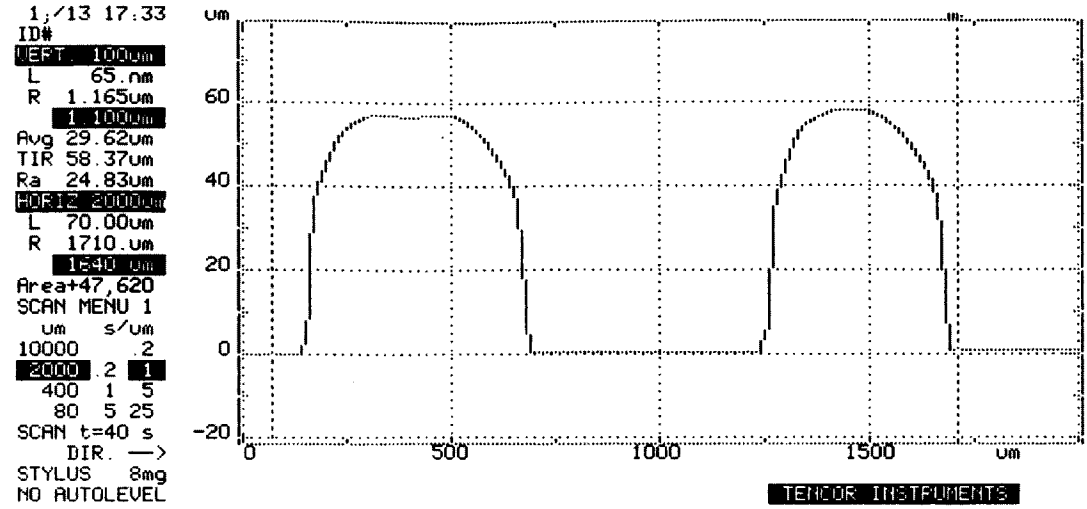

Figure A.2.1: Surface profile for SU-8 bars exposed for 5.0 seconds.

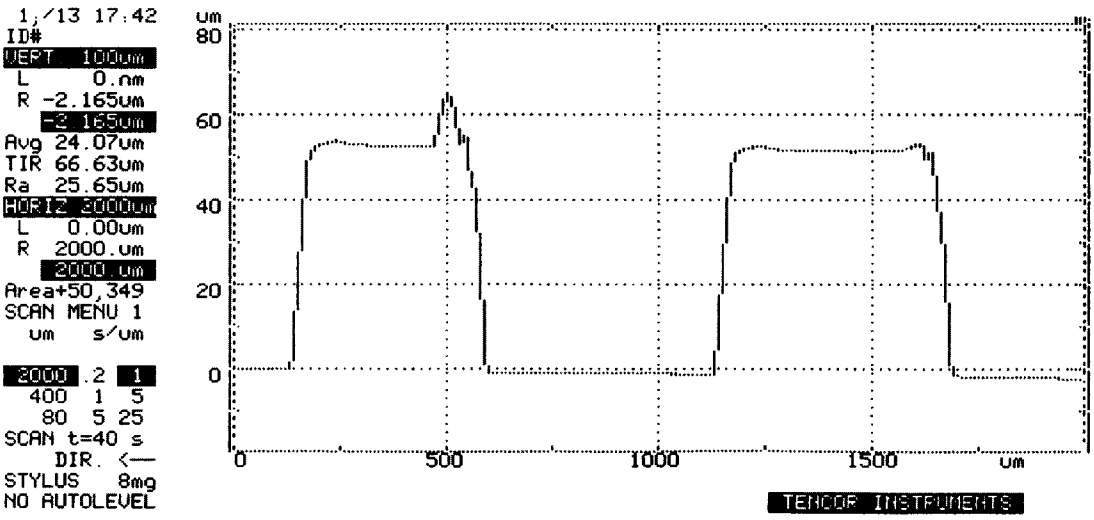

Figure A.2.2: Surface profile for SU-8 bars exposed for 5.5 seconds.

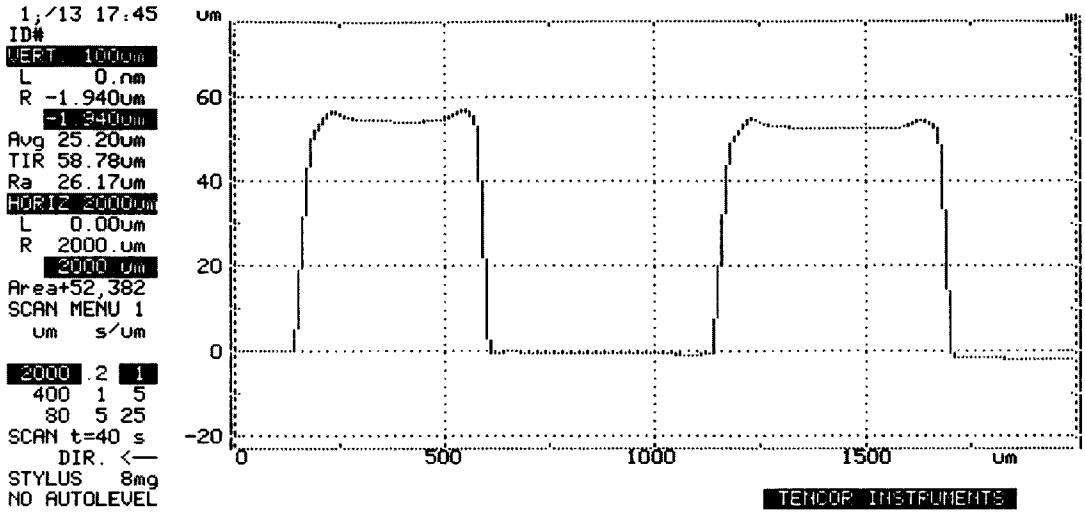

Figure A.2.3: Surface profile for SU-8 bars exposed for 6.0 seconds.

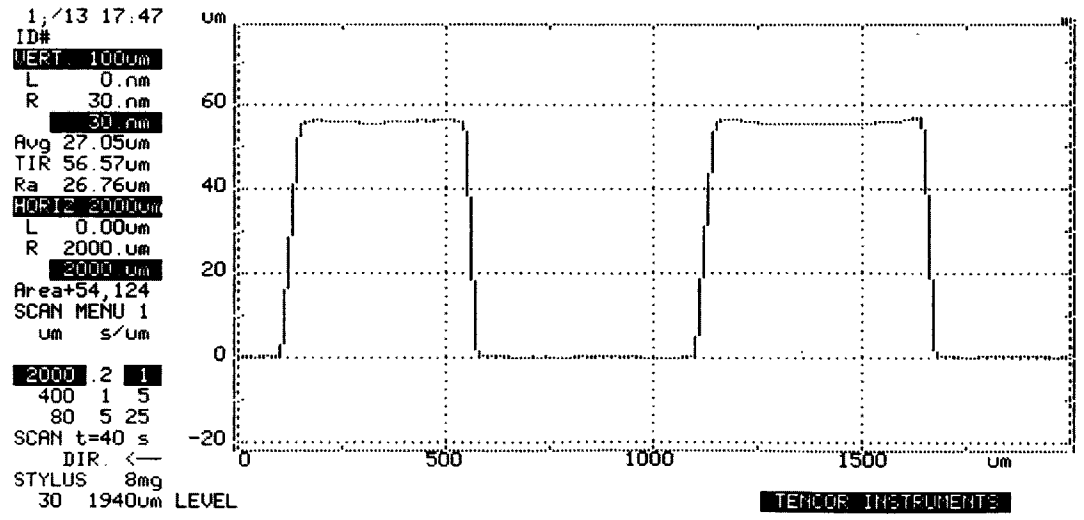

Figure A.2.4: Surface profile for SU-8 bars exposed for 6.5 seconds.

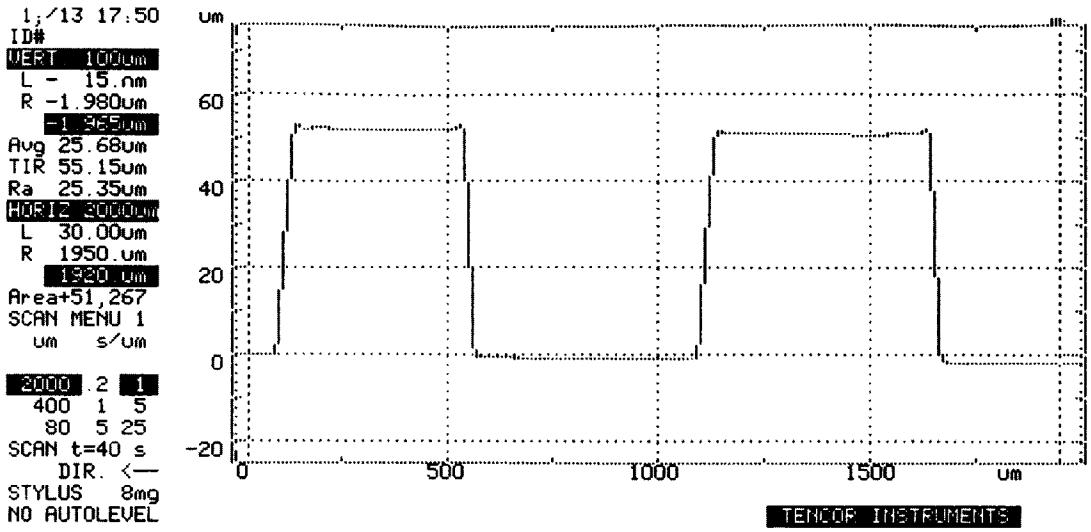

Figure A.2.5: Surface profile for SU-8 bars exposed for 7.0 seconds.

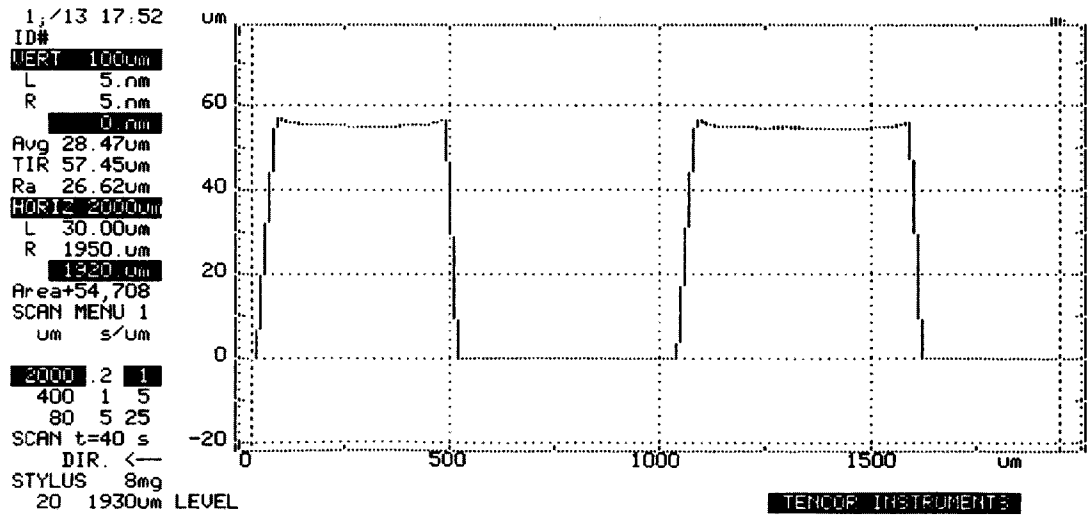

Figure A.2.6: Surface profile for SU-8 bars exposed for 7.5 seconds.

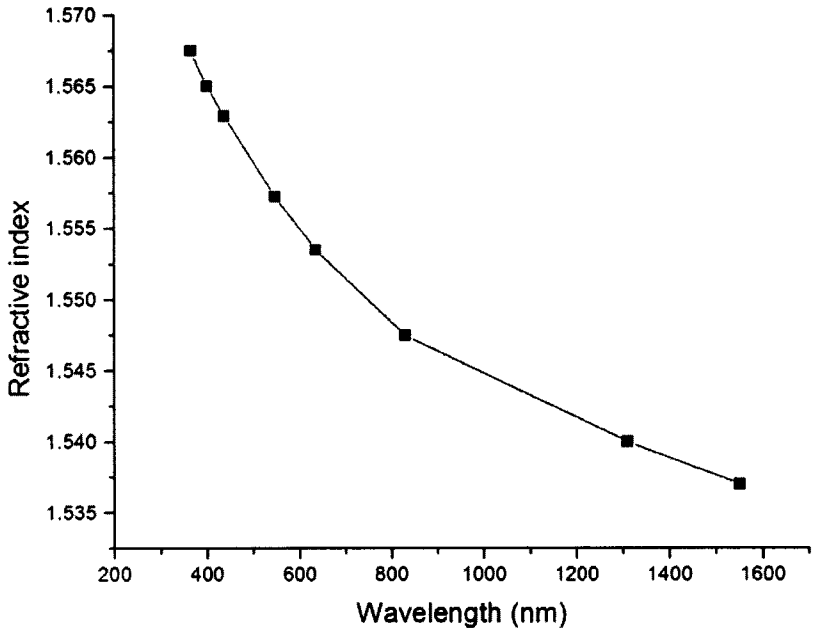

Figure A.3.1: Refractive indices of Ormocore at different wavelengths [3].

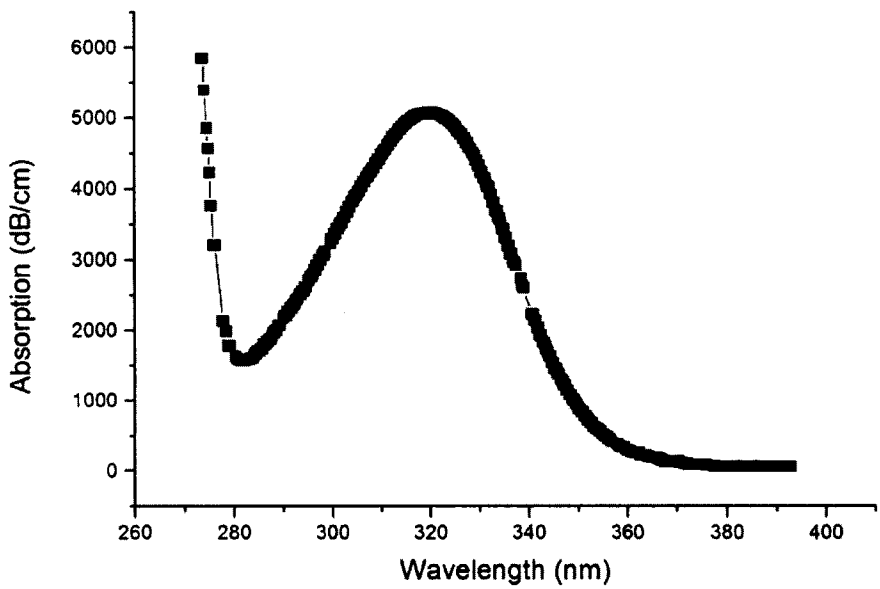

Figure A.3.2: Absorptions in Ormocore in dB/cm for different wavelengths in the UV region [4].

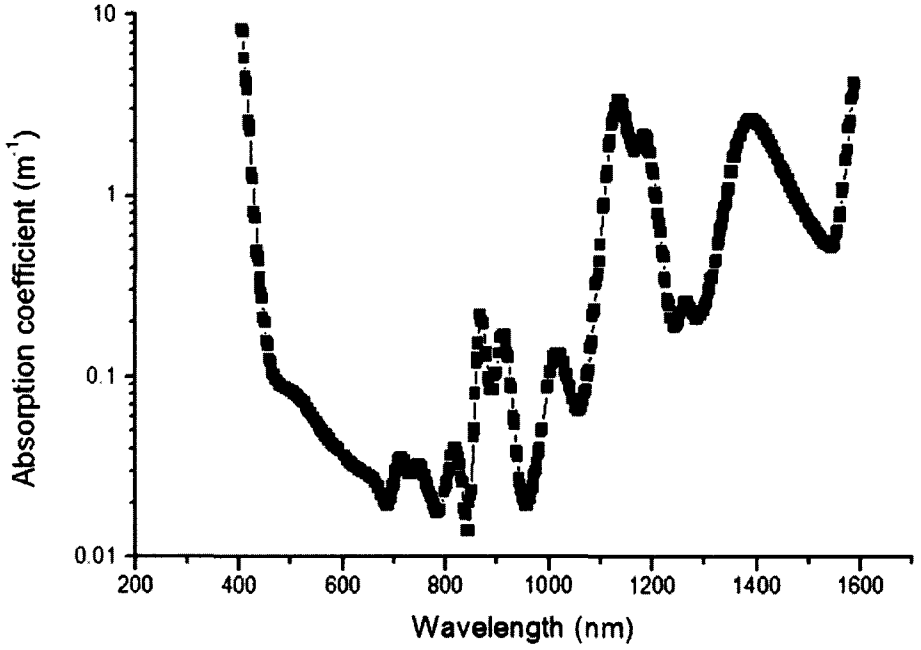

Figure A.3.3: Absorption coefficient in Ormocore for different wavelengths [4].

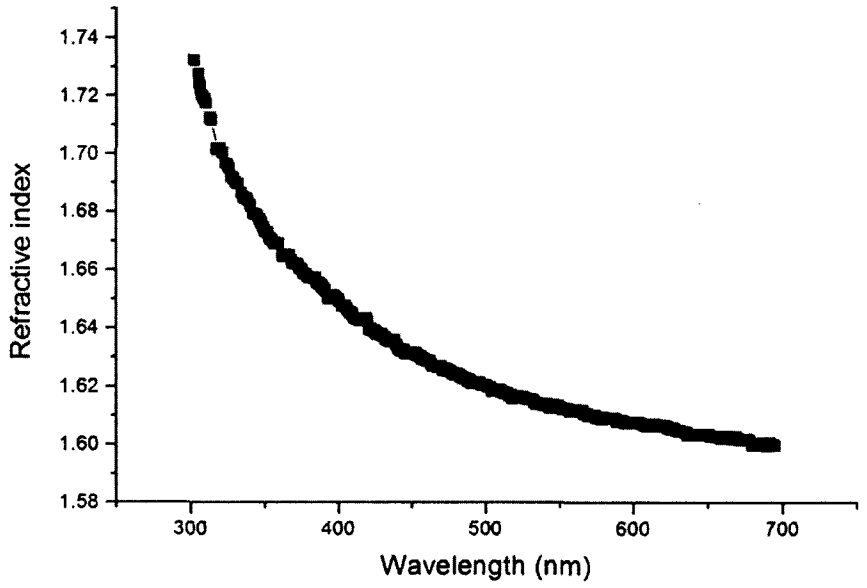

Figure A.3.4: Refractive indices of SU-8 at different wavelengths [5].

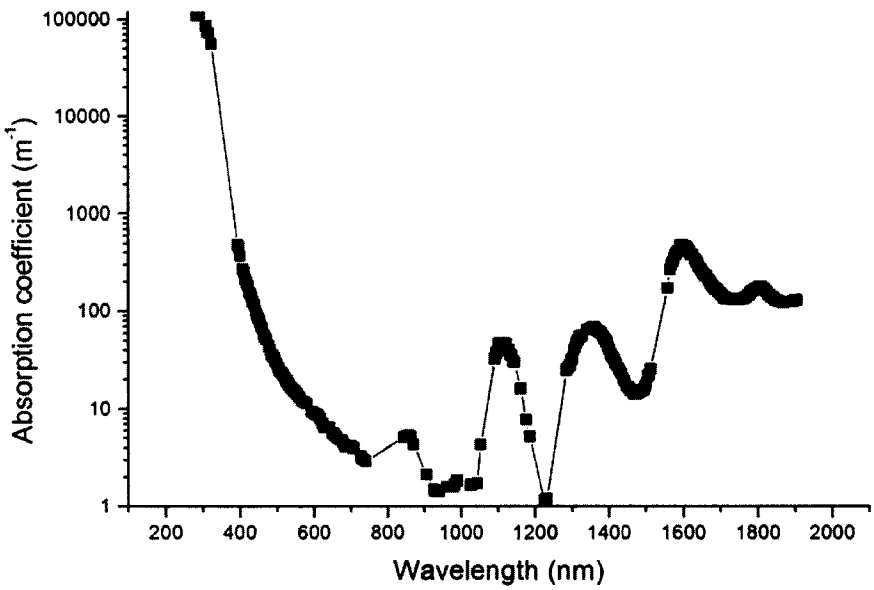

Figure A.3.5: Absorption coefficients for SU-8 at different wavelengths [6].

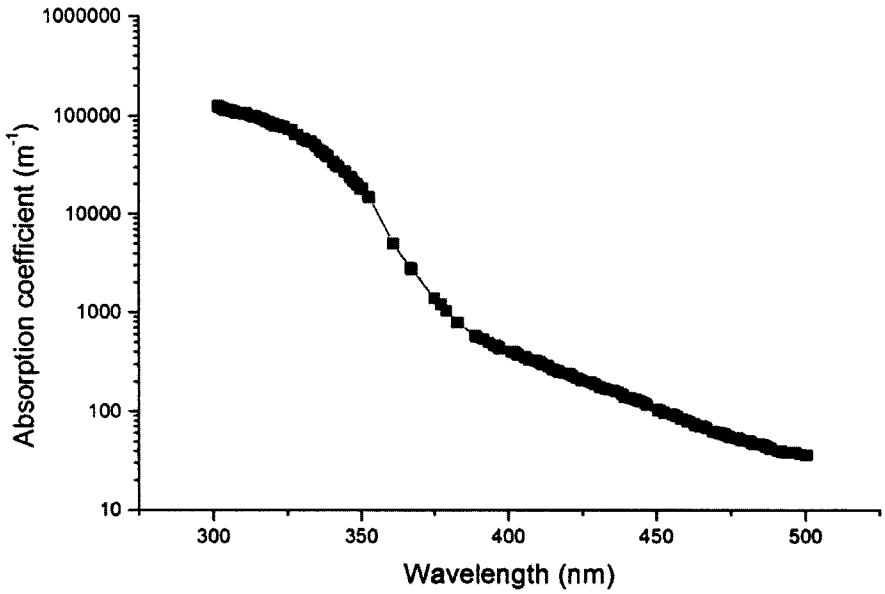

Figure A.3.6: Absorption coefficients for SU-8 for UV wavelengths [6].

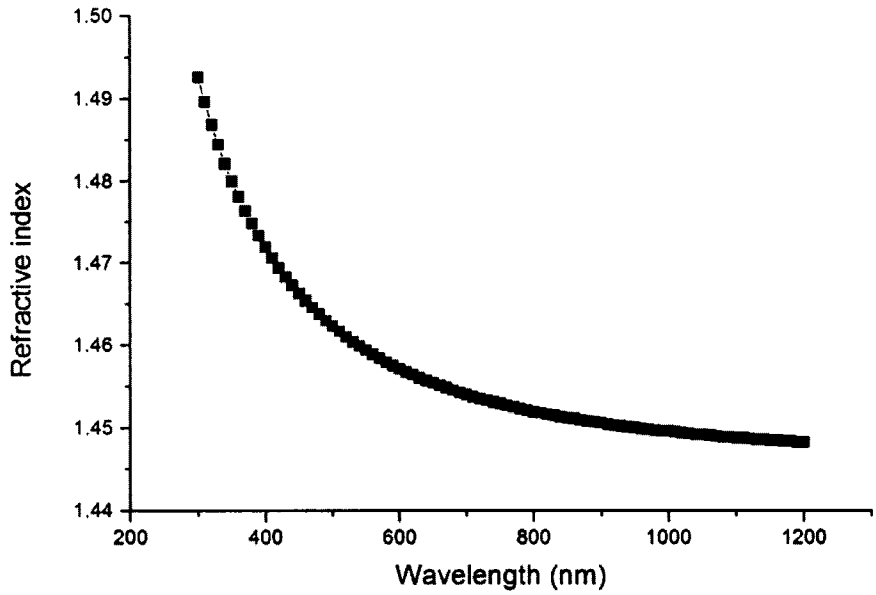

Figure A.3.7: Refractive indices of Quartz, matarial to make the mask, at different wavelengths.

A.3.2 Absorption in Ormocore

Ormocore has significant absorption below 400 nm wavelengths and it is almost transparent to lights with wavelengths above that limit. Figure A.3.2 and A.3.3 shows the variation of absorptions (dB/cm) with wavelengths [4].

A.3.3 Refractive index of SU-8

SU-8 has higher refractive indices at different wavelengths [5] compared to Ormocore as seen in the Figure A.3.4.

A.3.4 Absorption in SU-8

SPA of SU-8 depends on the initial exposure condition. Exposed SU-8 abosorbs more than unexposed SU-8 resists [6]. Figures A.3.5 and A.3.6 show the variation of the absorption coefficient with different wavelengths for unexposed resists as reported in the reference [6].

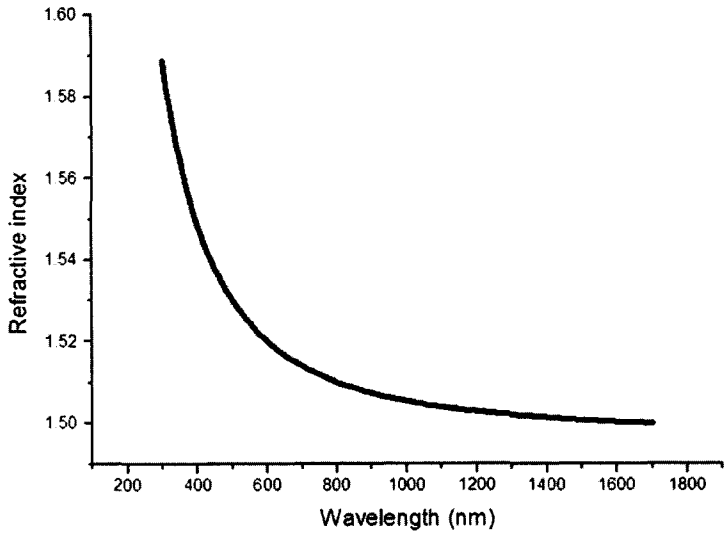

Figure A.3.8: Refractive indices for 0211 glass at different wavelengths.

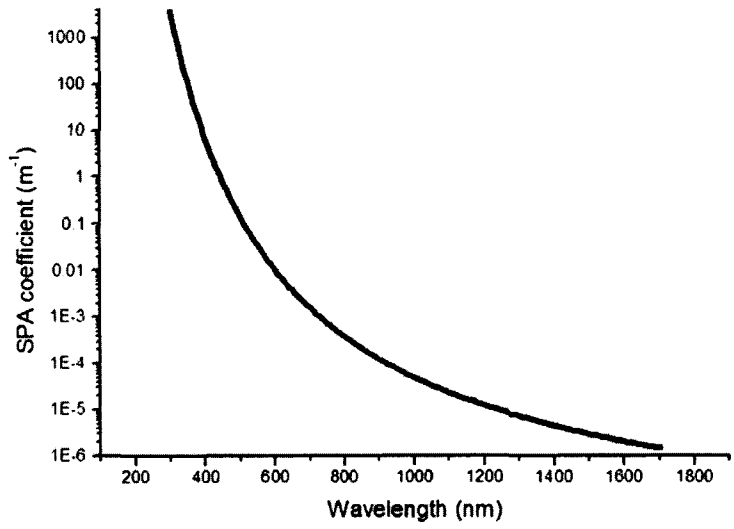

Figure A.3.9: SPA coefficients for 0211 glass at different wavelengths.

A.3.5 Refractive index of the Mask material (Quartz)

The transparent one square inch area on the mask was used to determine the refractive index of the material. The ellipsometer in the nanofab was used for the experiments. Figure A.3.7 shows the variation of the refractive index with wavelengths.

A.3.6 Properties of 0211 glass

A Monochromator (High Speed Monochromator System, HS-190, from J. A. Woollam Co., Inc) available at the Nanofab, U of A, was used to determine the refractive index and SPA coefficient of 0211 glass. Figure A.3.8 and A.3.9 shows the experimentally measured parameters for different wavelengths. For 800 nm wavelength, the refractive index for the material is 1.51 and SPA coefficient is 3.8 $\times 10^{-4}$ m^{-1}.

A.4 Beam profile after a thin lens

When a Gaussian beam centered at z=0 with beamwaist ω_0 is transmitted through a thin lens located at a distance z, as shown in Figure A.4.1, the beam parameters after the lens can be found using the following equations [47],

Beam waist	$\omega_0' = M\omega_0$	(A.1)
Waist location	$(z' - f) = M^2(z - f)$	(A.2)
Depth of focus	$2z_0' = M^2 2z_0$	(A.3)
Divergence	$2\theta_0' = \frac{2\theta_0}{M}$	(A.4)
Magnification	$M = \frac{M_r}{\sqrt{1+r^2}}$	(A.5)
$r = \frac{z_0}{z-f}$	$M_r = \left\lvert \frac{f}{z-f} \right\rvert$	(A.6)

A.5 Beam diameter (horizontal) after the lens

Chapter 3.4.2 mostly discusses the vertical beam waists or radiuses at different locations after the lens. Horizontal beam profiles also closely match the theoretical

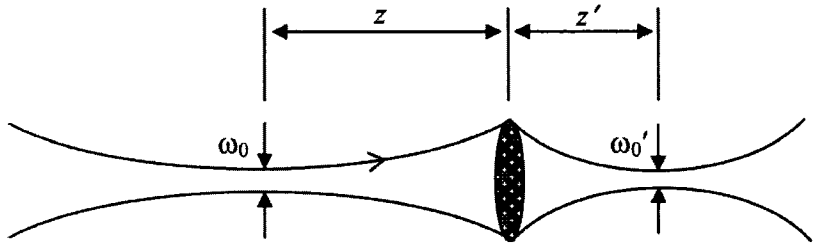

Figure A.4.1: Change in beam parameters after transmitting through a thin lens.

ones at the approximate half way between the lens and the focal point and in the scanning zone. Figure A.5.1 shows the beam waist variation for the horizontal beam at different locations after the lens.

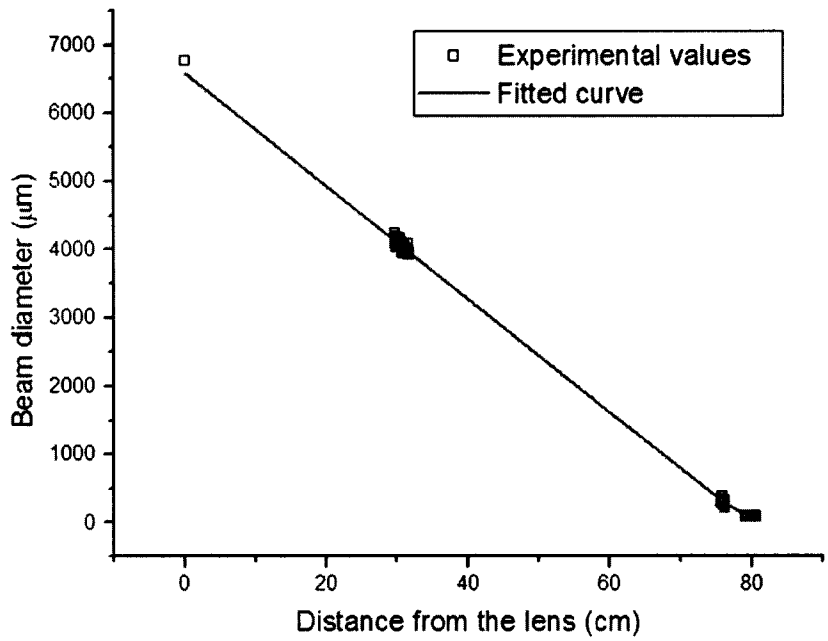

Figure A.5.1: Beam diameter (horizontal) at different positions after the lens.

A.6 TPA coefficients of Fused silica

Table A.6.1 presents TPA coefficients of Fused Silica determined by different research groups.

Table A.6.1: TPA coefficients β for Fused silica

λ [μm]	τ_p [ns]	$\beta \times 10^{11}$ [m/W]	Ref
0.2128	0.023	0.75±0.04	Repeyev et al [44]
0.216	0.15	0.5±0.1	Dmitriev et al [48]
0.2484	0.008	0.08±0.02	Tomie et al [49]
0.2661	0.015	0.05±0.01	DeSalvo et al [50]
0.270	0.015	0.75±0.04	Dmitriev et al [48]
0.282	3	< 0.02	Mizunami et al [51]
0.293	0.004	0.005±0.001	Ross et al [52]
0.2985		0.005	Kim et al [53]
0.308	0.12	0.0078±0.0016	Mizunami et al [54]
0.3507	1-7	< 0.0005	Smith [55]
0.3547	0.017	< 0.00125	Liu et al [45]

A.7 Beam profiles recorded in a CCD

A COHU camera and Spirikon software were used to collect the beamprofile and analyze its parameters. Sprikon software also triggered the shot to be triggered and the opening of the aperture was set so that the camera can capture the image. Figure A.7.1 shows a typical image of the beam close to the surface of the substrate for the first attempt to measure the TPA coefficients of the resists.

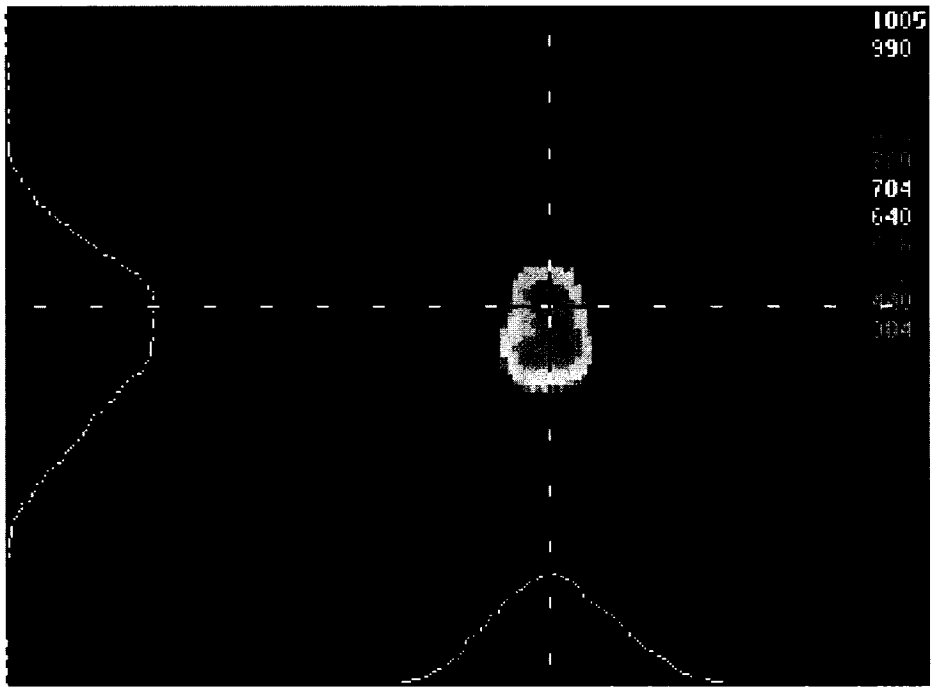

Figure A.7.1: Typical beam profile recorded in CCD camera at the scanning zone.

A.8 Stage performance

The performance of the DC motor stage from Physic Instruments are given in Figure A.8.1. The M 110.1 DG stage was used in the TPA 3D structure writing and total span for that stage was $\approx$ 19 mm.

A.9 Matlab codes to determine scanning scheme

Matlab codes can be used to determine efficient scanning schemes for either raster scan or vector scan approaches. This section presents a scheme to optimize scanning for a 2D images which can be extended to 3D structures. The 2D images containing the imformation about positions to write and not to write coded in ones and zeros will be used to control the movement of the stage-assembly. Section A.9.1 and A.9.2 present the codes used to find the scheme while Figure A.9.1 shows the scanning patterns determined from an image.

TECHNICAL DATA:			
Models	M-110.1DG	M-111.1DG	Units
Travel range	5	15	mm
Design resolution	0.007	0.007	µm
Min. incremental motion	0.05	0.05	µm
Unidirectional repeatability	0.1	0.1	µm
Backlash	2	2	µm
Max. velocity	1.5	2.5	mm/sec
Max. normal load capacity	10	10	kg
Max. push/pull force	10	10	N
Max. lateral force	10	10	N
Encoder resolution	2048	2048	counts/rev.
Drive screw pitch	0.4	0.4	mm/rev.
Gear ratio	28.44444:1	28.44444:1	
Nominal motor power	0.6	2	W
Motor voltage range	0 to ±12	0 to ±12	V
Weight	0.3	0.4	kg
Recommended motor controllers	C-842, C-844, C-860	C-842, C-844, C-860	
Travel range:	**700,000**	**2,100,000**	**[counts]**

Common data:

Gear head ratio: **(116/9):1, 28,44444:1**

Translation Ratio: **145.63555 counts/µm**

Design Resolution: **0.006866 µm / count**

Figure A.8.1: Perfomance of the mechanical stages used for the 3D structure writing using TPA method. Manufacturer: Physik Instrumente (PI) GmbH & Co. KG, www.pi.ws

A.9.1 Main function

```
%clear
%This is the function to produce scanning sequence of the photoresists
%in terms of real distances and real velocities
clc

%Values to convert into velocities and distances
d_p2p_mat=1; %um, distance in um between two points for the given matrix(original image)
% ### in output distance will be in count, 7 nm = 1, because PI stage understands counts
v_v2v_write=1; %unit velocity to write a voxel, this enables to scan at different velocities from Labview
v_v2v_travel=10; %velocity to move to next section without writing on the photoresist

%overlaping parameters
interm_level=0; %No of points in between two clusterred pixel in horizontal/vertical direction
%for diagonal movement it is increased by a factor of 1/cos(theta) where theta=tan-1(del_col/del_row)

%
%Cluster dimension
%|y (row)
%|
%- - -> (col) x
% z pp to the surface of this page, going up

min_x=3; %min possible x point that can be drawn by scanning
min_y=3; %min possible y point that can be drawn by scanning
min_z=5; %min possible z point that can be drawn by scanning

%Conversion factor to reality
%Tilted angle of the whole page in x-y plage, theta
% .
%     .   z ^
% ....... x-y plane
theta=30; %degree

%Scaling image
scaling_factor=[1 1];% Scaling factor of [a b] means it will be resized to a/b

%Scanning method
method=1; %1 to scan row by row, the points that has to be scanned
          %2 scan boundary in an optimum way
Max_allowable_pt_seperation=5;
%Maximum allowable point seperation that can be considerred that same loop in method 2
% ### This should be tuned based on image ###

%preferrence factor for row and col(hor. and ver.) movement
PF_row=1.01; %take row/col as one and other value less than 2, 1.1 is good enough
PF_col=1;

%scan Starting position
% 0,0   0,1  0->lower row/col 1-> higher row or column
% 1,0   1,1  row,column
SP=[1 0];

% ### main coding starts ###

theta=theta*pi/180; %theta in radian

min_col=min_x; %min no. of col of the image that can be considered as one
min_row=round(min_y*min_z/sqrt((min_z*cos(theta))^2+(min_y*sin(theta))^2));
%min no. of col of the image that can be considered as one
if min_row<=0
    min_row=1;
end
% since x is in col position, tilt doesn't change the min col
%but theta being an angle between y and z axis, min_row is contributed by min_y and min_z
%when theta is 0 degree the min_row is min_y, when it is 90 degree, min_row is min_z
%so min_row is determined using an elliptical distribution

%Loading image
image_1=imread('U','bmp');

%flipping vertically so that from row and col perspective it looks similar to the original picture
image_1=flipud(image_1);

%Scaling image
if scaling_factor(1)/scaling_factor(2)~=1
    image_1=scale_image(image_1,scaling_factor);
end
%This point will also be considered as the origin for the xyz plane
%Making image of desired size pixels
if and(min_col~=1,min_row~=1)
    clusterred_image=Cluster_image(image_1,min_col,min_row);
else
```

```
    clusterred_image=image_1;
end

clear image_1

clf
%subplot(2,1,1)
hold on
%Plotting clusterred_image
[r,c]=find(clusterred_image); plot(c,r,' sy');
clear r c

if method==2 %Getting boundary for scanning scheme or 2
    %Getting 2D boundary of the image
    clusterred_image=get_2D_boundary(clusterred_image);
    %clear clusterred_image
    %Plotting boundary in green
    [r,c]=find(clusterred_image); plot(c,r,' sr');
    clear r c
end

%Setting scanning sequence
[scan_order_row,scan_order_col]=Scan_Order(clusterred_image,PF_row,PF_col,method,SP);
%clear boundary PF_row PF_col
%plotting in scan_order_row and scan_order_col green for method 2

if method==2
    plot(scan_order_col,scan_order_row,'-b');
end

%plot_ptbypt(scan_order_row,scan_order_col); %plotting point by point to check how scanning is performed

%Slicing into sections so that every section can be drawn without any break
if method==1 %if it is method 1 then it is solid image but for method 2 it is the boundary of the image
    is_boundary=0; %that is available. Procedure depends on this information.
elseif method==2
    is_boundary=1;
end

[row_significant,col_significant,SP_row,SP_col]=Slice(scan_order_row,scan_order_col,method,
Max_allowable_pt_seperation,is_boundary);
%SP point is special point that has only one point not start or end of a section in a row,
%used in method 1
%is_boundary indicates whether image is consists of boundary values or solid image
%1 for boundary and zero for solid images
plot(col_significant,row_significant,' *r')

%Interpolating middle points, mainly for method 1, where you have to insert multiple rows
% ### for method==2 it will do nothing ### because you don't need intermediate point
%while going from one to other
%it is already going at a writing velocity
if method==1
    [scan_order_row,scan_order_col]=Interpolate(row_significant,col_significant,method,interm_level);
    plot(scan_order_col,scan_order_row,' ob');
end

%Setting original scanning sequence, for method 1 row_significant is basically giving
scanning_sequence_command_file(scan_order_row,scan_order_col,row_significant,col_significant,SP_row,SP_col,
method,interm_level,d_p2p_mat,v_v2v_write,v_v2v_travel,theta,min_col,min_row);
```

A.9.2 Other functions

Clustering the image

```
function clusterred_image=Cluster_image(image,min_x,min_z)
%This is the function to bundle pixels in a bigger cluster
%mentioned by min_x and min_z

image_size=size(image);
clusterred_image_size=round([image_size(1)/min_z  image_size(2)/min_x]);
clusterred_image=zeros(clusterred_image_size);

%Finding a point and
%Checking whether all point within that cluster defined by min_x and min_z is non zero
Org_No_1=length(find(image==1));

disp('Clusterring the image.. please wait')

while ~isempty(find(image==1)) %Searching until everypoint is scanned
    found_one_cluster=0;

    %Finding non zero row and column
    [row,column]=find(image==1);
```

```
    Index=1;
    while found_one_cluster==0
        %Making temporary cluster to verify
        temp_cluster=[];
        for i=1:min_z
            temp_cluster=[temp_cluster;image(row(Index),column(Index):column(Index)+min_x-1)];
        end

        %Checking whether it is valid cluster
        if length(find(temp_cluster==1))==min_x*min_z
            clusterred_image(floor(row(Index)/min_z+1),floor(column(Index)/min_x)+1)=1;
            found_one_cluster=1;
            %Deleting selected part from the image
            for i=1:min_z
                image(row(Index),column(Index):column(Index)+min_x-1)=0;
            end
        else
            image(row(Index),column(Index))=0;
            Index=Index+1;
            if Index>length(row)
                found_one_cluster=1; %Just to make sure Index doesn't exceed limit
            end
        end
    end
end

disp('Clusterring done. Thanks')
```

Finding 2D boundary

```
function slide_boundary=get_2D_boundary(slide)
%Any non-zero point that has all the four-corner(top, bottom, left, and right)
%filled is not a boundary value. So, those points are removed to keep only the boundary value
%any point at the extreme boundary is also boundary
Size=size(slide);
slide_boundary=slide;

[I,J]=find(slide);
for i=1:length(I)
    row_now=I(i);
    col_now=J(i);

    %checking 4 side of the point
    if slide(row_now-1,col_now)==0 %Bottom
    elseif slide(row_now+1,col_now)==0 %Top
    elseif slide(row_now,col_now-1)==0 %left
    elseif slide(row_now,col_now+1)==0 %right
    else
        slide_boundary(row_now,col_now)=0;
    end
end
```

Determining the scanning order

```
function [scan_order_row,scan_order_col]=Scan_Order(clusterred_image,PF_row,PF_col,method,SP)
%This is the program to find scanning sequence
% from a given clustered frame or original frame

[total_row,total_col]=size(clusterred_image);

%Finding non zero row and column
[row,col]=find(clusterred_image==1);
L_row=length(row);

%Sorting based on starting point
[row,col]=sort_on_SP(row,col,SP);

if or(method<0,method>2)
    disp('Illegal method')
    return
end

if method==1
    scan_order_row=row;
    scan_order_col=col;
    disp('Scan order processing.. done')
    return %no work to do to detect the optimum scanning scheme
end

%Setting order
%takes the left lower most corner as a starting point
%Moves to closest point
```

```
%preference of movement can be set by preference factor

%Finding significant edge by slicing method, this will be used to modify the edges
[row_significant,col_significant]=Slice(row,col,1,10,1);
%the 10 will not be used for method 1, so no worry
%last value is is_boundary and it is 1 since it is already bondary values giving single point
% at the edge the program will not consider those as a single points

current_row=row(1); current_col=col(1);
scan_order_row=current_row; scan_order_col=current_col;
%Removing current element since it is already entered
row=remove(row,1); col=remove(col,1);
%This is a previous row too since it is entered, moreover it is first time entering
prev_row=current_row; prev_col=current_col;
%removing the element from row_significant and col_significant
I_sig=find(and(row_significant==current_row,col_significant==current_col));
row_significant=remove(row_significant,I_sig);
col_significant=remove(col_significant,I_sig);

disp('Ordering scan sequence.. please wait')

%Primarily selecting scanning path for method 2
for i=1:length(row)
    %Finding closest position
    distance=sqrt(((current_row-row)*PF_row).^2+((current_col-col)*PF_col).^2);
    %Col change cost is increased by a factor of sqrt(1.25)
    %so that it prefers horizontal change instead of vertical change
    [Min,I_point]=min(distance);

    %storing current position
    current_row=row(I_point(1));
    current_col=col(I_point(1));
    %Checking whether there is a row change
    if current_row-prev_row~=0 %when there is a row change taking nearest significant position
        D=sqrt(((row_significant-prev_row)*PF_row).^2+((col_significant-prev_col)*PF_col).^2);
        [Min,I_min]=min(D);
        current_row=row_significant(I_min(1));
        current_col=col_significant(I_min(1));
        %Finding element to remove from row
        I_point=find(and(row==current_row,col==current_col));
    end
    scan_order_row=[scan_order_row;current_row];
    scan_order_col=[scan_order_col;current_col];
    %Removing current element since it is already entered and definining
    %current pos previous for the next computation
    row=remove(row,I_point);   col=remove(col,I_point);
    prev_row=current_row;    prev_col=current_col;

    %removing the element from row_significant and col_significant if it is there
    I_row_sig=find(and(row_significant==current_row,col_significant==current_col));
        if ~isempty(I_row_sig)
            row_significant=remove(row_significant,I_row_sig);
            col_significant=remove(col_significant,I_row_sig);
        end

    %Plotting in order to make sure it is going in a right direction
%    plot(scan_order_col,scan_order_row,' *r')
end
disp('Scan order processing.. done')
```

Sectioning the whole scheme

```
function [row_significant,col_significant,SP_row,SP_col]=Slice(scan_order_row,
scan_order_col,method,Max_allwable_pt_seperation,is_boundary)
%This is the function to slice the scanning order so that it can scan row by row
%or it can go through maximum no. of points at a time in a boundary condition
%SP point is special point that has only one point not start or end of a section in a row
%used in method 1
%is_boundary indicates whether image is consists of boundary values or solid image
%1 for boundary and zero for solid images


%Converting into col matrix if not
S=size(scan_order_row);
if S(1)<S(2)
    scan_order_row=scan_order_row';
    scan_order_col=scan_order_col';
end

MX=Max_allwable_pt_seperation;

col_significant=[];
row_significant=[];
SP_row=[]; %Special points, that is just a point, not boundary of a section in a row
```

```
SP_col=[];

%For method 2, when it touches all the point that can be drawn at a stroke
if method==2
    %Finding distance between successive points
    [scan_path_distance,scan_path_L]=FindP2PDistance(scan_order_row,scan_order_col);
    I=find(scan_path_distance>MX);
    col_start_index=[1 I+1];
    col_end_index=[I length(scan_order_col)];
    row_start_index=[1 I+1];
    row_end_index=[I length(scan_order_row)];
    for i=1:length(col_start_index)
      col_significant=[col_significant scan_order_col(col_start_index(i)) scan_order
      _col(col_end_index(i))];
      row_significant=[row_significant scan_order_row(row_start_index(i)) scan_order
      _row(row_end_index(i))];
    end
    %converting into column matrix
    col_significant=col_significant';
    row_significant=row_significant';
    return
end

%Slicing in sections having same row
[scan_path_distance,scan_path_L]=FindP2PDistance(scan_order_row,zeros(size(scan_order_row)));
%Finding distance that is more than or equal to 1
row_slice_start_index=[1 find(scan_path_distance>=1)+1];

for i=1:length(row_slice_start_index)
    %Sliced according in each row
    if i~=length(row_slice_start_index)
      row_slice=scan_order_row(row_slice_start_index(i):row_slice_start_index(i+1)-1);
      col_4_row_slice=scan_order_col(row_slice_start_index(i):row_slice_start_index(i+1)-1);
    else
      row_slice=scan_order_row(row_slice_start_index(i):length(scan_order_row));
      col_4_row_slice=scan_order_col(row_slice_start_index(i):length(scan_order_col));
    end

    [scan_path_distance,scan_path_L]=FindP2PDistance(row_slice,col_4_row_slice);
    %Finding distance that is more than one
    col_start_index=[1 find(scan_path_distance>1)+1];
    col_end_index=[find(scan_path_distance>1) length(col_4_row_slice)];
    if ~is_boundary
        %Finding special points that has only one point not part of the section
        I_SP=find(col_end_index-col_start_index==0);
        if ~isempty(I_SP)
            SP_row=[SP_row;row_slice(1)*ones(size(I_SP'))];
            SP_col=[SP_col;col_4_row_slice(col_start_index(I_SP'))];
            %removing special point from normal points
            for j=1:length(I_SP)
                col_start_index=remove(col_start_index,I_SP(j)-j+1);
                %-j+1 is to compensate the change of dimension size once it is removed
                col_end_index=remove(col_end_index,I_SP(j)-j+1);
            end
        end
    end
    col_significant_this_row=col_4_row_slice(sort([col_start_index col_end_index]));

    %Storing significant row and column information
    col_significant=[col_significant;col_significant_this_row];
    row_significant=[row_significant; row_slice(1)*ones(size(col_significant_this_row))];
end

%Avoiding mulitiple entry of a single point, this sort of porblem may arise when
%you are trying to find significant row and col for a diagrag showing boundary
[row_significant,col_significant]=avoid_repeat(row_significant,col_significant);

%converting into column matrix
col_significant=col_significant';
row_significant=row_significant';
```

Adding intermediate point for raster scan

```
function [row_significant_new,col_significant_new]=interpolate(row_significant
,col_significant,method,interm_level)
%This is the function to add intermediate point based on no. of intermediate level
%Basically outputs are modified and column significant

row_significant_new=[];
col_significant_new=[];

if method==1
    row_all=avoid_repeat(row_significant);
    % just extracting the row that is present
```

```
L=length(row_all);
disp('Putting intermediate levels..')
for i=1:L-1
    %Taking two rows to find intermediate rows
    row_1=row_all(i); row_2=row_all(i+1);
    row_int=(row_2-row_1)./(interm_level+1)*[1:interm_level]+row_1;

    col_1=[];   col_2=[];
    %Taking two columns to find intermediate columns
    col_1=col_significant(find(row_significant==row_all(i)));
    col_2=col_significant(find(row_significant==row_all(i+1)));
    %Getting smaller element having column to scan for closest column
    if length(col_1)<=length(col_2)
        col_s=col_1; col_b=col_2; direction_changed=0;
    else
        col_b=col_1; col_s=col_2; direction_changed=1;
    end
    %finding points closer to
    col_index=1;
    col_int=[];
    for j=1:length(col_s)
        d=sqrt((col_s(j)-col_b).^2+1);%distance
        [Min,I_cp]=min(d); %Getting index of closest point
        cp=col_b(I_cp);

        %Finding intermediate points
        col_int(col_index,1:interm_level)=(cp-col_s(j))/(interm_level+1)
        *[1:interm_level]+col_s(j);

        %removing cp
        col_b=remove(col_b,I_cp);
        col_index=col_index+1;
    end
    %extra points, that is a new section, will be neglected

    S=size(col_int);%size of col_int
    r=S(1);
    c=S(2);

    %if direction is changed then flipping the col_int values
    if direction_changed==1
        a=[];
        for k=1:floor(c/2)
            a=col_int(:,k);
            col_int(:,k)=col_int(:,c-k+1);
            col_int(:,c-k+1)=a;
        end
    end

    %Adding intermediate levels
    new_row_2_add=[];
    for j=1:interm_level
        new_row_2_add=[new_row_2_add;row_int(j)*ones(r,1)];
    end
    if i~=L-1 %for last row we have to add col_2 too
        row_significant_new=[row_significant_new;row_1*ones(size(col_1));
        new_row_2_add];
    else
        row_significant_new=[row_significant_new;row_1*ones(size(col_1));new_row_2_add;
        row_2*ones(size(col_2))];
    end

    new_col_2_add=[];
    for j=1:interm_level
        new_col_2_add=[new_col_2_add;col_int(:,j)];
    end
    if i~=L-1
        col_significant_new=[col_significant_new;col_1;new_col_2_add];
    else
        col_significant_new=[col_significant_new;col_1;new_col_2_add;col_2];
    end
 end
%organizing columns alternatively when scanning through row
% - - - - > \/
% < - - - -

clear row_significant col_significant
row_all=avoid_repeat(row_significant_new); % just extracting the row that is present
L=length(row_all);
alter_sort_order=0; %it will alter sort order for column if this value equals to 1
for i=1:L
    if alter_sort_order
        I=find(row_significant_new==row_all(i));
        col_this_row=col_significant_new(I);
        %sorting in opposite order
```

```
            col_this_row=col_this_row(length(col_this_row):-1:1);
            col_significant_new(I)=col_this_row;
            alter_sort_order=0;
        else
            alter_sort_order=1;
        end
    end
end
disp('Putting intermediate levels.. done')
```

A.9.3 Writing in a file to be used for Labview

```
function scanning_sequence_command_file(scan_order_row,scan_order_col,row_significant,
col_significant,SP_row,SP_col,method,interm_level,d_p2p_mat,v_v2v_write,v_v2v_travel,theta,
min_col,min_row);
%this is the function that will write scanning sequence to a file
%that will be extracted by a labview code and used to scan the sample

%Making lowest col and row position as origin
min_row_value=min(scan_order_row);
scan_order_row=scan_order_row-min_row_value;
row_significant=row_significant-min_row_value;
min_col_value=min(scan_order_col);
scan_order_col=scan_order_col-min_col_value;
col_significant=col_significant-min_col_value;

%Converting row, col and theta information in x, y and z value
%|y
%|
%- - -> x
% z pp to the surface of this page, going up

%scanning position for x, y and z in terms of clusterred image units, 1
x=scan_order_col;
y=scan_order_row*cos(theta);
z=y*tan(theta);

%a 3D plotting in relative position, clusterred matrix
subplot(2,1,2)
plot(x,y)
title('Press any button to continue.. it is in pause mode')
plot_3D(x,y,z,1,cos(theta)) %1 and cos(theta) are the step-unit in x and y plane

%Scanning position in original units
x=scan_order_col*min_col*d_p2p_mat; %d_p2p_mat be the distance between point to point in real
y=scan_order_row*min_row*d_p2p_mat*cos(theta);
z=y*tan(theta);

shutter_status=[];

if method==1
    L=length(scan_order_row);
    %finding scanning scheme for clusterred image where to write and where to travel faster than

    %it start from first point goes to second at a writing speed
    %and second point to third point at faster speed
    row_start=scan_order_row(1:L-1);
    row_end=scan_order_row(2:L);
    %Velocities in a dimension
    vel=zeros(size(row_start));
    vel([1:2:2*floor((L-1)/2)+1])=v_v2v_write;
    % L-1 is due to the fact that no of row is 1 element smaller than the starting or ending row no.
    vel([2:2:2*floor((L-1)/2)])=v_v2v_travel;

    %when it will go from one position at the end of a row
    %to the next position of the next row it will go at writing velocity too detecting row change
    D=row_end-row_start; new_row_index=find(D~=0);
    vel(new_row_index)=v_v2v_write;

    shutter_status=ones(size(vel));
    shutter_status(find(vel>1))=0;
    clear row_start row_end

elseif method==2
    %Connecting all values within row significant, col significant odd to even
    %[that means one of that can be connected at once]
    %and then finishing the circle by again adding row col sig odd example
    %size of row sig.  = 4, there is 2 loops one from row sig(1),col sig(1) to row sig(2), col sig(2)
    %second one is from row sig(3),col sig(3) to row sig(4), col sig(4)
    x_new=[]; y_new=[]; z_new=[];
    vel=[];
    for i=1:length(row_significant)/2
        %Starting index in scan_order_row and scan_order_col
```

```
        I_start=find(and(scan_order_row==row_significant(i),scan_order_col==col_significant(i)));
        I_end=find(and(scan_order_row==row_significant(i+1),scan_order_col==col_significant(i+1)));
        %making new x with to make sure it completes the loops
        x_new=[x_new;x(I_start:I_end);x(I_start)];
        y_new=[y_new;y(I_start:I_end);y(I_start)];
        z_new=[z_new;z(I_start:I_end);z(I_start)];
        %Calculating velocities
        %Except the very first starting of a loop, the sample velocity should be travelling velocity
        %when going to its starting point
        if i==1
            vel=[vel;v_v2v_write*ones(I_end-I_start+1,1)];
            shutter_status=[shutter_status;ones(I_end-I_start+1,1)];
        else
            vel=[vel;v_v2v_travel;v_v2v_write*ones(I_end-I_start+1,1)];
            shutter_status=[shutter_status;0;ones(I_end-I_start+1,1)];
        end
    end

    x=x_new; y=y_new; z=z_new;
    L=length(x);
    clear x_new y_new z_new
end

%Finding real scanning scheme
%Positions to start and end
x_start=x(1:L-1); x_end=x(2:L);
y_start=y(1:L-1); y_end=y(2:L);
z_start=z(1:L-1); z_end=z(2:L);

%velocity components in x, y and z direction, it is dependent on the distance it is
travelling at x, y and z since
%all has to finish at the same time
del_x=x_end-x_start; del_y=y_end-y_start; del_z=z_end-z_start;
del_r=sqrt(del_x.^2+del_y.^2+del_z.^2);
vel_x=abs(vel.*del_x./del_r); vel_y=abs(vel.*del_y./del_r); vel_z=abs(vel.*del_z./del_r);

%Only change in position will be recorded, so clearing unnecessary elements
clear x_start x_end y_start y_end z_start z_end del_r

%Converting all the parameters into count
info_count=round([1/.007*[del_x del_y del_z vel_x vel_y vel_z] shutter_status]);

%openning file
fid=fopen('Scanning_scheme.txt','w');
%storing change in distance, velocities
for i=1:length(del_x)
    fprintf(fid,'%g\t%g\t%g\t%g\t%g\t%g\t%g\n',info_count(i,:));
end
fclose(fid);

disp('Scanning scheme is successfully saved in ''Scanning_scheme.txt'' located in the current folder')
```

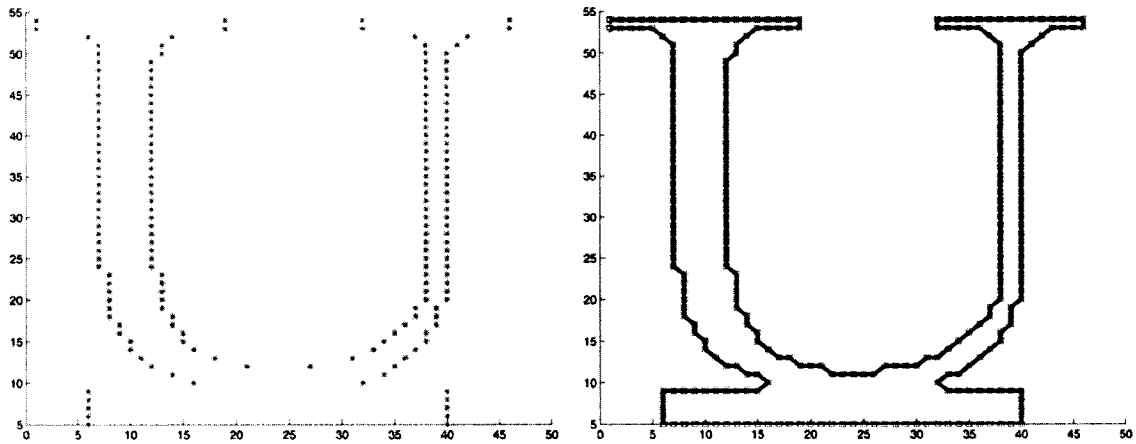

Figure A.9.1: Scanning scheme optimization using (a) raster scan and (b) vector scan. For the raster scan case scanning will be performed row wise starting at the left most writing point at the end of that segment. Another segment of the same row (if any) will be started after skipping the region in between the two segments. In contrast the entire boundary will be scanned for the vector scan case which saves resources since the scanning time should be shorter.

Bibliography

[1] S. Maruo, O. Nakamura, and S. Kawata, "Three-dimensional microfabrication with two-photon-absorbed photopolymerization," *Optics letters* **22**, pp. 132–134, 1997.

[2] E. F. Reznikova, J. Mohr, and H. Hein, "Deep photo-lighography characterization of su-8 resist layers," *Microsystem Technologies* **11**, pp. 282–291, 2005.

[3] "www.microresist.de/poster_ormocer.pdf,"

[4] R. Houbertz, L. Fröhlich, M. Popall, U. Streppel, P. Dannberg, A. Bräuer, J. Serbin, and B. N. Chichkov, "Inorganic-organic hybrid polymers for information technology: from planar technology to 3d nanostructures," *Advanced Engineering Materials* **5**, pp. 551–555, 2003.

[5] R. Yang and W. Want, "Numerical and experimental study of an out-of-plane prealigned refractive microlens fabricated using ultraviolet lithography method," *Optical Engineering* **43**, pp. 3096–3103, 2004.

[6] Z.-g. Ling, K. Lian, and L. Jian, "Improved patterning quality of su-8 microstructures by optimizing the exposure parameters," *Proceedings of SPIE* **3999**, pp. 1019 1027, 2000.

[7] D. A. Parthenopoulos and P. M. Rentzepis, "Three-dimensional optical storage memory," *Physical Review Letters.* **245**, pp. 843–845.

[8] R. Menzel, "Photonics: Linear and nonlinear interactions of laser light and matter," *Berlin, Germany: Springer-Verlag* , 2001.

[9] J. M. Song, T. Inoue, H. Kawazumi, and T. Ogawa, "Determination of two photon absorption cross section of fluorescein using a mode locked titanium sapphire laser," *Analytical Sciences* **15**, pp. 601–603, 1999.

[10] S. Y. Lin, E. Chow, J. Bur, S. G. Johnson, and J. D. Joannopoulos, "Low-loss, wide-angle y splitter at 1.6-μm wavelengths built with a two-dimensioanl photonic crystal," *Optics Letters* **27**, pp. 1400–1402, 2002.

[11] H.-G. Pakr, S.-K. Kim, S.-H. Kwon, G.-H. Kim, S.-H. Kim, R. H-Y, S.-B. Kim, and Y.-H. Lee, "Single-mode operation of two-dimensional photonic crystal laser with central post," *IEEE Photonics Technology Letters* **15**, pp. 1327–1329, 2003.

[12] J. L. Jewell, J. P. Harbison, A. Scherer, Y. H. Lee, and L. T. Florez, "Vertical-cavity surface-emitting lasers: Design, growth, fabrication, characterization," *IEEE Journal of Quantum Electronics* **27**, pp. 1332–1346, 1991.

[13] M. Watanabe, S. Juodkazis, H. B. Sun, S. Matsuo, H. Misawa, M. Miwa, and R. Kaneko, "Transmission and photoluminescence images of threedimensional memory in vitreous silica," *Applied Physics Letters* **74**, pp. 3957–3959.

[14] E. N. Glezer, M. Milosavljevic, L. Huang, R. J. Finlay, T.-H. Her, J. P. Callan, and E. Mazur, "Three-dimensional optical storage inside transparent materials," *Optics Letters* **21**, pp. 2023–2025, 1996.

[15] K. Miura, J. Qiu, H. Inouye, T. Mitsuyu, and K. Hirao, "Photowritten optical waveguides in various glasses with ultrashort pulse laser," *Applied Physics Letters* **71**, pp. 3329–3331, 1997.

[16] Y. Sikorski, A. A. Said, P. Bado, R. Maynard, C. Florea, and K. A. Winick, "Optical waveguide amplifier in nd-doped glass written with near-ir femtosecond laser pulses," *Electronic Letters* **36**, pp. 226–227, 2000.

[17] H. B. Sun, Y. Xu, S. Juodkazis, K. Sun, M. Watanabe, J. Nishii, S. Matsuo, and H. Misawa, "Arbitrary-lattice photonic crystals created by multiphoton microfabrication," *Optics Letters* **26**, pp. 325–327, 2001.

[18] S. Katayama, M. Horiike, K. Hirao, and N. Tsutsumi, "Structures induced in by irradiation of femto-second laser pulse in dyed polymeric materials," *Journal of Polymer Science* **40**, pp. 2800–2806, 2002.

[19] S. Katayama, M. Horiike, M. Urairi, K. Hirao, and N. Tsutsumi, "Structures induced in polysilane and thin polysilane layer coated polymer films by irradiation of femto-second laser pulse," *Chemical Physics Letter* **373**, pp. 140–145, 2003.

[20] S. Kawata and H.-B. Sun, "Two-photon photopolymerization as a tool for making micro-devices," *Applied Surface Sciences* **208-209**, pp. 153–158, 2003.

[21] S. M. Kuebler, K. L. Braun, W. Zhou, J. K. Cammack, T. Yu, C. K. Ober, S. R. Marder, and J. W. Perry, "Design and application of high-sensitivity two-photon initiators for three-dimensional microfabrication," *Journal of Photochemistry and Photobiology A: Chemistry* **158**, pp. 163–170, 2003.

[22] H. Kou, A. Asif, W. Shi, Z. Jiang, and W. Huang, "A novel hyperbranched polyester acrylate used for microfabrications," *Polymers for Advanced Technologies* **15**, pp. 1000–1002, 2004.

[23] J. Serbin, A. Egbert, A. Ostendorf, B. N. Chichkov, H. Houberta, G. Domann, J. Schulz, C. Cronauer, L. Fröhlich, and M. Popall, "Femtosecond laser-induced two-photon polymerization of inorganic-organic hybrid materials for applications in photonics," *Optics Letters* **28**, pp. 301–303, 2003.

[24] G. Witzgall, R. Vrijen, E. Yablonovitch, V. Doan, and B. J. Schwartz, "Single-shot two-photon exposure of commercial photoresist for the production of three dimensional structures," *Optics Letters* **22**, pp. 1745–1747, 1998.

[25] C. H. Lee, T. W. Chang, K. L. Lee, J. Y. Lin, and J. Wang, "Fabricating high-aspect ratio sub-diffraction-limit structures on silicon with two-photon photopolymerization adn reactive ion etching," *Applied Physics A* **79**, pp. 2027–2031, 2004.

[26] W. H. Teh, U. Dürig, U. Drechsler, C. G. Smith, and H. J. Güntherodt, "Effect of low numerical-aperture femtosecond two-photon absorption on (su-8) resist for ultrahigh-aspect-ratio microstereolithography," *Journal of Applied Physics* **97**, 2005.

[27] K. K. Seet, V. Mizeikis, S. Matsuo, S. Juodkazis, and H. Miwawa, "Three-dimensional spiral-architecture photonic crystals obtained by direct laser writing," *Advanced Materials* **17**, pp. 541–545, 2005.

[28] W. Becker, E W amd Ehrfeld, P. Hagmann, A. Maner, and D. Münchmeyer, "Fabrication of microstructures with high aspect ratios and great structural heights by synchrotron radiation lithography, galvanoforming, and plastic moulding (liga process)," *Microelectronic Engineering* **4**, pp. 35–56, 1986.

[29] W. Ehrfeld and H. Lehr, "Deep x-ray lithography for the production of three-dimensional microstructures from metals, polymers and ceramics," *Radiation Physical Chemistry* **45**, pp. 349–365, 1986.

[30] C. Burbaum, J. Mohr, and P. Bley, "Fabrication of capacitive acceleration sensors by the liga technique," *Sensors and Acruorors A* **25-27**, pp. 559–563, 1991.

[31] S. K. Griffiths, "Fundamental limitations of liga x-ray lithography: sidewall offset, slope and minimum feature size," *Journal of Micromechanics and Microengineering* **14**, pp. 1332–1346, 2004.

[32] A. L. Bogdanov and S. S. Peredkov, "Use of su-8 photoresist for very high aspect ratio x-ray lithography," *Microelectronic Engineering* **53**, pp. 493–496, 2000.

[33] C.-R. Yang, G.-W. Hsieh, Y.-S. Hseih, and Y.-D. Lee, "Microstructuring characteristics of a chemically amplified photoresist systhesized for ultra-thick uv-liga applications," *Journal of Micromechanics and Microengineering* **14**, pp. 1126–1134, 2004.

[34] K. Ikuta and K. Hirowatari, "Real three dimensional micro fabrication using stereo lithograpy and metal molding," *Micro Electronic Mechanical Systems* **47**, pp. 42–47, 1993.

[35] J. L. Sanchez, J. A. van Kan, T. Osipowicz, S. V. Springham, and F. Watt, "A high resolution beam scanning system for deep ion beam lithography," *Nuclear Instruments and Methods in Physics Research B* **136**.

[36] J. A. van Kan, J. L. Sanchez, B. Xu, T. Osipowicz, and F. Watt, "Micromachning using focused high energy ion beams: deep ion beam lighography," *Nuclear Instruments and Methods in Physics Research B* **148**, pp. 1085–1089, 1999.

[37] D. P. Stumbo and J. C. Wolfe, "Ion exposure characterization of a chemically amplified epoxy resist," *Journal of Vacuum Science and Technology B* **11**, pp. 2432–2435, 1993.

[38] F. Munnik, F. Benninger, S. Mikhailov, A. Bertsch, P. Renaud, H. Lorenz, and Gmür, "High aspect ratio, 3d structuring of photoresist materials by ion beam liga," *Microelectronic Engineering* **67-68**, pp. 96–103, 2003.

[39] R. Yang and W. Wanjun, "Numerical and experimental study on gap compenstation and wavelength selection in uv-lighography of ultra-high aspect ratio su-8 microstructures," *Sensors and Actuators B* **110**, pp. 279–288, 2005.

[40] X. Tian, G. Liu, Y. Tian, P. Zhang, and X. Zhang, "Simulation of deep uv lithography with su-8 resist by using 365 nm light source," *Microsystem Technologies* **11**, pp. 265–270, 2005.

[41] W. Kaiser and C. Garrett, "2-photon excitation in caf2 - eu2+," *Physical Review Letters* **7**, p. 229, 1961.

[42] A. Dragomir, J. G. McInerney, D. N. Nikogosyana, and P. G. Kazansky, "Two-photon absorption properties of commercial fused silica and germanosilicate glass at 264 nm," *Applied Physics Letters* **80**, pp. 114–116, 2002.

[43] J. N. Chróinín, A. Dragomir, J. G. McInerney, and D. N. Nikogosyan, "Accurate determination of two-photon absorption coefficients in fused silica and crystalline quartz at 264 nm," *Optical Communications* **187**, pp. 185–191, 2001.

[44] Y. A. Repeyev, E. V. Khoroshilova, and N. D. N, "212.8 nm laser photolysis of aromatic and aliphatic amino-acids and related peptides," *Journal of Photochemistry and Photobiology B-Biology* **12**, pp. 259–274, 1992.

[45] P. Liu, W. K. Smith, H. Lotem, J. H. Bechtel, N. Bloembergen, and R. S. Adhav, "Absolute 2-photon absorption-coefficients at 355 and 266 nm," *Physical Review B* **17**, pp. 4620–4632, 1978.

[46] K. Yamasaki, S. Juodkazis, M. Watanabe, H. B. Sun, S. Matsuo, and H. Misawaa, "Recording by microexplosion and two-photon reading of three-dimensional optical memory in polymethylmethacrylate films," *Applied Physics Letters* **76**, pp. 1000 1002, 2000.

[47] B. E. A. Saleh and M. C. Teich, "Fundamentals of photonics," *1st ed. , Germany: John Wiley and sons* , 1991.

[48] V. G. Dmitriev, G. G. Gurzadyan, and N. D. N, "Handbook of nonlinear optical crystals," *Springer* , 1991.

[49] T. Tomie, I. Okuda, and M. Yano, "3-photon absorption in caf2 at 248.5 nm," *Applied Physics Letters* **55**, pp. 325–327, 1989.

[50] R. DeSalvo, A. A. Said, D. J. Hagan, E. W. Vanstryland, and M. Sheikbahae, "Infrared to ultraviolet measurements of two-photon absorption and n(2) in wide bandgap solids," *IEEE Journal of Quantum Electronics* **32**, pp. 1324–1333, 1996.

[51] T. Mizunami and K. Takagi, "2-photon absorption in silica optical fibers measured with a xebr excimer laser," *Optics Communications* **68**, pp. 223–227, 1988.

[52] I. N. Ross, W. T. Toner, and C. J. Hooker, "Nonlinear properties of silica and air for picosecond ultraviolet pulses," *Journal of Modern Optics* **37**, pp. 555–573, 1990.

[53] Y. P. Kim and M. H. R. Hutchinson, "Intensity-induced nonlinear effects in uv window materials," *Applied Physics B-Photophysics and Laser Chemistry* **49**, pp. 469–478, 1989.

[54] T. Mizunami, T. Miyazaki, and K. Takagi, "Short-pulse ultraviolet fiber raman laser pumped by a xecl excimer laser," *Journal of the Optical Society of America B-Optical Physics* **4**, pp. 498–504, 1987.

[55] W. L. Smith, "two photon absorption in condensed media," *CRC Handbook of Laser Science and Technology - Optical Materials: Part 1* , pp. 229–258, 1986.